Composites Science and Technology 270 (2025) 111281

Contents lists available at ScienceDirect

Composites Science and Technology

journal homepage: www.elsevier.com/locate/compscitech

Integrated experimental and computational approach to analyse and design multiphase nanocomposites for broadband reflection loss

A. Phanendra Kumar [a], Rishi Raj [b], Dineshkumar Harursampath [a], Sathiskumar Anusuya Ponnusami [c,*]

[a] NMCAD Laboratory, Department of Aerospace Engineering, Indian Institute of Science, Bengaluru, Karnataka, India
[b] Polymer Processing Laboratory, Department of Material Engineering, Indian Institute of Science, Bengaluru, Karnataka, India
[c] Department of Engineering, City St George's, University of London, London, United Kingdom

ARTICLE INFO

Keywords:
Electromagnetic reflection loss
Multiphase nanocomposites
Electromagnetic properties characterisation
Transfer matrix method
Impedance matching

ABSTRACT

This study presents an integrated experimental and computational methodology for analysing multiphase composites with ceramic ($BaTiO_3$, $CoFe_2O_4$) inclusions and carbon-based inclusions (MWCNTs) aimed at broadband electromagnetic (EM) reflection loss (RL) applications. Characterisation techniques (SEM, TGA, and X-ray 3-D tomography) were employed to analyse the nanocomposite. Fabricated nanocomposites were tested using a two-port VNA, and the EM properties of the composites were derived using the Nicolson-Ross-Weir (NRW) algorithm. An in-house optimisation tool is used to extract the EM properties of individual nanoparticles and later validate them using the experimental results. The RL spectrum in the frequency range is attained using the in-house Transfer Matrix Method (TMM)-based tool, which is validated using the scattering parameters obtained from the two-port VNA. Later, parametric studies are carried out using the validated in-house tools by varying the influencing parameters. Results have shown that composites with high $BaTiO_3$ or MWCNT contents exhibited impedance mismatches, leading to immediate EM reflection upon interaction with the nanocomposite surface. In contrast, $CoFe_2O_4$-dominant composites achieved broadband RL (< -10 dB) over a bandwidth of 4.4 GHz across different thicknesses even at higher loading due to improved impedance matching. Incident transverse magnetic (TM) polarised EM waves provided broadband RL up to 80° incidence. In contrast, transverse electric (TE) polarised EM waves showed broadband RL at angles up to 40° due to different field interactions. The proposed generalised approach offers a versatile framework for designing nanocomposites tailored for specific broadband or frequency-selective RL applications.

1. Introduction

In recent years, research on designing materials or structures for broadband reflection loss has gained interest for both long-standing aeronautical and emerging space security applications [1–5]. With the advancement in the detection using radars, which can cover a wide range of frequencies and multiple angles of incidence, the research on fabricating novel composites reaching demanding requirements is evolving day by day [6,7]. Traditional two-phase composites can limit the frequency bandwidth, which makes them efficient only in a small frequency range [8]. Whereas multiphase composites are observed to have mitigated this issue because each individual phase will provide an added mechanism that helps attain a broadband width reflection loss [8–10]. Meng et al. [9] have fabricated a multiphase composite with carbon black and barium titanate ($BaTiO_3$) nanoparticles embedded in the matrix made up of polyvinylidene fluoride (PVDF). The composites are fabricated via a simple blending and hot-moulding technique, demonstrating superior absorption properties compared to two-phase systems (CB/PVDF or BT/PVDF). At optimal filling ratios, the multiphase nanocomposite achieved a broadband RL covering 3.5 to 18 GHz with samples of thickness 1.5 mm to 5.0 mm. The broadband reflection loss in this three-phase composite can be attributed to the synergic effect between the fillers and the matrix, as well as different mechanisms like dipole polarisation, dielectric losses, and the conductive nature of carbon black. Vovchenko et al. [8] explored the absorption characteristics of epoxy-based composites reinforced with multiphase fillers, including carbon nanotubes (CNTs) combined with titanium dioxide (TiO_2) or carbonyl iron (Fe), across a wide frequency range (1–67 GHz). The research demonstrates that ternary composites, particularly CNT/Fe/epoxy, exhibit superior electromagnetic reflection loss (RL) ranging between −30 dB and −44 dB due to the synergistic

* Corresponding author.
E-mail address: sathiskumar.ponnusami@citystgeorges.ac.uk (S.A. Ponnusami).

https://doi.org/10.1016/j.compscitech.2025.111281
Received 29 April 2025; Received in revised form 19 June 2025; Accepted 27 June 2025
Available online 5 July 2025

conductive nature of CNTs and magnetic losses due to Fe. For enhanced performance, 4-layered composites were designed by stacking single layers with varying compositions/thicknesses (e.g., low-CNT layers for impedance matching and high-CNT layers for absorption). By optimising filler ratios and employing multilayered designs, the study achieved enhanced broadband absorption (covering 8 to 12 GHz) and tunable RL performance. Wang et al. [10] has developed a novel composite by embedding magnetic particles $Ni_3Fe/NiFe_2O_4$ into a porous carbon-based matrix. The Ni_3Fe alloy enhances magnetic loss due to its high saturation magnetisation, while $NiFe_2O_4$ mitigates demagnetisation effects and reduces eddy current losses. The porous carbon network not only lowers the material's density but also promotes multiple reflections and scattering of electromagnetic waves (EMWs), improving absorption efficiency. The synergy between magnetic coupling, interfacial polarisation, and conductive loss mechanisms enables superior impedance matching and attenuation of EMWs across a wide frequency range. The developed composite attained the desired broadband RL with a 2 mm sample thickness covering X and Ku frequency bands.

A few works have been discussed before to emphasise the advantages of the multiphase composites for the intended broadband width reflection losses. Traditionally, designing these multiphase composites involves extensive experimental trial and error procedures by varying the loading content of different nanoparticles or the materials embedded inside the matrix [8–11]. Effective usage of multiphase composites' performance capabilities for broadband reflection loss requires optimising the volume fractions and electromagnetic properties of constituent phases. The extensive experimental trial-and-error to optimise nanoparticle volume fractions, a process that is both costly and time-intensive. Most notably, no prior research has utilised minimal experimental data to computationally optimise multiphase nanocomposites for broadband RL, leaving a significant gap to develop efficient computational design methodologies. The proposed methodology in this work bridges this gaps by introducing an integrated experimental-computational approach that minimises experimental effort. Using scattering parameters from just two nanocomposite samples per nanoparticle, obtained using a two-port Vector Network Analyser (VNA) and postprocessed with the Nicolson-Ross-Weir (NRW) algorithm, aids in attaining the EM properties of the composites. Later, using the in-house optimisation tool, based on Nelder–Mead and L-BFGS algorithms, the nanoparticles' EM properties and interaction parameters in the Lichtenecker mixing rule have been extracted. This enables precise tuning of compositions to achieve a 4.4 GHz broadband RL (<−10 dB) in the X-band, validated with 3%–6% deviation from experiments, significantly reducing the reliance on iterative fabrication.

Recent advancements in computational and analytical techniques have transformed the design and optimisation of multiphase composites for microwave absorption by enabling detailed insights into electromagnetic loss mechanisms. For instance, He et al. [12] employed high-resolution transmission electron microscopy (HRTEM) and fast Fourier transform (FFT) analysis, computationally processing lattice hybridisation and defects in hollow carbon nanocages embedded with $CoFe_2Se_4$ quantum dots, revealing how lattice strain and Moiré fringes enhance interfacial polarisation and dielectric loss, achieving a reflection loss of −67.6 dB and an effective absorption bandwidth of 11.4 GHz. The simulations reported further demonstrated reduced scattering intensities, highlighting the role of computational modelling in optimising far-field absorption characteristics. Similarly, Liu et al. [13] used Lorentz off-axis electron holography to quantitatively analyse gradient magnetic domains in Fe-Co@TiO_2 microrods, elucidating how macroscopic magnetic coupling, long-range magnetic diffraction, and nanoscale magnetic bridge connections amplify magnetic loss, resulting in a reflection loss of −51.5 dB and an absorption bandwidth of 8.6 GHz. Furthermore, Zhao et al. [14] applied density functional theory (DFT) calculations to study MoS_2/V_2O_3 heterostructures, showing that sulfur vacancies and interfacial charge separation significantly enhance dielectric loss through polarisation relaxation, with the system achieving a reflection loss of −69.65 dB and a bandwidth of 7.68 GHz. These studies underscore the power of integrating advanced characterisation methods, electromagnetic simulations, and quantum mechanical computations to unravel the complex interplay of dielectric, magnetic, and conductive losses in multiphase systems. These studies primarily focus on system-specific structural engineering and high-fidelity analysis.

The present work complements the previously mentioned computational works and addresses the key gap in the literature by introducing a generalisable computational framework that works on a physics-based tool (TMM tool), leverages minimal experimental testing to optimise the volume fraction of nanoparticles in the multiphase composite design for broadband absorption. The existing computational models [12–14] are often tailored to specific material systems, limiting their applicability across diverse composite configurations. Furthermore, achieving broadband RL across a wide range of incident angles and polarisations remains underexplored, despite its critical role in aerospace applications, where EM waves impinge from multiple directions. Our methodology addresses these deficiencies by developing a physics-based, material-agnostic framework using the modified Transfer Matrix Method (TMM) to predict RL spectra for any multiphase composite. This physics-based method takes into account both forward & backwards moving waves, multiple internal reflections and the phase of the reflected waves, before evaluating the finally transmitted and reflected EM wave components [2]. By integrating minimal experimental data with validated in-house tools, the proposed framework facilitates rapid exploration of the design space, optimising nanoparticle loadings for attaining broadband or frequency-specific RL. Parametric studies demonstrate that our proposed novel composite, combining $BaTiO_3$, $CoFe_2O_4$, and multi-walled carbon nanotubes (MWCNTs) in an epoxy matrix, achieves broadband RL (<−10 dB) under both Transverse Electric (TE) and Transverse Magnetic (TM) polarised EM waves, addressing angular sensitivity challenges. This generalised computational approach accelerates development cycles and ensures robust performance across varied operational conditions, offering a scalable solution for advanced EM absorption applications.

$BaTiO_3$ nanoparticles are used in the composite due to their enhanced dielectric properties [15]. The $BaTiO_3$ nanoparticles exhibit good ferroelectric properties, making them an ideal candidate for enhancing the dielectric properties of the overall composite due to their electric polarisation abilities [16]. When $BaTiO_3$ nanoparticles are incorporated into the epoxy, they will aid in increasing the dielectric properties of the composite, thereby enhancing its potential to store and dissipate the electrical energy [17]. This mechanism will be essential for broadband reflection loss applications, where the material must efficiently absorb and reduce the reflection of electromagnetic waves over a wide frequency range. Because of the ceramic behaviour of these nanoparticles, the electromagnetic properties do not vary over a wide range of temperatures [18]. Furthermore, $BaTiO_3$ ferroelectric nature allows for tunable dielectric properties through external electric fields, providing an additional control layer in the composite's performance [19]. Complementing the dielectric properties of $BaTiO_3$, $CoFe_2O_4$ nanoparticles are incorporated into the composite for its remarkable magnetic properties [20]. $CoFe_2O_4$ is ferromagnetic material; thus, the material has an overall magnetic moment that can respond without an applied magnetic field [21], which eventually helps in increasing the electromagnetic wave absorption. These ferrite-based nanoparticles assist in tailoring the overall permeability of the composite and, thus, the total absorption characteristics. With the aid of these ferromagnetic particles, magnetic energy can be dissipated because of the hysteresis losses [22], which assists in converting the magnetic component of incident EM energy to heat, thereby attenuating the incident EM waves. The synergic combination of $CoFe_2O_4$'s magnetic properties with $BaTiO_3$'s dielectric properties creates a unique composite that can simultaneously manage the electric and magnetic components

of electromagnetic waves, resulting in improved dissipation of the electromagnetic energy [23].

Due to high electrical conductivity, MWCNTs can effectively interact with the incident electromagnetic wave and impart conduction losses [24]. Not only do they cause conduction losses, but they also enhance the loss due to the dielectric losses. The higher electrical conductivity is attributed to the unique cylindrical structure and the sp^2 hybridised carbon atoms [25]. Due to the length-to-diameter ratio of the nanotubes, these nanoparticles can create large conductive paths, resulting in multiple reflections within the composite, helping increase the attenuation of EM waves [26]. Moreover, MWCNTs contribute to the mechanical integrity of the composite, providing tensile strength and reinforcement to the composite matrix and improving its structural stability and durability [27]. This makes MWCNTs valuable in composites intended to withstand challenging operating conditions, ensuring both mechanical integrity and enhanced EM wave attenuation under various operating conditions [28]. The strategic combination of $BaTiO_3$, $CoFe_2O_4$, and MWCNTs in an epoxy matrix creates a multiphase composite with enhanced broadband RL capabilities. Each nanoparticle uniquely contributes to the composite's electromagnetic wave attenuation, reducing reflection by targeting specific loss mechanisms. Integrating these materials in an epoxy matrix helps achieve impedance matching with free space, thereby reducing the immediate reflection and enhancing the interaction with the nanocomposite. The conductive networks formed by MWCNTs facilitate charge transfer and energy dissipation, while the ferromagnetic and dielectric properties of $CoFe_2O_4$ and $BaTiO_3$ ensure optimal attenuation of both electric and magnetic fields. Additionally, the conductive pathways in MWCNTs promote multiple reflections and enhance localised field intensities, further maximising energy dissipation within the composite. Fine-tuning the nanoparticle's individual compositions can help tailor the electromagnetic properties for a specific frequency range.

The novel contributions from this research work are as follows: The first and foremost addition is the usage of $BaTiO_3$, $CoFe_2O_4$ and MWCNTs combination inside the epoxy matrix for broadband RL applications, which helps in taking advantage of individual nanoparticles exceptional abilities (discussed before). Second, the in-house optimisation tool is used to extract the electromagnetic properties of nanoparticles and the interaction parameters of the nanoparticles in the X-band frequency range using minimal experimental results. Third is the in-house computational tool, which aids in analysing the multiphase composites for reflection loss capabilities under the influence of different polarised EM waves and incident angles. These in-house computational tools and experiments helped identify the influence of individual nanoparticles and their synergic combination on broadband RL capabilities. This research emphasises an integrated experimental-computational approach for designing multiphase nanocomposites for broadband electromagnetic (EM) reflection loss applications. The developed methodology is both novel and versatile, overcoming the limitations of trial-and-error procedures in use and enabling the rapid design of novel multiphase composites with minimal experimental effort. While the input parameters may vary depending on the specific material configurations, the developed in-house tools require only minimal experimental data, enabling efficient optimisation of the inclusions in the new nanocomposite configurations. Now, the organisation of the article is divided into five sections. The methodological approach used in the current study is briefly discussed in Section 2. Section 3 discusses the details of the materials used and the fabrication strategy. Subsequently, the in-house computation tools formulation is detailed in Section 4. Later, the results and conclusions from the experiments & the details of parametric studies performed using the computational tools to analyse the multiphase composites are explained in Sections 5 and 6 respectively.

2. Problem description

The current research proposes a novel integrated approach to designing multiphase composites for detection evasion applications. Fig. 1 presents the methodology implemented to validate the in-house tools and evaluate the influence of the nanoparticles inside the multiphase composite. As mentioned in Section 1, $BaTiO_3$, $CoFe_2O_4$ and MWCNTs are used as the inclusions in the Epoxy-based nanocomposites. Fabricating two-phase nanocomposites ($BaTiO_3$+Epoxy, $CoFe_2O_4$+Epoxy and MWCTNs+Epoxy) with two different volume fractions allowed extraction of the nanoparticle's properties in the X-band frequency range. Electromagnetic characterisation of the fabricated composites is performed using the two-port Vector Network Analyser (VNA) to obtain the nanocomposite scattering parameters, and electromagnetic properties are extracted using the Nicolson-Ross-Weir (NRW) method. The Lichtenecker mixing rule [29] is employed to relate the homogenised composite properties with the properties of epoxy and nanoparticles. The equations relating composite properties with properties of nanoparticles and matrix are shown in Eq. (1). In this equation, ϵ_i and μ_i represent electric permittivity and magnetic permeability of i (c - composite, n - nanoparticle, m - matrix), respectively.

$$\begin{aligned} \epsilon_c^{K_\epsilon} &= f * \epsilon_n^{K_\epsilon} + (1-f) * \epsilon_m^{K_\epsilon} \\ \mu_c^{K_\mu} &= f * \mu_n^{K_\mu} + (1-f) * \mu_m^{K_\mu} \end{aligned} \tag{1}$$

Two two-phase nanocomposite samples are fabricated because the number of unknowns is two, i.e., the property of the nanoparticle and the exponentials (K_ϵ, K_μ) in the mixing rule, which signifies the interaction between the nanoparticles and the matrix. The developed in-house optimisation tool determines these unknown parameters from the mixing rule. The homogenised composite properties (ϵ_r, ϵ_i, μ_r, μ_i) for any arbitrary nanoparticle loading can be obtained using the resulting mixing rule. The in-house tool developed based on the transfer matrix method (TMM) is used to attain the scattering parameters and evaluate the RL, using the effective homogenised properties in the X-band frequency range and the sample's thickness. Both the in-house tools are validated with the experimental results. Subsequently, the compositions of the individual phases in the multiphase composite are varied to attain RL spectra in the X-band frequency range under the incidence of both TE and TM polarised EM waves. A more detailed explanation of the experimental and computational works is elaborated in the subsequent sections.

3. Experimental framework

3.1. Materials

Multi-walled Carbon Nanotubes (MCT) of outer diameter between 10 to 30 nm, lengths between 5 to 10 μm, 98% were purchased from Nanocyl, Belgium. Barium titanate (BTO) and Cobalt ferrite (CFO) nanoparticles having average particle size (APS) of 100 nm and 35 nm, respectively, with a purity of 99.9%, were purchased from Nano research lab, India. The Epoxy and Hardener are purchased from Bhor Chemicals. Acetone (99%) was purchased from Sigma Aldrich. Silicone-based moulds are used to cure the nanocomposite samples.

3.2. Fabrication of composite samples

Two-phase epoxy-based nanocomposites with MCT, BTO, and CFO nanoparticles were fabricated using the solution mixing method. CFO-based and BTO-based nanocomposites of volume fractions 5%, 10%, 15%, 20%, 25% and 30% are farbicated. While MCT-based composites having 5%, 10%, 15%, 20%, 25% and 40% volume fractions have been fabricated. A maximum limit of 30% volume fraction could be fabricated in the case of CTO and BTO nanocomposites because of the very high viscosity of the slurry and limitations of the processing method. The fabrication procedure employed to prepare the nanocomposites of

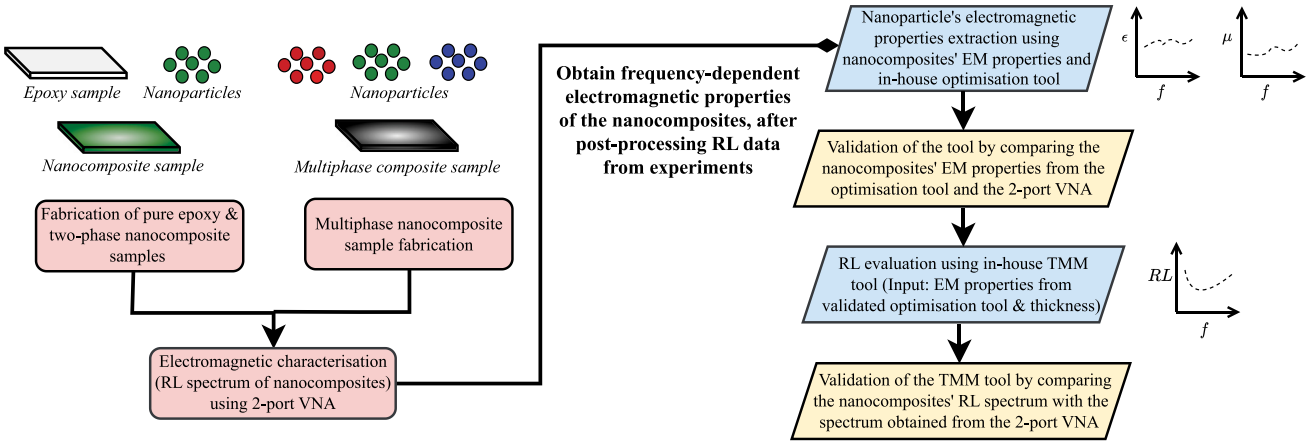

Fig. 1. Schematic represents the flowchart of the methodology implemented to evaluate the influence of the individual phases of the multiphase composite (three nanoparticles - $BaTiO_3$, $CoFe_2O_4$, MWCNTs and Epoxy) on reflection loss spectra. The pink and blue blocks in the flowchart represent the experimental and computational stages, respectively. The yellow blocks represent the validation parts of the in-house tools used in the methodology.

Table 1
Weights of individual phases of $BaTiO_3$ (BTO), $CoFe_2O_4$ (CFO), and MWCNTs (MCT) nanoparticles to achieve two-phase nanocomposites with specified nanoparticle volume fractions (V_f).

Nanoparticles V_f	Individual phases (in grams)			
	Epoxy	BTO	CFO	MCT
05%		02.00	01.75	0.03
10%		04.23	03.69	0.06
15%		06.72	05.86	0.09
20%	5.00	09.53	08.31	0.13
25%		12.70	11.08	0.17
30%		16.33	14.44	–
40%		–	–	0.35

interest is shown in Fig. 2. Nanoparticles were dispersed in acetone and were subjected to probe and bath sonication for 60 min each to break agglomerates of nanoparticles. In another beaker, 5 grams of epoxy was dissolved in acetone at 70 °C at 350 rpm for 20 min using a magnetic stirrer until a uniform solution was formed. The sonicated dispersion of nanoparticles was added to the epoxy solution and stirred at 90 °C until all the acetone evaporated. In the case of the epoxy/CFO nanocomposite, magnetic stirring was avoided due to the ferromagnetic nature of CFO nanoparticles, which could result in uncontrolled particle aggregation under magnetic fields. Instead, a non-magnetic titanium rod was employed for shear mixing, enabling mechanical dispersion by breaking agglomerates and promoting uniform particle distribution Therefore, shear mixing using a titanium-based rod was performed to disperse nanoparticles in the epoxy solution. The prescribed amount of hardener was added to epoxy/nanoparticles dispersion, followed by desiccation under vacuum for 20 min to remove entrapped air bubbles. This dispersion was poured into a silicone mould to cure at room temperature for 24 h, followed by heating in a hot air oven for 12 h at 90 °C. The sample code and their corresponding compositions can be seen in Table 1.

3.3. Characterisation

X-ray diffraction (Rigaku, Smart Lan SE) analysis is carried out on the nanoparticle powders with Cu-K_α of 1.54 Å.To study the XRD peaks, the 2θ scan range is set between 10° to 90° with a scanning rate of 0.7°/min with a step size of 0.01°. Raman (LabRAM HR) analysis is performed with a 532 nm laser on the powdered samples. The acquisition time for the measurements is 20 s, and the analysis is done with a 100x objective lens using an 1800 grating for spectral resolution. TGA (Q 500, TA instruments, USA) was performed to evaluate the volume fraction of the fabricated nanocomposites. Small chunks of mass between 10 to 15 mg are heated from 0 °C to 700 °C at a rate of 5 °C/min to attain the TGA plots. X-ray tomography was performed using the XRadia Versa 500 (Zeiss, USA) at 15 kV. The selected region of the multiphase nanocomposite for analysis had a voxel size of 1.062 μm, with a spatial resolution of 270 μm. Reflection loss studies of the nanocomposite sample with thicknesses between 5.0 mm and 6.0 mm were performed by the Keysight fieldfox microwave analyser (N9918A) within the X-band. S-parameters (S_{11}, S_{12}, S_{21}, and S_{22}) and the phases were obtained from the two-port vector network analyser (VNA).

4. Computational framework

4.1. Optimisation tool

This section describes the optimisation algorithm designed to solve the complex-valued parameter problem. This algorithm is implemented in Python using NumPy, Pandas, and SciPy libraries. Unlike iterative experimental approaches, the proposed optimisation tool combines Nelder–Mead's global search with the Limited-memory-Broyden–Fletcher–Goldfarb–Shanno method (L-BFGS) local convergence to efficiently extract complex-valued electromagnetic properties from minimal experimental data. The overall logic of the in-house tool is given in Fig. 3.

This hybrid approach intends to leverage the advantages and mitigate the disadvantages of individual methods. To understand the criteria behind developing this hybrid optimisation tool, the details of the objective function need to be established. The objective function that needs to be minimised is given in Eq. (2).

$$J(K, P_n) = \sqrt{\text{Mean}(|r_1|^2 + |r_2|^2)} \tag{2}$$

The r_1, r_2 (refer Eq. (3)) values are the difference between the actual effective composite property (P_c) and the evaluated effective property using fibre volume fractions (f_i, g_i), nanoparticle property (P_n), matrix property (P_m), exponential (K). These expressions for r_1, r_2 are for two-phase composite; similarly, expressions can be derived for multiphase composite by including the other particulate's volume fraction. All the properties (P_c, P_n, P_m) are complex-valued, and K, f_i, g_i are scalar parameters.

$$r_1 = P_c - \left[f_i * P_n^K - (1 - f_i) * P_m^K\right]^{1/K} \;\&\; r_2 = P_c - \left[g_i * P_n^K - (1 - g_i) * P_m^K\right]^{1/K} \tag{3}$$

The objective function J presents challenges in the optimisation, such as the domain exploration happens in complex domain for getting the

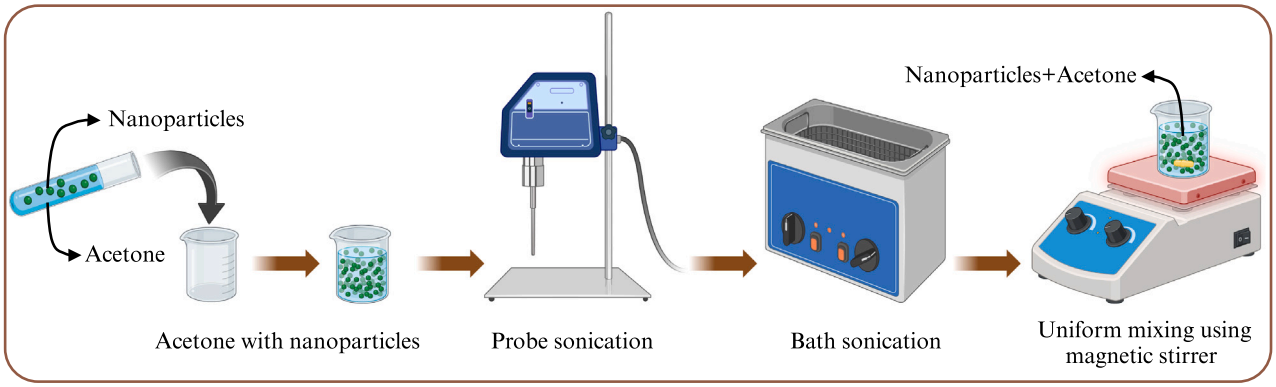

(a) Dispersion of nanoparticles inside acetone using probe and bath sonicators.

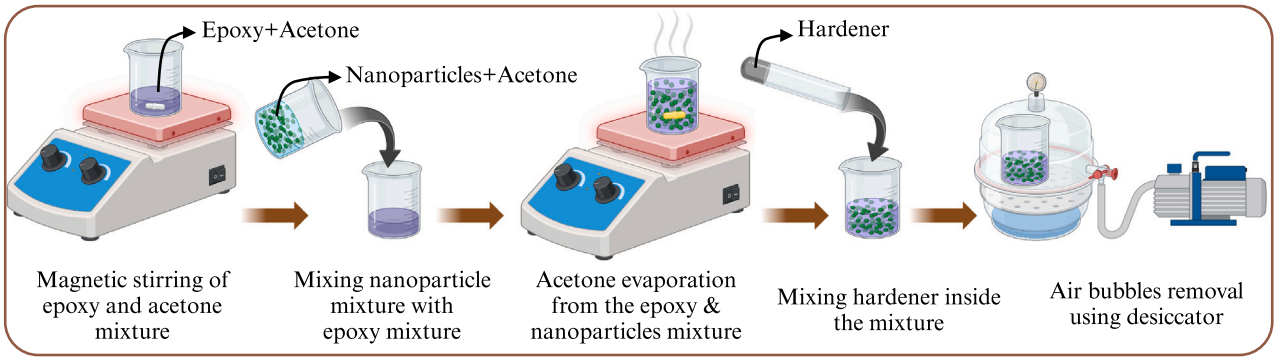

(b) Mixing of nanoparticles and epoxy along with evaporation of the acetone.

Fig. 2. Different stages of solution mixing method to attain uniformly dispersed nanoparticles and epoxy mixture to fabricate the nanocomposite samples.

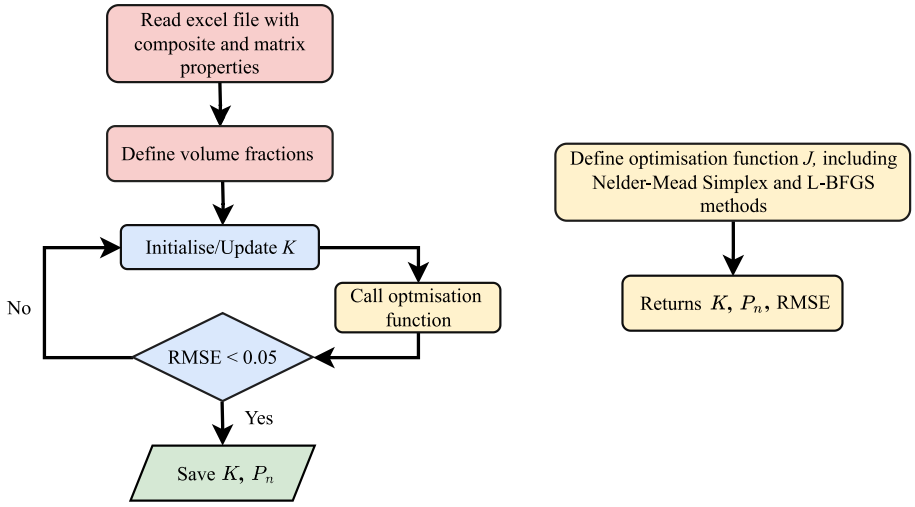

Fig. 3. Flowchart of the in-house optimisation tool used to extract the interaction parameters (K) and the material properties (P_n).

P_c. The objective function has inherent non-linearity because of the P_n^K. Due to complex exponential, the error landscape can be non-convex, resulting in multiple local minima. Small variations in the K can result in large variations in P_n and can also result in ill-conditioning.

The effectiveness of the Nelder–Mead method in the first stage is attributed to the fact that it is a derivative-free optimisation algorithm that is apt for non-smooth, noisy environments. The Nelder–Mead method is suitable for potentially non-convex regions caused by the non-linear P_n^K term. It helps find the favourable region in the parameter space, even if there are many local optima. This method helps find good initial guess values for P_n vector across the X-band frequency range. However, the Nelder–Mead method's convergence rate will be slow in the regions close to the optimum in high-dimensional areas. L-BFGS method convergence tends to be an issue due to potential non-convexity issues if it starts with a poor initial guess. The L-BFGS used in the second stage is a quasi-Newton technique similar to BFGS using limited memory. It has the property of fast local convergence, which is very effective for the final iteration. The method's applicability to large-scale problems proves useful when working with high-dimensional P_n vectors. Consequently, Nelder–Mead's inherent characteristic of global search enriches L-BFGS's local optimisation performance. This combination allows for a good approximate solution with Nelder–Mead and a

high-precision solution with L-BFGS. The K parameter is varied using a grid search over the range [0, 5]. The input complex-valued vectors P_c, P_m are scaled by their maximum absolute value to improve the numerical stability. An early termination check is implemented, which stops the search if the solution has a root mean squared error (RMSE) lower than 0.05. This feature potentially reduces computational time without significantly compromising solution accuracy. The organised search through the K-space can aid in finding the global optimum in cases where there are multiple local optima, which might occur due to the complex nature of the objective function involving powers of complex numbers.

In conclusion, this optimisation approach combines the Nelder–Mead method's excellent global optimisation capacities with L-BFGS's highly efficient, local converging characteristic, making it a remarkably effective problem-solving model. Specifically, it is designed to compute gradients and the Hessian of the objective function, which might be complex-valued, non-linear, and non-convex, and learn parameters with mutual dependency, indicating the potential for numerical instability. Therefore, the algorithm becomes a powerful means of performing the parameter estimation of the systems described by the complex-valued equations in various applications of signal processing, electromagnetics and diverse areas where a study on complex-valued data is carried out.

4.2. Reflection loss evaluation

This section explains the formulation used to evaluate the composite samples' scattering parameters and reflection loss. Compared to computationally intensive methods like finite element modelling used in composite design, the modified TMM approach provides a semi-analytical solution optimised for layered structures, is computationally efficient, fast & memory efficient. However, the proposed method is suitable only for homogeneous structures, and the structure is assumed to be periodic in the x and y directions. In the conventional transfer matrix method, the electromagnetic (EM) wave modes travelling only in the forward direction will be considered, resulting in instability. In this formulation proposed by Rumph [30], the distinction between forward and backward EM waves will be considered while solving the Maxwell equations. The electric and magnetic fields will be normalised in the conventional curl equations because the ratio of fields is related to the impedance of the medium, which is of order two. Along with the fields, the wave numbers and dimensions involved are also normalised to maintain the same order of magnitude, which helps improve the accuracy and reduce the numerical errors. Assuming the plane EM wave is propagating in the +z direction. The normalised curl equations, using Ampere's and Faraday's induction law, are shown in Eq. (4).

$$\begin{aligned} \nabla \times \vec{E} &= -j\omega\mu(\omega)\vec{H} = -j\omega\mu_0\mu_r(\omega)\vec{H} = K_0\mu_r(\omega)\vec{\tilde{H}} \\ \nabla \times \vec{\tilde{H}} &= j\omega\epsilon(\omega)\vec{E} = j\omega\epsilon_0\epsilon_r(\omega)\vec{E} = K_0\epsilon_r(\omega)\vec{E} \\ \text{where, } \vec{\tilde{H}} &= -j\sqrt{\frac{\mu_0}{\epsilon_0}}\vec{H} \end{aligned} \tag{4}$$

In Eq. (4), $\vec{E}$ and $\vec{H}$ represent the electric and magnetic fields, respectively. K_0, ϵ_0, μ_0 represent free space's wave number, electrical permittivity and magnetic permeability, respectively. Whereas $\epsilon_r(\omega)$, $\mu_r(\omega)$ represent materials relative electrical permittivity and relative magnetic permeability, respectively, which are frequency (ω) dependent. By considering the structure to be periodic in the x and y directions, the partial differentiation of electric and magnetic fields can be replaced as shown in Eq. (5).

$$\frac{\partial\vec{E}}{\partial x} = jK_x\vec{E}, \quad \frac{\partial\vec{E}}{\partial y} = jK_y\vec{E}, \quad \frac{\partial\vec{H}}{\partial x} = jK_x\vec{H}, \quad \frac{\partial\vec{H}}{\partial y} = jK_y\vec{H} \tag{5}$$

By simplifying the six partial differential equations given in Eq. (4) and using the relationships in Eq. (5), equations can be reduced to a single second-order differential equation as shown in . Where, $\tilde{z}$ and wave number $\tilde{K}_j$ are normalised using K_0 ($\tilde{z} = K_0 z$, $\tilde{K}_j = K_j/K_0$). The subscript j in the wave number represents the direction. The superscript L used in all the symbols used in this work corresponds to the composite layer L.

$$\begin{aligned} &\frac{d^2}{d\tilde{z}^2}\begin{bmatrix}E_x\\E_y\end{bmatrix} = P_E^L\frac{d}{d\tilde{z}}\begin{bmatrix}\tilde{H}_x\\\tilde{H}_y\end{bmatrix} = P_E^L Q_H^L\begin{bmatrix}E_x\\E_y\end{bmatrix} = \Lambda^2\begin{bmatrix}E_x\\E_y\end{bmatrix} \\ &\text{Where, } P_E^L = \frac{1}{\epsilon_r^L(\omega)}\begin{bmatrix}\tilde{K}_x\tilde{K}_y & \mu_r^L(\omega)\epsilon_r^L(\omega) - \tilde{K}_x{}^2 \\ \tilde{K}_y{}^2 - \epsilon_r^L(\omega)\mu_r^L(\omega) & -\tilde{K}_x\tilde{K}_y\end{bmatrix} \\ &\text{Where, } Q_H^L = \frac{1}{\mu_r^L(\omega)}\begin{bmatrix}\tilde{K}_x\tilde{K}_y & \mu_r^L(\omega)\epsilon_r^L(\omega) - \tilde{K}_x{}^2 \\ \tilde{K}_y{}^2 - \epsilon_r^L(\omega)\mu_r^L(\omega) & -\tilde{K}_x\tilde{K}_y\end{bmatrix} \end{aligned} \tag{6}$$

Considering the EM wave's forward and backwards modes, the differential equation's solution can be seen in Eq. (7). Λ is a matrix, and to evaluate the exponential of the matrix, the principal component analysis method (f(matrix) = eigenvector matrix*f(eigenvalue matrix)*inverse of eigenvector matrix) is used. In Eq. (7), χ and λ represent the eigenvector and eigenvalues matrices of Λ, respectively. a^+ and a^- represent the proportionality constants for forward (+z) and backward (-z) waves. c^+ and c^- represent the amplitude coefficient of each electromagnetic mode in forward and backward directions, respectively.

$$\begin{bmatrix}E_x(\tilde{z})\\E_y(\tilde{z})\end{bmatrix} = e^{-\Lambda\tilde{z}}a^+ + e^{\Lambda\tilde{z}}a^- = \chi e^{-\lambda\tilde{z}}\chi^{-1}a^+ + \chi e^{\lambda\tilde{z}}\chi^{-1}a^- = \chi e^{-\lambda\tilde{z}}c^+ + \chi e^{\lambda\tilde{z}}c^- \tag{7}$$

Similar to the solution for the electric field solution given in Eq. (7) for the second-order different equation in terms of the electric field (), the solution for the magnetic field can be seen in Eq. (8). The physical significance of the eigenvector matrices (χ and ξ) is that they represent the relative amplitudes of E_x, E_y, H_x and H_y of the electromagnetic modes. The exponential of the eigenvalue matrices in Eq. (7) and Eq. (8) describe how the modes are propagating (decaying or growing nature). Meanwhile, the amplitude coefficients (c^+ and c^-) in the equations quantify how much energy is contained in each mode.

$$\begin{bmatrix}\tilde{H}_x(\tilde{z})\\\tilde{H}_y(\tilde{z})\end{bmatrix} = e^{-\Lambda\tilde{z}}a^+ + e^{\Lambda\tilde{z}}a^- = -\xi e^{-\lambda\tilde{z}}\xi^{-1}a^+ + \xi e^{\lambda\tilde{z}}\xi^{-1}a^- = -\xi e^{-\lambda\tilde{z}}c^+ + \xi e^{\lambda\tilde{z}}c^- \tag{8}$$

Combining Eqs. (7) and (8), the combined field of the composite layer L can be written in a single matrix (refer Eq. (9)). Considering the physical boundary conditions, the tangential components of electric (E_x, E_y) and magnetic ($\tilde{H}_x$, $\tilde{H}_y$) fields will always be continuous across the interface, but the normal components (E_z, $\tilde{H}_z$) will be discontinuous. As the normal components were eliminated from the assumptions made in formulating the transfer matrix method, the field described in Eq. (9) can be considered for ensuring the physical boundary continuity at the interfaces. Inside the sample holder of the two-port VNA setup, the composite sample will be surrounded by the free space on both sides; a similar setup is shown as a schematic in Fig. 4(a).

$$\psi^L(\tilde{z}) = \begin{bmatrix}E_x(\tilde{z})\\E_y(\tilde{z})\\\tilde{H}_x(\tilde{z})\\\tilde{H}_y(\tilde{z})\end{bmatrix}^L = \begin{bmatrix}\chi & \chi\\-\xi & \xi\end{bmatrix}^L\begin{bmatrix}e^{-\lambda\tilde{z}} & 0\\0 & e^{\lambda\tilde{z}}\end{bmatrix}^L\begin{bmatrix}c^+\\c^-\end{bmatrix}^L \tag{9}$$

The boundary conditions can be applied as mentioned in Eq. (10) (superscripts represent the medium on both sides of the composite laminate of layer L). Enforcing these boundary conditions using the field expression shown in Eq. (9), the mode coefficients on the left side will be related to the ones on the right (in the conventional transfer matrix method). In this modified method, the matrices can be rearranged, and the input mode coefficients (c_1^+, c_2^-) will be related to the output mode coefficients (c_1^-, c_2^+). The matrix relating these input and output mode coefficients is nothing but the scattering matrix ($S^{(L)}$), which is similar to what is obtained from the two-port VNA setup. These elements in the scattering matrix also have a physical meaning,

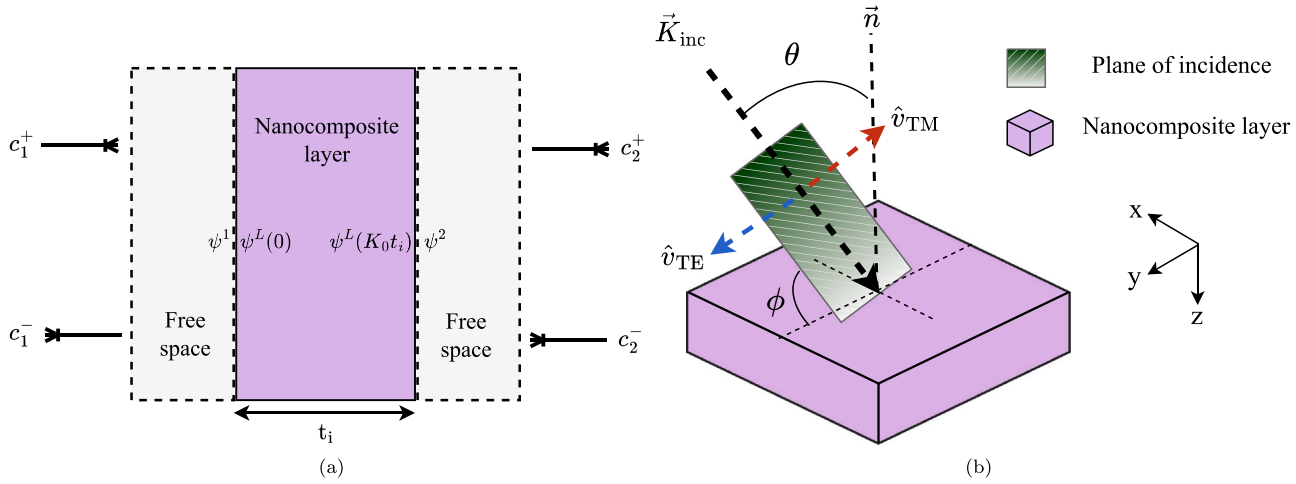

Fig. 4. (a) Schematic representing the nanocomposite of thickness t_i placed between the free space and the physical boundary conditions of the electromagnetic field (ψ^i) at the interfaces of the layers. (b) Schematic representation of the electromagnetic wave incident on a nanocomposite layer. The incident wave vector $\vec{K}_{inc}$ impinges on the layer at an angle θ relative to the surface normal $\vec{n}$ with, $\hat{v}_{TE}$ and $\hat{v}_{TM}$ representing the unit vectors of transverse electric (TE) and transverse magnetic (TM) components, respectively. The angles θ, ϕ define the orientation of the incident wave relative to the nanocomposite layer.

whereas the elements in the transfer matrix will not have any physical meaning.

$$\psi^1 = \psi^L(0) \quad \& \quad \psi^L(K_0 t_i) = \psi^2 \tag{10}$$

If multiple composite layers are inside the free space, scattering matrices of individual layers can be obtained. Then, the Redheffer star product can be used to obtain the global scattering matrix. The expression for evaluating the global matrix, if there are n composite layers, can be seen in Eq. (11). This global matrix relates the mode coefficients on the reflection (c_{ref}) and transmission (c_{trans}) side to the incidence mode coefficient (c_{inc}). If the comparison is made between the mode coefficients, then c_1^+ and c_2^- are the incidence mode coefficients (c_{inc}), but in two-port VNA setup, the EM waves are incident from only one direction that is port 1, therefore c_2^- will be set to zero in the analysis. c_1^- and c_2^+ are the reflection (c_{ref}) and transmission coefficients (c_{trans}) respectively. Therefore, the resulting global scattering matrix relating these mode coefficients, consistent with the two-port VNA testing, is shown in Eq. (11).

$$S^{(G)} = S^{(L1)} \otimes S^{(L2)} \otimes S^{(L3)} \otimes \cdots \ldots S^{(Ln)}$$
$$\begin{bmatrix} c_{ref} \\ c_{trans} \end{bmatrix} = \begin{bmatrix} S_{11}^{(G)} & S_{12}^{(G)} \\ S_{21}^{(G)} & S_{22}^{(G)} \end{bmatrix} \begin{bmatrix} c_{inc} \\ 0 \end{bmatrix} \tag{11}$$

As the global scattering matrix can be obtained from the material properties and the thickness of the composite layers, the incidence mode coefficient is unknown in the equation when evaluating the reflection and transmission coefficients. To attain the c_{inc}, the simplification used in Eq. (7) can be used ($c = \chi^{-1}a$). In this expression, a is nothing but the proportionality constant or the incidence electric field. The electric field components in the x and y directions are the components of the polarisation vectors in the x and y directions (refer Eq. (12)). Using Eq. (7), Eq. (11) and the relation between c_{inc} and polarisation components, the electric field components in reflection and transmission regions are obtained, as shown in Eq. (12).

$$c_{inc} = \chi_{inc}^{-1}\, \psi^L(0) = \chi_{inc}^{-1} \begin{bmatrix} E_{x,inc} \\ E_{y,inc} \end{bmatrix} = \chi_{inc}^{-1} \begin{bmatrix} P_x \\ P_y \end{bmatrix}$$
$$c_{ref} = \chi_{ref}^{-1} \begin{bmatrix} E_{x,ref} \\ E_{y,ref} \end{bmatrix} \implies \begin{bmatrix} E_{x,ref} \\ E_{y,ref} \end{bmatrix} = \chi_{ref}\, c_{ref} = \chi_{ref}\, S_{11}^{(G)}\, c_{inc}$$
$$c_{trans} = \chi_{trans}^{-1} \begin{bmatrix} E_{x,trans} \\ E_{y,trans} \end{bmatrix} \implies \begin{bmatrix} E_{x,trans} \\ E_{y,trans} \end{bmatrix} = \chi_{trans}\, c_{trans} = \chi_{trans}\, S_{21}^{(G)}\, c_{inc} \tag{12}$$

Linear polarised waves sent from the plane wave source can be either transverse electric (TE) or transverse magnetic (TM) polarised with respect to the composite structure. In TE polarisation, the electric field vector is polarised perpendicular to the plane of incidence. TM polarised magnetic waves will be parallel to the plane of incidence. The composite polarisation vector ($\vec{P}$), including both the transverse electric (TE) and transverse magnetic (TM) polarised vectors, can be seen in Eq. (13). Using the components of the polarisation vector, the electric field amplitudes mentioned in Eq. (12) are obtained. The scattering parameters which are obtained in Eq. (11) cannot be used directly because the longitudinal component of the electric field is still not yet incorporated in the analysis. To evaluate the longitudinal component ($E_{z,inc}$, $E_{z,ref}$, $E_{z,trans}$), the Gauss law or the zero divergence ($\nabla.\vec{E} = 0$) law can be used. Using the electric field components in all directions, both reflection (R) and transmission (T) are obtained using the formulation mentioned in [31]. Using these components, the reflection loss (RL = $10^*\log_{10}$(R)) can be obtained.

$$\vec{P} = P_{TE}\hat{v}_{TE} + P_{TM}\hat{v}_{TM}$$
$$\hat{v}_{TE} = \frac{\vec{K}_{inc} \times \vec{n}}{|\vec{K}_{inc} \times \vec{n}|} \quad \& \quad \hat{v}_{TM} = \frac{\hat{v}_{TE} \times \vec{K}_{inc}}{|\hat{v}_{TE} \times \vec{K}_{inc}|} \tag{13}$$

However, in the two-port VNA setup, there is no TE and TM polarisation kind of treatment; only waveguide modes are possible. The two-port VNA setup used for the experiments is a WR 90 rectangular waveguide in which TE_{10} mode is the dominant mode with the lowest cutoff frequency of 6.56 GHz. The operation X-band frequency range is below the cutoff frequency of the possible higher modes and attenuates quickly. This attenuation of higher modes helps accurately measure the scattering parameters. This TE_{10} mode can be approximately taken as a TE polarised wave. Because in TE_{10} mode, the electric field component will be only along y-direction (similar to TE polarised wave at normal incidence). This E_y component will vary sinusoidally along the x-axis, but it is uniform along the z-axis ($E_y = E_0 \sin(\pi x/a)\, e^{-j\beta z}$). This sinusoidal variation is maximum at the centre of the sample holder (x=a/2), equivalent to what is observed in TE polarised wave ($E_y = E_0\, e^{-j\beta z}$). For all the testing, the samples are placed at the centre of the sample holder to ensure this kind of correspondence. The placement of the sample in the middle of the holder, where the field intensity is at or near its maximum, ensures that the sample experiences a field distribution that a uniform plane wave can closely approximate.

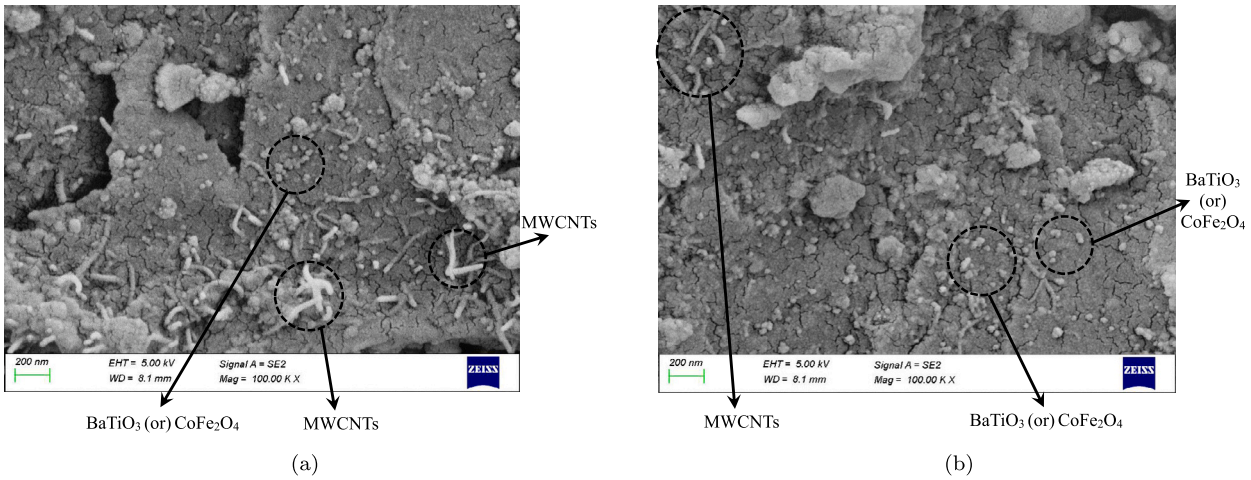

Fig. 5. Scanning Electron Microscopy (SEM) images of multiphase nanocomposite showing the spherical nanoparticles (BTO and CFO) and multi-walled carbon nanotubes (MCT) at 100k magnification at two different locations, illustrating the morphology and dispersion of the material's inclusions. The scale bar represents 200 nm.

5. Results and discussion

5.1. Characterisation results

The crystal structure and phase composition of the $BaTiO_3$, $CoFe_2O_4$ and MWCNTs were investigated using X-ray diffraction (XRD) analysis and Raman spectra (refer Figs. A1–A3). The detailed description and the relevant plots are presented in Appendix. The morphological and elemental characterisation of the individual phases in the multiphase composite was performed using Scanning Electron Microscopy (SEM) and Energy-dispersive X-ray Spectroscopy (EDS). The SEM images shown in Fig. 5 obtained at 100K magnification show the dispersion of the spherical nanoparticles of BTO, CFO and tubular configurations of MCT at two different locations in the cross-section of the manually broken composite sample. These morphologies and particle sizes of individual phases can be seen in Fig. A4 in the Annexure. Fig. A4 depicts the SEM images of the CFO, BTO and MCT nanocomposites obtained at 100K and 50K magnifications. At 100K magnification, the particle sizes are mentioned in Figs. A4(a), A4(c) and A4(e). From Fig. A4(a), it can be identified that the BTO particle sizes vary from 100 nm to 153 nm with an average size of approximately 120 nm. Fig. A4(c) shows that the CFO particle sizes vary from 55 nm to 200 nm with an average size of approximately 115 nm. From Fig. A4(e), it is observed that the MCT length and diameter are approximately 245 nm and 20 nm.

To further investigate the elemental composition and confirm the presence of the various phases, elemental mapping was performed on the selected region, which is shown in Fig. 6. The corresponding elemental maps for Ba, Ti, Co, Fe, C, and O, shown in Fig. 6, confirm the distribution of each element. Ba and Ti distribution indicate the presence of $BaTiO_3$, Co and Fe corresponds to $CoFe_2O_4$, while the carbon distribution is attributed to the presence of both the MWCNTs and the epoxy matrix. The oxygen distribution aligns with both the oxides present in the composite phases and the epoxy matrix. Additionally, the EDS spectrum in Fig. 6 provides a detailed quantitative analysis of the elements in the composite. The major peaks correspond to Ba (19.01 wt%), Ti (21.00 wt%), Co (04.33 wt%), Fe (06.02 wt%), C (26.95 wt%), and O (22.70 wt%). The atomic percentages of these elements indicate the composition of the desired phases within the composite, with a predominant presence of carbon due to the MWCNTs and the epoxy matrix. Elemental mapping and point EDS spectrum of the two-phase composites is also carried out to confirm the elements and their distribution. Figs. A5, A6, and A7 show the mapping of BTO, CFO and MCT-based composites, respectively.

The X-ray computed tomography (CT) scanning was conducted at a voltage of 140 kV and a power of 10 W, ensuring sufficient penetration of the X-rays through the dense composite materials. Image acquisition was conducted using a 4× objective lens with HE1 source filtering and normal field mode. The scanning is carried out for almost seven hours with a bin setting of 2 and an exposure time of 10 s per projection to achieve optimal contrast between the different phases. X-ray CT was performed to analyse the internal structure and phase distribution of the multiphase nanocomposite consisting of $BaTiO_3$, $CoFe_2O_4$, MWCNTs, and an epoxy matrix. Fig. 7 illustrates the setup and results of the X-ray CT scan. In Fig. 7(a), the placement of the sample inside the scanning chamber is shown, demonstrating the sample's alignment for detailed imaging. Fig. 7(b) provides a reference X-ray CT image of the scanned region, highlighting the selected area for analysis with a pixel size of 1.062 μm and spatial resolution of 270 μm. Figs. 7(c) and 7(d) present the three-dimensional and cross-sectional views of the multiphase nanocomposite. The densities and the particle sizes of the $BaTiO_3$ and $CoFe_2O_4$ are very close, so there is not much colour contrast to distinguish between these nanoparticles. Because of the density contrast between MCT, Epoxy and ceramic nanoparticles, the colour contrast between these phases is more clearly visible. These images illustrate the internal distribution of $BaTiO_3$ or $CoFe_2O_4$ (yellow regions), MWCNTs (red regions), and the epoxy matrix (purple regions). The distinct phases are clearly identifiable, with $BaTiO_3$, $CoFe_2O_4$ particles appearing well-dispersed throughout the matrix, while MWCNTs form a network embedded within the epoxy. This analysis shows the uniformity of the nanoparticles inside the epoxy of the multiphase nanocomposite and provides insights into the distribution and phase interactions at the microstructural level. Micro CT analysis is also employed to investigate the microstructure of two-phase nanocomposites, composed of BTO and CFO nanoparticles. The scanning was performed using an X-ray computed tomography (CT) system operated at 160 kV and 10 W power, ensuring adequate X-ray penetration through the dense composite materials. Image acquisition utilised a 4× and 20× for BTO and CFO nanocomposites, respectively. The scan duration extended to approximately nine hours with a bin setting of 2 & an exposure time of 7.5 and 16 s per projection for BTO and CFO nanocomposites to optimise phase contrast. Complementary SEM analysis revealed that the average particle sizes of BTO and CFO were approximately 120 nm, while multi-walled carbon nanotubes (MWCNTs) exhibited diameters of ≈20 nm. Due to the significant size disparity between the ceramic nanoparticles and MWCNTs, identifying individual nanotubes within the multiphase nanocomposites (comprising BTO, CFO, MWCNTs, and epoxy matrix) proved challenging in

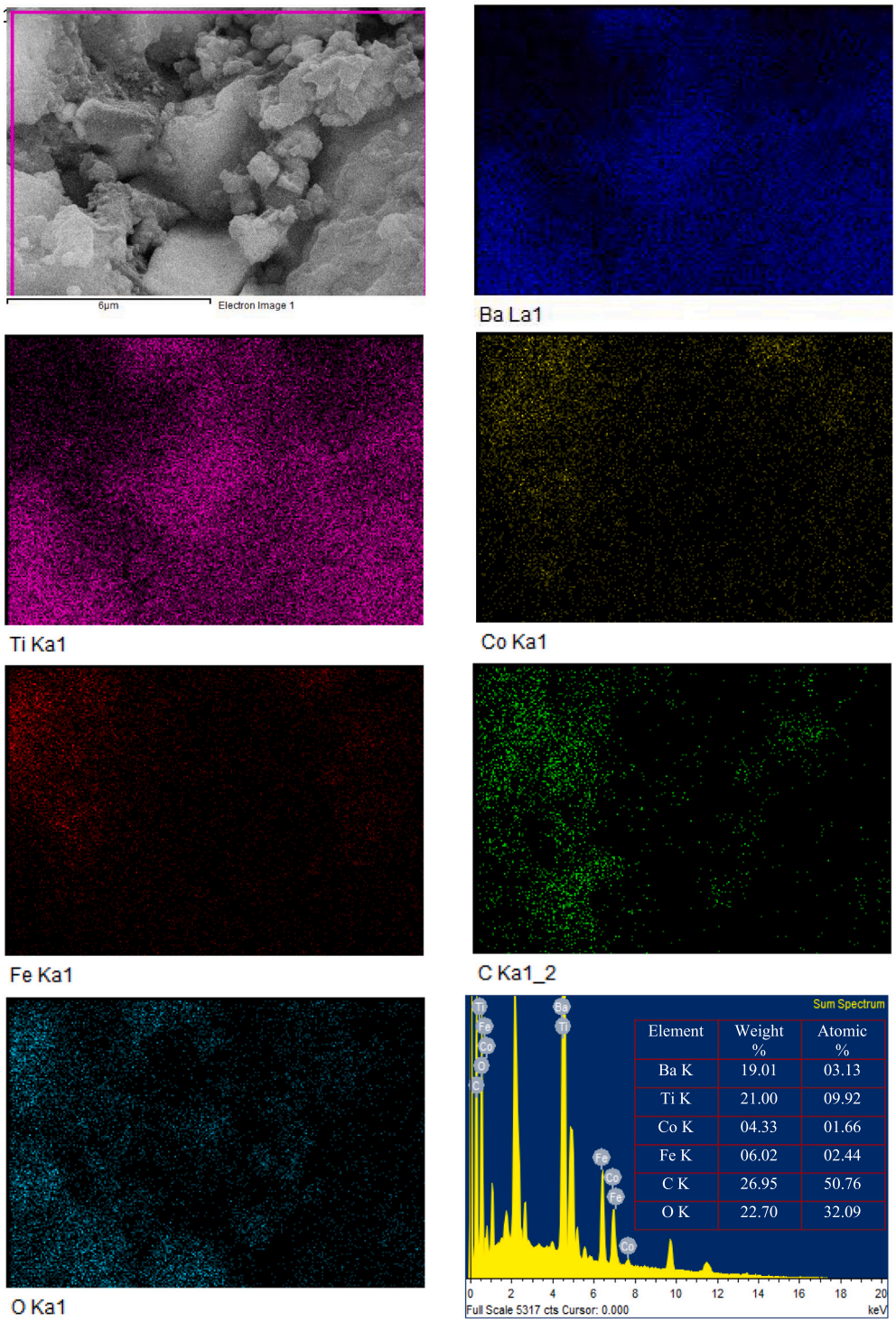

Fig. 6. EDS elemental mapping of Ba-L, Ti-K, Co-K, Fe-K, C-K, O-K of multiphase composite in the region selected in the SEM image is shown. The EDS spectrum of the mixed composites with different elements is shown in the graph, with the *X*-axis representing energy in keV and the *Y*-axis showing the counts of detected X-rays. Major peaks correspond to the elements present in the sample, including barium (Ba), titanium (Ti), cobalt (Co), iron (Fe), carbon (C), and oxygen (O). A table is provided with the weight percentage and atomic percentage of each element in the image area selected.

micro-CT images. Consequently, micro-CT analysis was excluded for MWCNT-incorporated composites. The videos obtained from the micro-CT analysis are included in the supplementary data to visualise the 3D distributions of the nanoparticles inside both two-phase and multiphase nanocomposites.

TGA analysis is performed, and the actual volume fraction of the fabricated composite samples is obtained. The particles are also degrading along with the epoxy; therefore, the degradation of the pure particles is also taken into account, and Eq. (14) is used to evaluate the volume fractions of the two-phase composite (BTO, CFO and MCT). Densities of BTO, CFO, Epoxy and MCT are 6.02, 5.25, 1.08 and 0.0834 gram/cm^3 respectively. In Eq. (14), m_i represents the remaining mass

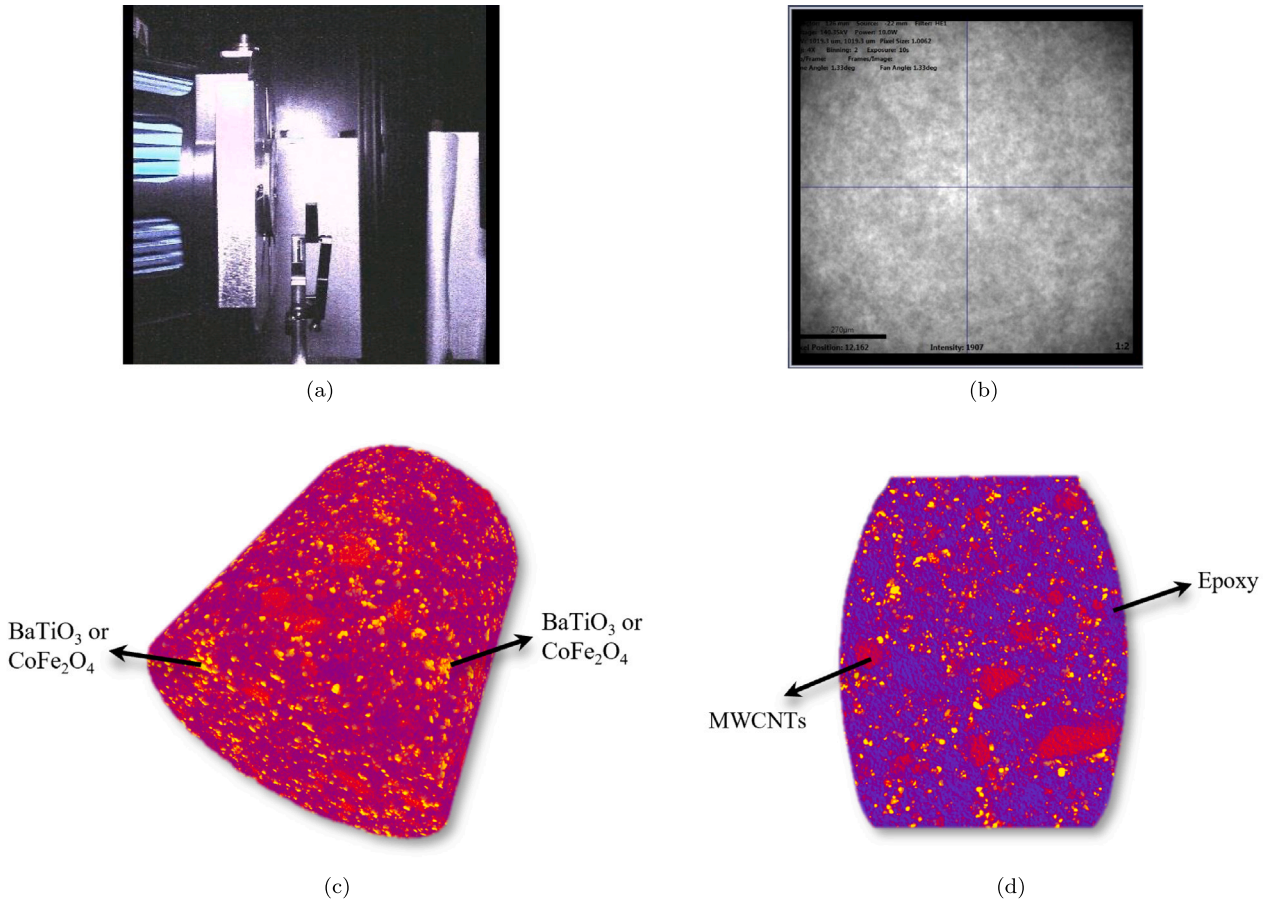

Fig. 7. (a) The image highlights the placement of multiphase nanocomposite within the scanning chamber placed inside the X-ray Computed Tomography (CT) equipment. The setup shows the sample positioned for scanning, allowing for detailed imaging and phase analysis. (b) X-ray CT scan reference image of the scanned area in the multiphase nanocomposite. The image shows the selected region for analysis with a pixel size of 1.062 μm and a spatial resolution of 270 μm. (c) shows the 3-D view, and (d) shows the cross-sectional view of the multiphase nanocomposite, showing the phase distribution and material density variations. The colour mapping highlights distinct phases within the composite, with yellow, red and purple indicating $BaTiO_3$ or $CoFe_2O_4$, MWCNTs, and epoxy, respectively.

fraction of phase i at 700° and ρ_i represents the density of phase i. Where X is the remaining mass fraction of the particles inside the fabricated composites.

$$m_{\text{particles}}(X) + m_{\text{epoxy}}(1-X) = m_{\text{composite}}$$

$$\text{Actual volume fraction of the particles} = \frac{\dfrac{X}{\rho_{\text{particles}}}}{\left(\dfrac{X}{\rho_{\text{particles}}} + \dfrac{1-X}{\rho_{\text{epoxy}}}\right)} \quad (14)$$

TGA plots of BTO, CFO and MCT samples along with their pure phases degradation, shown in Fig. A8. The remaining mass percentages (at 700°) of the pure phases and composite samples are obtained from the TGA plots and shown in Table 2. A comparison between the required and actual volume fractions of the two-phase and multiphase composites is given in Table 3. The small discrepancies between required and actual volume fractions (e.g., 19.799% vs. 20% for BTO20) confirm the reliability of the fabrication process. These minor variations, within 1%–4%, suggest high repeatability in sample preparation, which is critical for consistent electromagnetic property measurements.

5.2. Validation of in-house computational tools

The scattering values and the phase are obtained from testing the composite samples using a two-port VNA in the X-band frequency range. Before measuring the samples, a full two-port TRL calibration is performed in the X-band frequency. The sample holders used for the measurement are clamped tightly between the waveguide adaptors, and the complex scattering parameters are measured. Using these scattering parameters as the input, the real and imaginary parts of the permittivity and permeability of the fabricated samples are obtained using the standard Nicolson-Ross-Weir (NRW) algorithm. The thickness of the sample plays a critical role in the accuracy and reliability of material property extraction using the NRW method based on S-parameters measured in the X-band (8.2–12.4 GHz). For the NRW method, to avoid phase ambiguity and ensure accurate extraction, maximum sample thickness should be no more than a quarter of the wavelength ($\lambda/4$). Since the characterisation is carried out in the X-band, the shortest wavelength (i.e., highest frequency = 12.4 GHz) gives the most conservative quarter-wavelength or thickness limit ≈ 6.05 mm. Therefore, the range of all the composite samples is maintained between 5.0 and 6.0 mm. The variation of the electromagnetic properties in the X-band frequency range is minimal (nearly constant); therefore, the average values across the frequency are represented in all the plots. Fig. 8 shows the extracted material properties.

It can be observed that the real part of permittivity (ϵ') of all the composite samples with different inclusions is always greater than the permittivity of the pure epoxy. For 5% volume fraction samples, the influence of the inclusions on the effective properties will be less, which

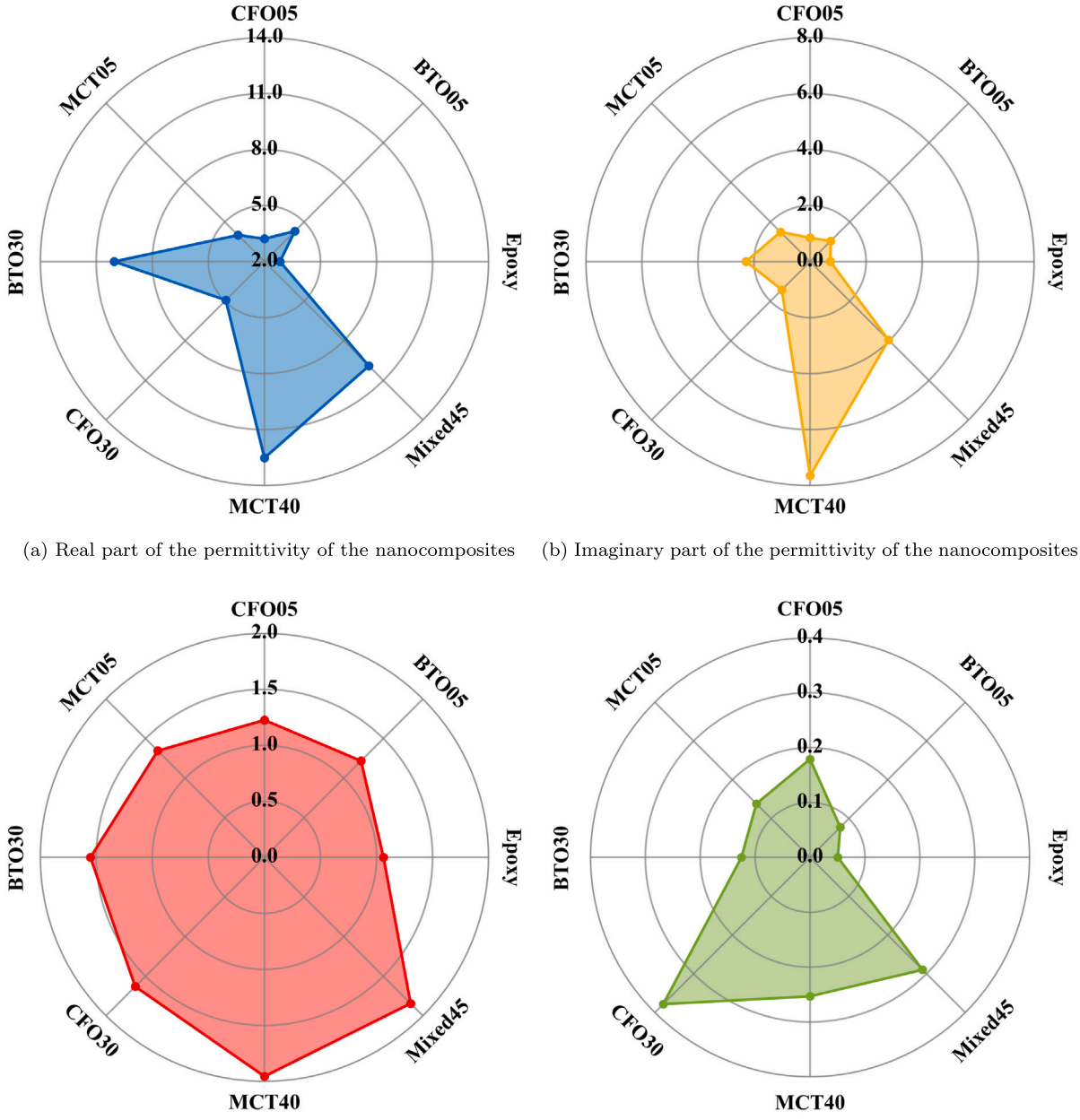

(a) Real part of the permittivity of the nanocomposites

(b) Imaginary part of the permittivity of the nanocomposites

(c) Real part of the permeability of the nanocomposites

(d) Imaginary part of the permeability of the nanocomposites

Fig. 8. Electromagnetic properties of nanocomposites in comparison with pure epoxy obtained from experiments. Where Mixed45 contains 15% MWCNTs, 15% $BaTiO_3$ and 15% $CoFe_2O_4$ nanoparticles inside epoxy.

is evident from Figs. 8(a), 8(b), 8(c) and 8(d). The exact influence of the inclusion particulates is visible only at higher volume fractions. The real part and imaginary parts of the permittivity (ϵ' and ϵ^{ε}) of MCT samples are greater than the CFO and BTO nanocomposite samples at higher volume fractions, which can be seen in Figs. 8(a) and 8(b). From the literature works, it is known that the magnetic permeability of cobalt ferrite will be greater than barium titanate; this is evident from Figs. 8(c) and 8(d) that CFO samples have higher value than BTO samples. Unlike the real part of permittivity, which is more than 2 for all the samples, including the epoxy, the real part of magnetic permeability (μ') is within the range of 1 to 2. Similarly, the imaginary part of the magnetic permeability (μ^{ε}) is less than 0.4 for all the composite samples considered. The imaginary value of the magnetic permeability of CFO30 is greater than MCT40 and mixed sample with 45% volume fraction, which shows how much cobalt ferrite will contribute to the magnetic losses in the overall absorption of the incident electromagnetic waves.

Using the properties of Epoxy, BTO05 and BTO30, the BTO nanoparticles properties are obtained using the optimisation tool described in Section 4.1. Similarly, the electromagnetic properties of CFO and MCT nanoparticles are also attained using the in-house tool using CFO05, CFO30 and MCT05, MCT40 composite samples, which can be seen in Fig. 9. The interaction parameter K obtained from the tool for the electrical permittivity (ϵ) and magnetic permeability (μ) of the BTO-based composites is 1.280 and 4.477, respectively. K for the ϵ and μ of the CFO composites is 1.973 and 4.130, respectively. Similarly, K for the ϵ and μ of the MCT composites is 0.866 and 4.521, respectively. It can be observed that the ϵ'' is close to ϵ' only for MCT nanoparticles.

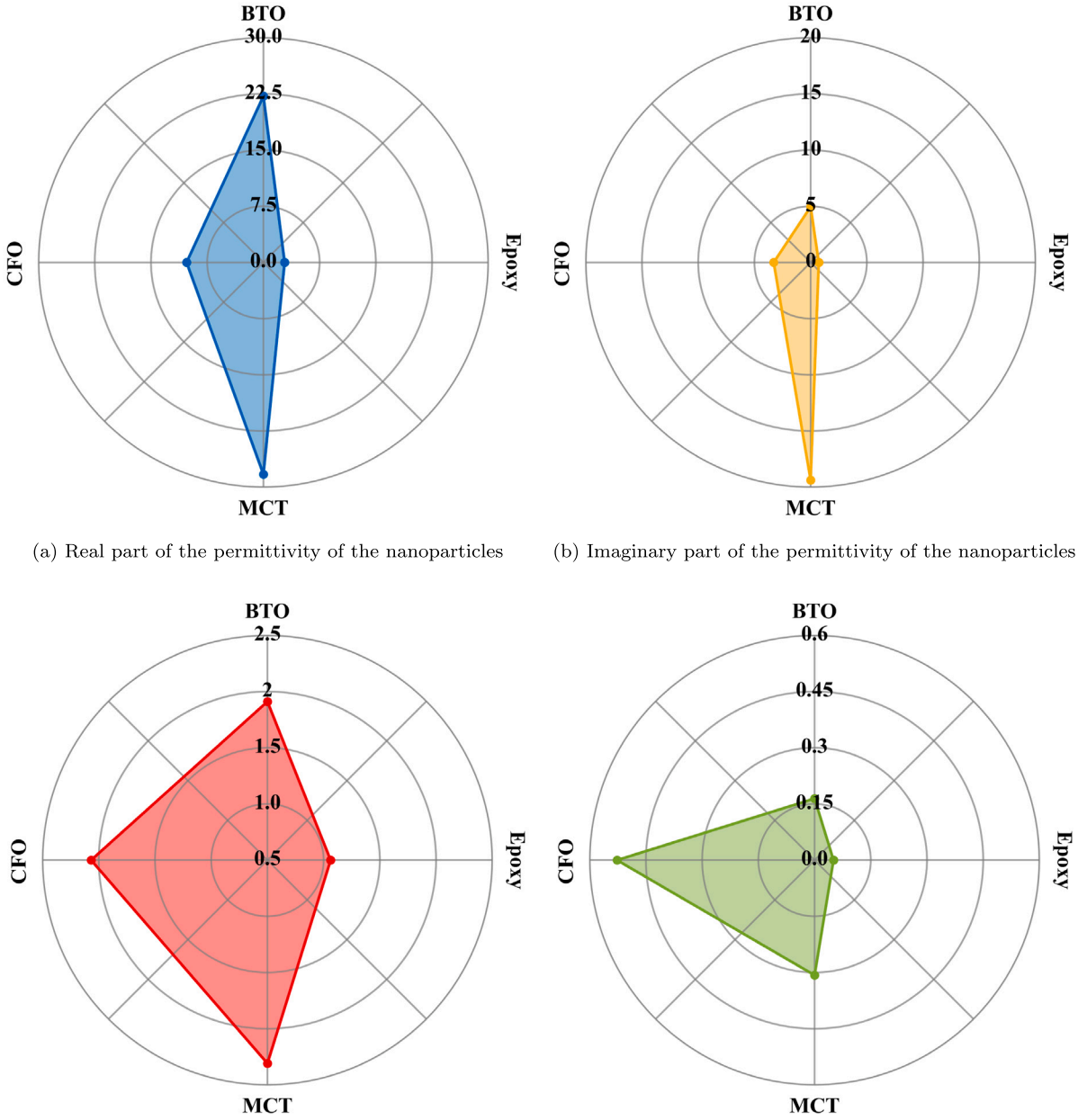

(a) Real part of the permittivity of the nanoparticles

(b) Imaginary part of the permittivity of the nanoparticles

(c) Real part of the permeability of the nanoparticles

(d) Imaginary part of the permeability of the nanoparticles

Fig. 9. Extracted electromagnetic properties of Epoxy, $BaTiO_3$, $CoFe_2O_4$ and Multi-walled CNT particles in the X-band frequency range using the optimisation tool.

It can also be seen that the BTO nanoparticle's electrical permittivities (ϵ', ϵ^{ε}) are greater than CFO nanoparticles. The magnetic permeabilities (μ', μ^{ε}) of CFO nanoparticles are greater than BTO nanoparticles. Using these extracted nanoparticle properties, the interaction parameter K is obtained for the multiphase composite with BTO, CFO and MCT particles using the Mixed45 composite sample's electromagnetic properties. K for the ϵ and μ of the multiphase composite is 0.762 and 4.752, respectively.

Using the interaction parameters (K's), epoxy properties and individual nanoparticle properties, the effective properties of BTO, CFO, MCT and Mixed composite samples with 20% volume fractions are obtained. These effective properties are compared with the extracted properties obtained from the experiments performed using two-port VNA. The properties obtained from the in-house tool parameters are plotted in violet, and the experimental results are plotted in yellow. It can be seen from Fig. 10 that the difference between properties obtained using the optimisation tool with the experimental results is less than 3% to 6%. The close agreement between the optimisation tool's predictions and experimental results (within 3%–6% deviation) demonstrates the reliability of the proposed methodology. Composite samples with 10%, 15%, 25% and 30% have also been tested, the effective EM properties from the optimisation tool have been obtained and validated with the experimentally obtained EM properties (refer Figs. A9, A10, A11). The table summarising the effective EM properties of two-phase and multiphase nanocomposites obtained from the experiments and the optimisation tool is shown in Table 4. The error percentages in Table 4 demonstrate that the optimisation tool predictions are within 6% of the experimental values for both permittivity

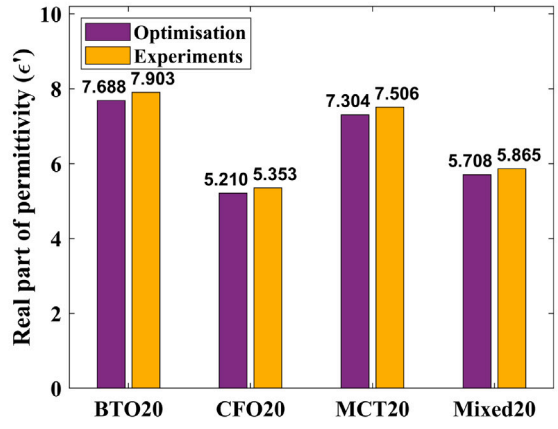

(a) Real part of the permittivity of the nanocomposites with 20% volume fraction

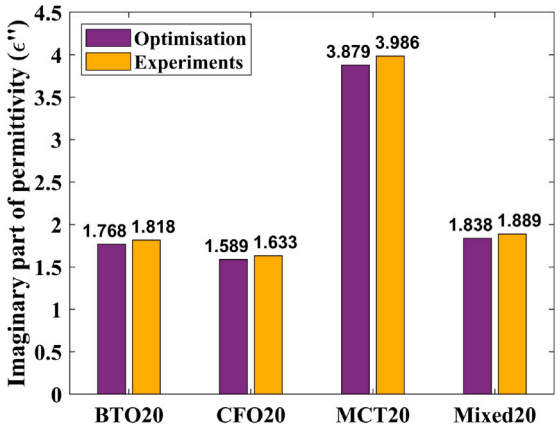

(b) Imaginary part of the permittivity of the nanocomposites with 20% volume fraction

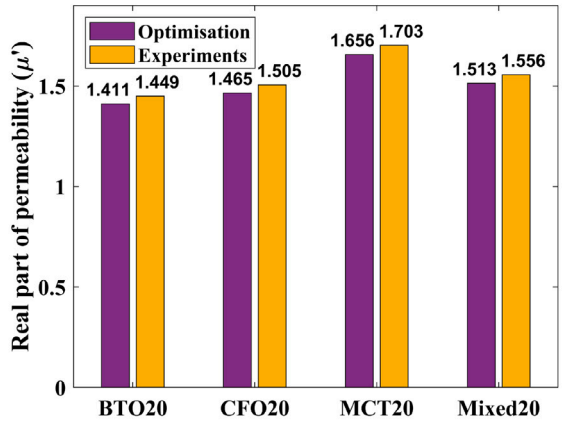

(c) Real part of the permeability of the nanocomposites with 20% volume fraction

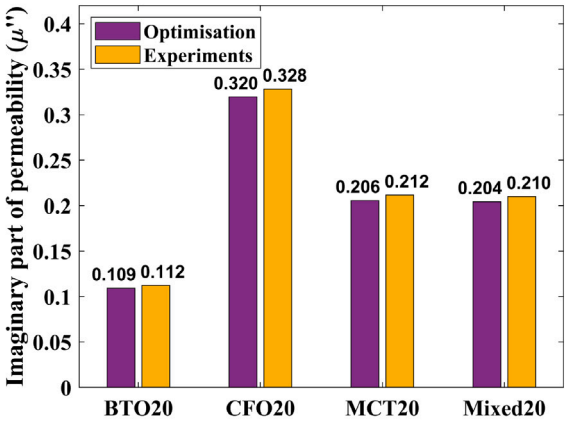

(d) Imaginary part of the permeability of the nanocomposites with 20% volume fraction

Fig. 10. Comparison of the electromagnetic properties of the nanocomposites with 20% volume fraction obtained from experiments (in yellow) and optimisation (in violet). Where Mixed20 contains 10% $BaTiO_3$, 5% $CoFe_2O_4$ and 5% MWCNTs nanoparticles inside epoxy.

and permeability across all samples, indicating strong agreement and supporting the applicability of the Lichtenecker mixing rule in these nanocomposites. The consistency in the prediction of the EM properties is attributed to the hybrid Nelder–Mead and L-BFGS approach, which effectively navigates the complex, non-convex optimisation landscape (Section 4.1). Similarly, the TMM tool's RL spectra (refer Fig. 11) align closely with experimental measurements, with deviations below 5%, confirming its robustness for predicting broadband reflection loss across various volume fractions and thicknesses. These results suggest that the proposed methodology is repeatable and stable, even with minimal experimental inputs, unlike data-intensive approaches such as machine learning-based property prediction.

The extracted properties obtained from the optimisation tool are given as input to the in-house TMM tool, along with the volume fraction and thickness of the respective samples, to evaluate the reflection loss (RL) in the X-band frequency range. The RL spectrum obtained from the TMM tool in the X-band frequency range is compared with the RL obtained using the S_{11} values obtained from two-port VNA (refer Fig. 11). The close agreement between the TMM evaluations and experimental RL spectra highlights the tool's capability to accurately model the electromagnetic behaviour of both two-phase and multiphase composites across a wide frequency range. For instance, the RL plots for the Mixed10 sample (containing 3% BTO, 4% CFO, and 3% MCT) exhibit a minimum RL of approximately −13 dB around 10 GHz, with the TMM predictions following the same trend as the experimental data. Similarly, for higher volume fractions such as Mixed30 (10% BTO, 10% CFO, and 10% MCT), the RL spectra show a consistent match, with deviations remaining minimal even as the material complexity increases. This consistency across different volume fractions and material combinations underscores the robustness of the TMM tool, making it a reliable method for predicting microwave absorption properties without requiring extensive experimental datasets. Although the TMM approach is computationally efficient for this study, future work could explore numerical methods (e.g., FEM or FDFD) to explicitly model non-uniform structures, offering deeper insights into localised effects. However, since this study

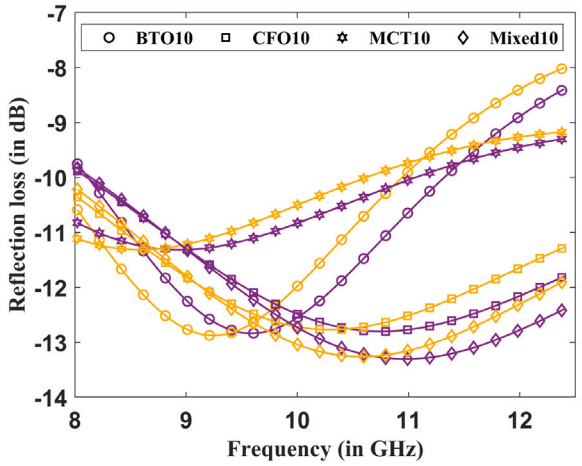

(a) Reflection loss plots comparison of two-phase and multiphase nanocomposites. Where, Mixed10 contains 3% $BaTiO_3$, 4% $CoFe_2O_4$ and 3% MWCNTs nanoparticles inside epoxy.

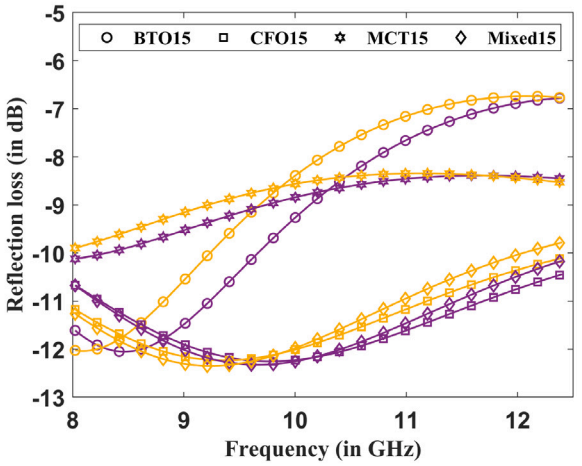

(b) Reflection loss plots comparison of two-phase and multiphase nanocomposites. Where, Mixed15 contains 5% $BaTiO_3$, 5% $CoFe_2O_4$ and 5% MWCNTs nanoparticles inside epoxy.

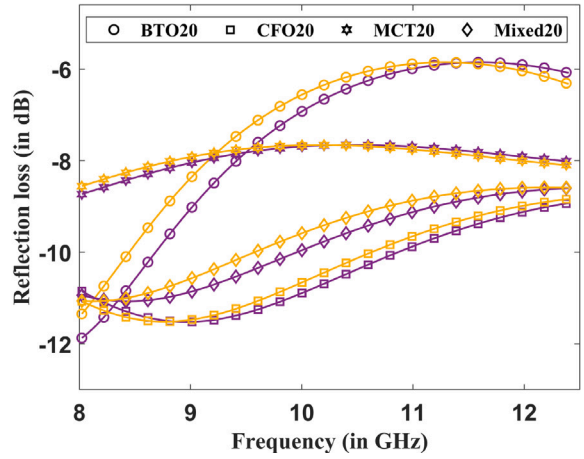

(c) Reflection loss plots comparison of two-phase and multiphase nanocomposites. Where, Mixed20 contains 10% $BaTiO_3$, 5% $CoFe_2O_4$ and 5% MWCNTs nanoparticles inside epoxy.

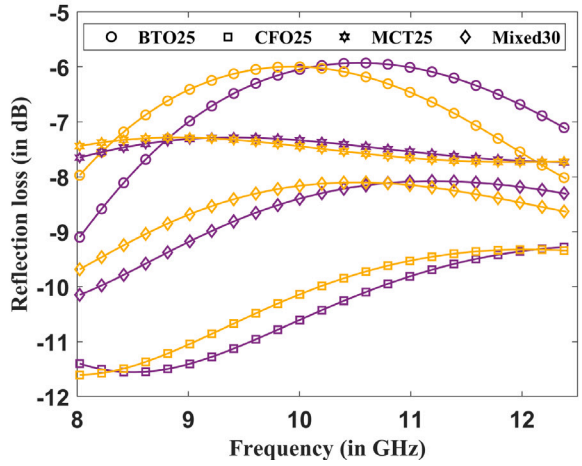

(d) Reflection loss plots comparison of two-phase and multiphase nanocomposites. Where, Mixed30 contains 10% $BaTiO_3$, 10% $CoFe_2O_4$ and 10% MWCNTs nanoparticles inside epoxy.

Fig. 11. Reflection loss comparison plots obtained from the in-house TMM tool (in violet) and the experiments (in yellow) for validating the in-house tool.

focuses on global EM responses (e.g., absorption/reflection), the uniformity assumption, compensated by the interaction parameters, does not compromise the results. For analyses requiring local field distributions (e.g., electric/magnetic field variations), micro-CT-based particle distribution data would be essential.

Compared to traditional trial-and-error methods [11], which suffer from high variability due to extensive experimental iterations, our methodology leverages minimal experimental data (e.g., two volume fractions per nanoparticle) to achieve consistent results. Similarly, while genetic algorithms [32] can optimise composite compositions, they often require numerous iterations, increasing computational variability. The proposed hybrid optimisation and TMM tools offer a reliable alternative, as evidenced by their validated performance across BTO, CFO, and MCT composites.

5.3. Transfer matrix method (TMM) results

This section analyses the multiphase composite's reflection loss (RL) capabilities with different combinations of volume fractions. The effective properties of the composites play a crucial role in determining the absorption characteristics. From the extracted properties of the individual nanoparticles and the interaction parameters (K) obtained from the experimental studies, design contours are plotted by varying the individual nanoparticle's volume fraction between 0 & 1, and the remaining volume fraction is of epoxy matrix. The design contours can be seen in Fig. 12. ϵ', ϵ^{ε}, μ' and μ^{ε} is varied from 2.87 & 28.04, 0.74 & 19.17, 1.07 & 2.30, and 0.06 & 0.52 respectively for different combinations of the volume fractions. Permittivity is more dominant for MCT nanoparticles, and higher effective permittivities (real and imaginary) are observed at higher volume fractions of MCT (refer to Figs. 12(a) and 12(b)). Whereas the μ' is almost in a similar range for all the nanoparticles, there for the triangular variation can be seen (refer to Fig. 12(c)). The μ^{ε} is more for CFO than MCT or BTO; therefore, the imaginary part of the magnetic permeability is more when the volume fraction of the CFO nanoparticles is more (refer to Fig. 12(d)). These effective properties are given as the input, along with other features like thickness, incidence angle and polarisation (TE or TM), to the in-house TMM tool described in Section 4.2.

5.3.1. Influence of nanoparticles and thickness

A parametric study was carried out to identify the influence of nanoparticles and the multiphase nanocomposites' thickness. The main

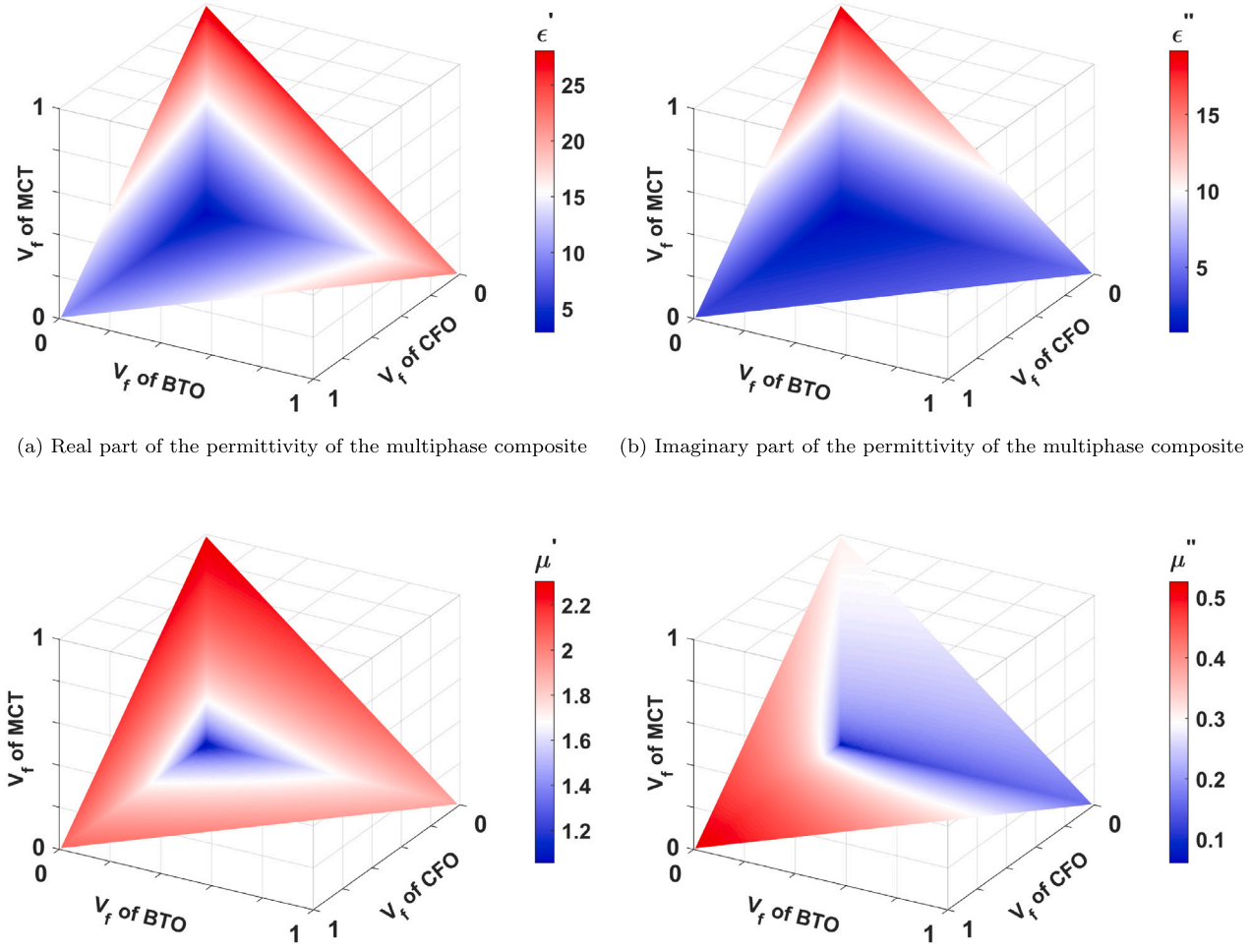

(a) Real part of the permittivity of the multiphase composite

(b) Imaginary part of the permittivity of the multiphase composite

(c) Real part of the permeability of the multiphase composite

(d) Imaginary part of the permeability of the multiphase composite

Fig. 12. Effective electromagnetic properties of the multiphase composite with different volume fraction combinations in the X-band frequency range.

objective is to ensure broadband reflection loss across the frequency range, i.e. bandwidth of 4.4 GHz (RL < −10 dB). The thickness of the sample is increased to 10 mm, starting from 1 mm, and the other parameters like V_f of BTO, CFO and MCT nanoparticles are varied from 1% to 20%. It has been identified that attaining a bandwidth of 4.4 GHz has become impossible at higher volume fractions of nanoparticles because of the deviation in the impedance of the composite from the free space impedance. Even fabricating composite samples at this higher loading is also difficult; therefore, the upper limit is fixed at 20%. To evaluate the influence of individual nanoparticles inside the multiphase composite, the reflection loss contours are obtained by increasing the volume fraction from 5% to 20% and keeping other nanoparticle volume fractions at 1%.

Fig. 13 shows the influence of BTO nanoparticle loading on the RL in the X-band frequency range. From Fig. 13(a) (V_f of BTO is 5% and others at 1%), it can be identified that the minimum RL of −15.1 dB is obtained while varying the thickness from 1 mm to 10 mm. It can be seen from Fig. 13(a) that between 2 mm and 5 mm, the RL is always greater than −10 dB. Two different thickness configurations (1 mm and 7 mm) have shown broadband RL covering the entire X-band frequency range when the BTO loading is 5%. However, the minimum RL for a 1 mm thickness sample is −13.65 dB (obtained at 8.00 GHz). The RL of −15.1 dB is obtained for a 7 mm thickness sample at 9.78 GHz. When the BTO loading increased to 10% (refer Fig. 13(b)) while keeping the other inclusions at 1%, only for thicknesses of 6.1 mm and 6.2 mm, the RL < −10 dB in the frequency range. With further increments in the BTO loading to 15% and 20% (refer Figs. 13(c) and 13(d)), not even at a single thickness configuration, a complete bandwidth of 4.4 GHz is obtained. This supports the argument that at higher loading contents of BTO, the EM wave reflection will be higher. Therefore, it is identified that BTO loading below 10% will result in broadband reflection loss.

The influence of CFO loading can be seen in Fig. 14, the plots from Fig. 14(a) to Fig. 14(d) show how RL contour is varying with increment in V_f of CFO from 5% to 20% along with the thickness of the nanocomposite. It is observed that when the CFO loading is 5%, the minimum RL is −14.8 dB in the X-band frequency range at certain thickness configurations. For a 1 mm thickness composite sample, the minimum RL of −14.8 dB has been attained. The broadband RL has been attained between the thickness range of 7 mm to 10 mm. When the CFO loading is increased to 10%, the minimum RL of −14.38 dB is obtained for 1 mm thickness and the complete bandwidth of 4.4 GHz between 6 mm to 10 mm along with a 1 mm thick sample. For 15% and 20% CFO loading, the minimum RL is −13.8 dB and −13.10 dB, respectively, obtained for 1 mm thick samples. Even at higher loadings of CFO, i.e., 15% and 20%, the broadband RL covering the entire X-band frequency range is obtained for a thickness range of 6 mm to 10 mm and 5 mm to 10 mm, respectively, along with 1 mm thick samples. From these RL plots of CFO-dominated nanocomposites, it can be observed that CFO loading provides broadband bandwidth even when a high volume fraction of CFO nanoparticles is loaded, and there

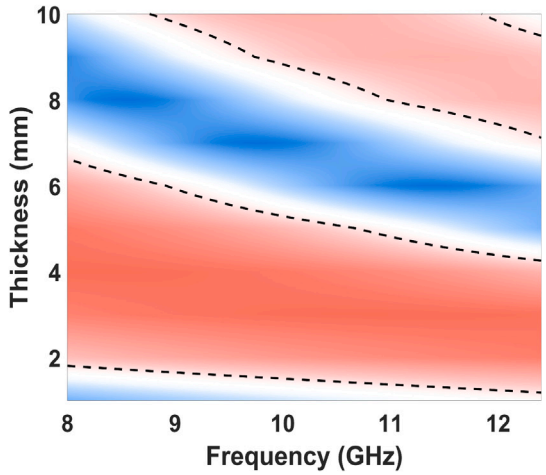

(a) RL contour of $BaTiO_3$ dominant loaded composite with V_f of $BaTiO_3$ = 05%

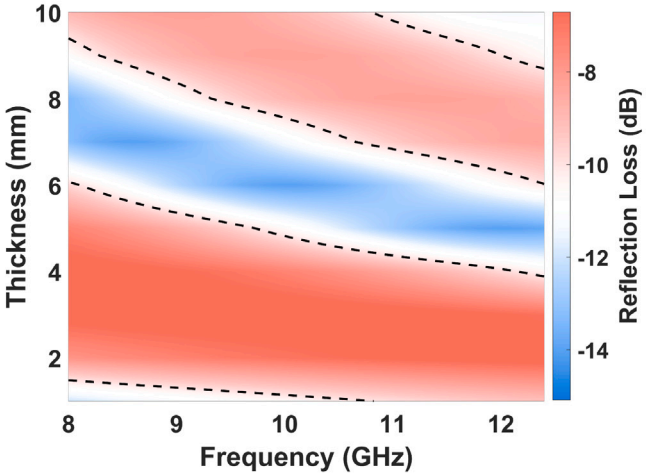

(b) RL contour of $BaTiO_3$ dominant loaded composite with V_f of $BaTiO_3$ = 10%

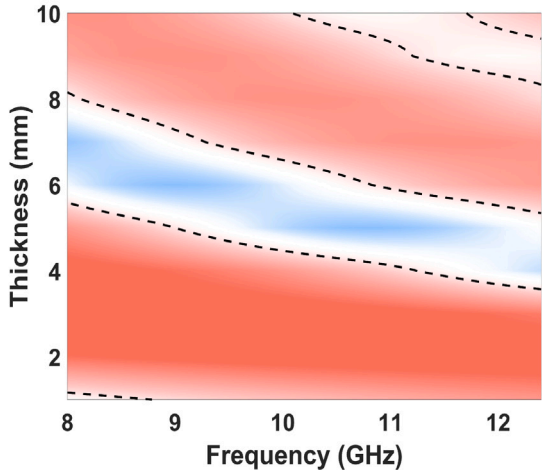

(c) RL contour of $BaTiO_3$ dominant loaded composite with V_f of $BaTiO_3$ = 15%

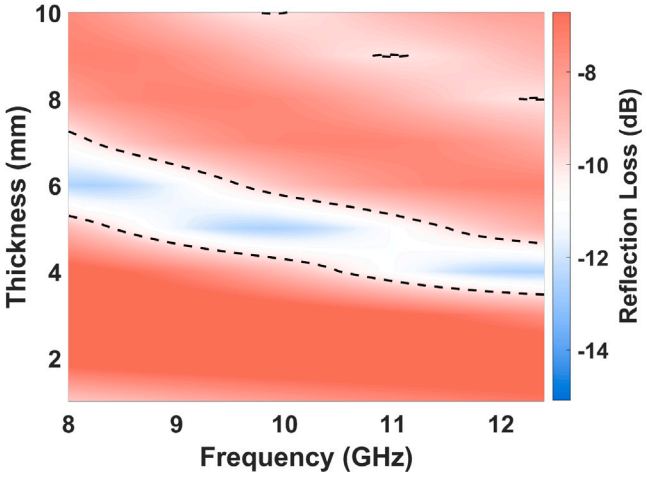

(d) RL contour of $BaTiO_3$ dominant loaded composite with V_f of $BaTiO_3$ = 20%

Fig. 13. Reflection loss contours of $BaTiO_3$-dominant multiphase composites with CFO and MCT nanoparticles at 1% volume fraction.

is a large range of thickness configurations where this bandwidth of 4.4 GHz is possible.

In a composite material, increasing BTO content leads to higher reflection rather than absorption. The high permittivity increases the composite's impedance mismatch with free space, causing more incident EM waves to reflect off the surface rather than penetrate the material and be absorbed. As a result, increasing BTO content often raises the reflection level, limiting the material's effectiveness for broadband absorption. In contrast, increasing CFO content does not lead to the same increase in reflection. CFO is a ferromagnetic material which introduces magnetic loss mechanisms such as ferromagnetic resonance and eddy current losses. The less electrical permittivity compared to BTO and higher magnetic permeability at higher loading of CFO enable better impedance matching with free space, allowing EM waves to enter the material more effectively rather than being reflected. Thus, even at higher loadings, CFO maintains lower reflection levels and enhances broadband absorption compared to BTO.

In the next step, MCT loading influence (refer Fig. 15) is evaluated by varying the thickness and the V_f of MCT. From Fig. 15(a), it can be seen that RL below −10 dB is attained for 6 mm to 7 mm thick composite samples. Meanwhile, the minimum RL of −13.40 dB is obtained for the 1 mm thick sample. When the loading is increased to 10%, the minimum RL is −11.70 dB, and broadband RL covers the entire X-band frequency range for a 5.5 mm thick sample. However, broadband RL is not obtained with further increments in MCT loading. As the MCT content increases, the composite's overall conductivity rises. High conductivity typically leads to reflection because conductive materials create a barrier to EM wave penetration, effectively acting like a mirror to incident waves. This high conductivity reduces the penetration depth, limiting the ability of the EM wave to enter the material where it could otherwise be absorbed. At lower MCT loadings, dielectric loss mechanisms (such as polarisation relaxation) play a larger role in absorbing EM waves. However, at higher loadings, the dominant conductive nature of the material overshadows these dielectric loss mechanisms, decreasing the material's ability to absorb and dissipate EM energy as heat.

Impedance of the nanocomposite placed between free space is obtained using Eq. (15) [33] to quantitatively compare the impedance with the change in the nanoparticles loading. $|Z_s|/\eta_0$ versus frequency and volume fraction plots have been plotted to illustrate the mismatching conditions for higher loadings of BTO and MCT. The impedance plots for 5 mm and 8 mm thick samples are presented in Fig. 16, and the following analysis elucidates the contributions of each nanoparticle type to impedance matching across the X-band frequency range

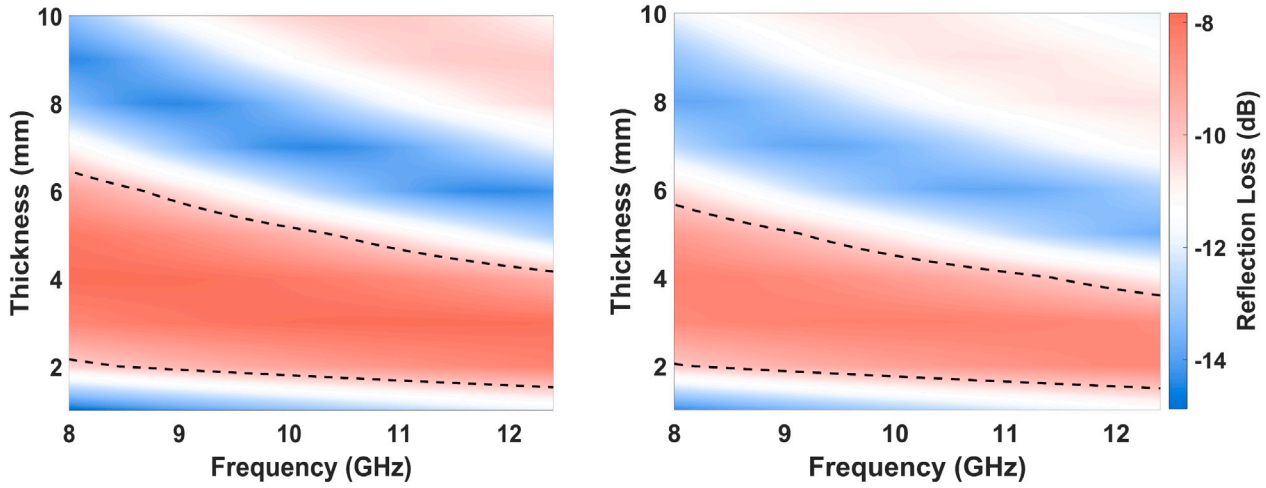

(a) RL contour of $CoFe_2O_4$ dominant loaded composite with V_f of $CoFe_2O_4$ = 05%

(b) RL contour of $CoFe_2O_4$ dominant loaded composite with V_f of $CoFe_2O_4$ = 10%

(c) RL contour of $CoFe_2O_4$ dominant loaded composite with V_f of $CoFe_2O_4$ = 15%

(d) RL contour of $CoFe_2O_4$ dominant loaded composite with V_f of $CoFe_2O_4$ = 20%

Fig. 14. Reflection loss contours of $CoFe_2O_4$-dominant multiphase composites with BTO and MCT nanoparticles at 1% volume fraction.

(8–12.4 GHz). The normalised impedance of a material is a critical parameter for assessing impedance matching, where Z_s is the input impedance of the sample, and η_0 is the impedance of free space (approximately 377 ohms). For optimal impedance matching, $|Z_s|/\eta_0$ should be close to 1, ensuring minimal reflection of electromagnetic waves at the air-material interface. The differences in these electromagnetic properties across BTO, CFO, and MCT samples directly influence the impedance mismatch observed at various volume fractions.

For the BTO samples, as shown in Figs. 16(a) and 16(b), the $|Z_s|/\eta_0$ values range from approximately 0.48 to 0.75 across the frequency range for both 5 mm and 8 mm thick samples. At higher BTO volume fractions (e.g., 10%–20%), the $|Z_s|/\eta_0$ decreases to below 0.6, indicating a greater deviation from the ideal value of 1. This impedance mismatch is primarily driven by the high permittivity of BTO, while the permeability remains relatively low. The imbalance between effective electromagnetic properties results in a lower $|Z_s|/\eta_0$, leading to increased reflection and poor impedance matching. The impedance mismatch (normalised impedance < 0.6) can be observed even at lower volume fractions in the 8 mm thick sample compared to the 5 mm thick sample. With some minor variations, this phenomenon is even similar in the case of MCT samples as well, which can be observed from Figs. 16(e) and 16(f).

$$Z_s = \eta_0 \frac{\eta_c + j\eta_0 \tan(\beta d)}{\eta_0 + j\eta_c \tan(\beta d)} \tag{15}$$

Where, $\eta_c = \eta_0\sqrt{\frac{\mu_r}{\epsilon_r}}$ is the intrinsic impedance of the composite material, $\eta_0 = \sqrt{\frac{\mu_0}{\epsilon_0}} \approx 376.73\ \Omega$ is the free-space impedance, $\gamma = j\frac{\omega}{c}\sqrt{\mu_r\epsilon_r} = j\beta$ is the propagation constant in the material, d is the slab thickness, ω is the angular frequency, $c = \frac{1}{\sqrt{\mu_0\epsilon_0}}$ is the speed of light, ϵ_r and μ_r are the relative permittivity and permeability of the composite, respectively.

In contrast, the CFO samples exhibit comparatively better impedance matching compared to BTO & MCT samples, as seen in Figs. 16(c) and 16(d), with $|Z_s|/\eta_0$ values ranging from 0.58 to 0.73 for both thicknesses. Even at higher volume fractions (e.g., 10%–20%), the $|Z_s|/\eta_0$ remains closer to 0.6. This phenomenon strengthens the argument that highly loaded CFO composite samples competitively minimise the impedance mismatch, making CFO-based composites more suitable for microwave absorption applications. The similarity in $|Z_s|/\eta_0$ trends between 5 mm and 8 mm thick CFO samples suggests that thickness has a less significant impact on impedance matching for CFO dominant composite samples.

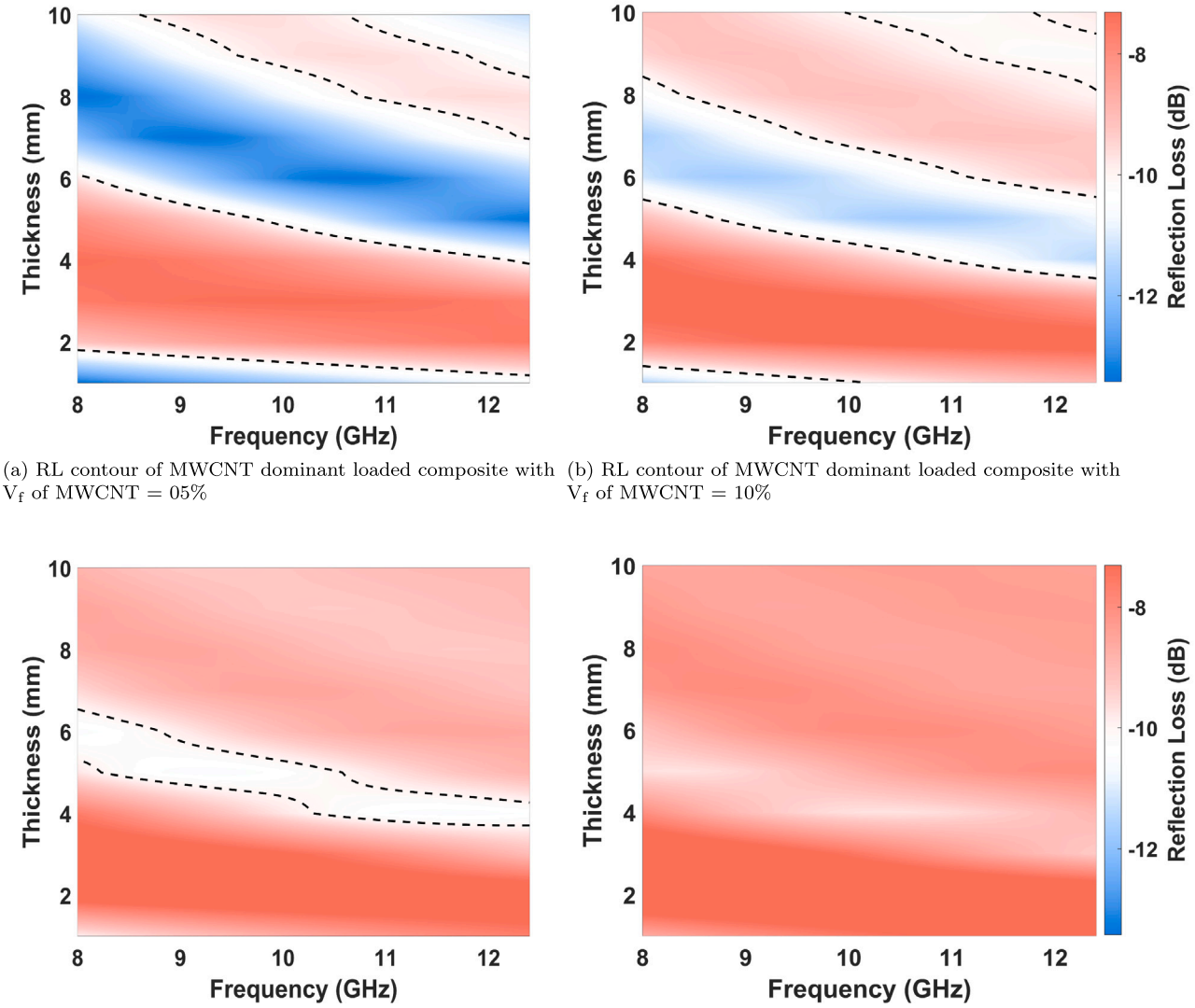

(a) RL contour of MWCNT dominant loaded composite with V_f of MWCNT = 05%

(b) RL contour of MWCNT dominant loaded composite with V_f of MWCNT = 10%

(c) RL contour of MWCNT dominant loaded composite with V_f of MWCNT = 15%

(d) RL contour of MWCNT dominant loaded composite with V_f of MWCNT = 20%

Fig. 15. Reflection loss contours of MWCNT-dominant multiphase composites with BTO and CFO nanoparticles at 1% volume fraction.

From these parametric studies, it can be seen that the broadband RL in the X-band frequency range can be attained for multiple combinations of volume fractions of nanoparticles and the thickness of the nanocomposite samples. Based on the application's requirements, the composite's configuration can be finalised using these experimentally validated in-house computational tools. In case a selective frequency range reflection loss is required, we can tailor the composition using these tools; similarly, if the objective is to reduce the transmission and increase the reflection in the frequency band, that can also be attained. On the other hand, if the goal is to use this nanocomposite mixture for the coating, then lower thickness samples can be given preference, whereas if the idea is to use these composites as a load-bearing component along with RL, then higher thickness configurations can be explored. Therefore, narrowing down a single configuration for broadband reflection loss is application-oriented.

5.3.2. *Influence of incidence angle and polarisation*

In this section, two different volume fraction combinations were chosen based on the inferences drawn from the previous section to evaluate the influence of the incident angle and the polarisation (TE and TM) on the multiphase composite with specific thickness, i.e., less volume fraction of BTO and MCT nanoparticles and more volume fraction of CFO nanoparticles. The thickness of the considered nanocomposite samples is 1 mm and 7 mm. These thicknesses are chosen to show the difference between the incident angle influence at lower and higher thicknesses. The incident angle is increased till 80° along with varying the polarisation.

Fig. 17 shows the RL contours of the multiphase composite sample with volume fractions of BTO, CFO and MCT as 2%, 4% and 2% respectively. The minimum RL is −14.10 dB in the X-band frequency range under the normal incidence (refer to Fig. 17(a)). Till the angle of incidence is 30°, the broadband RL is observed under the incidence of TE polarised waves. However, with the increment in the thickness of the composite with the same volume fraction combination, the bandwidth covering the entire X-band frequency range is attained only till the angle of incidence is 25° with a minimum RL of −13.98 dB which is very close to the minimum RL obtained for 1 mm thick sample. However, it can be seen above 50° and 40° that the RL is greater than −10 dB for 1 mm and 7 mm thick samples, respectively, which is not desirable. Unlike in the TE polarisation, upon incidence of TM polarised EM waves, broadband RL is attained till a very high incident

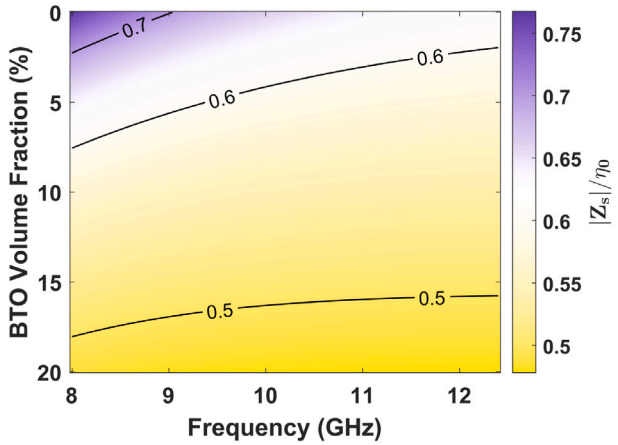

(a) Impedance ($|Z_s|/\eta_0$) as a function of frequency and BTO volume fraction for 5 mm thick samples.

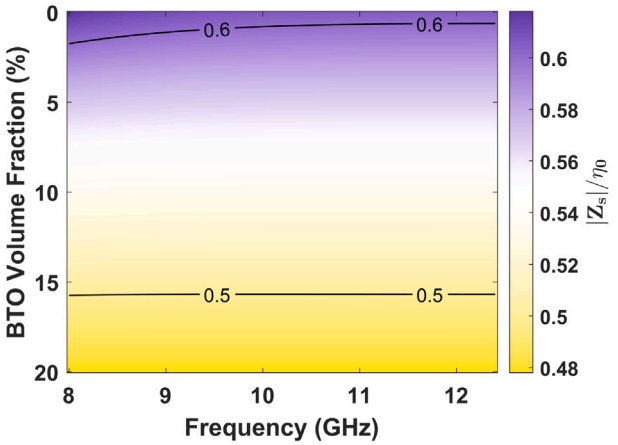

(b) Impedance ($|Z_s|/\eta_0$) as a function of frequency and BTO volume fraction for 8 mm thick samples.

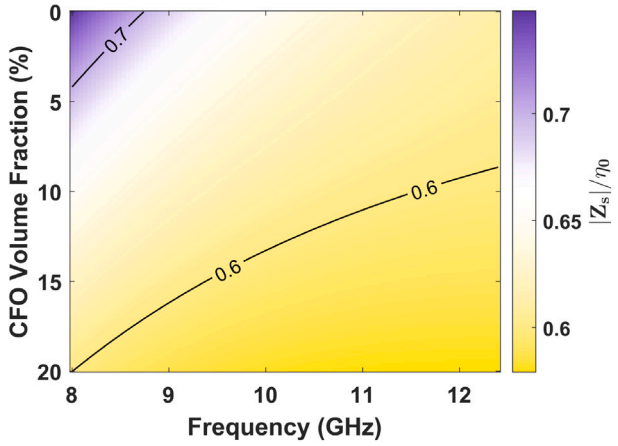

(c) Impedance ($|Z_s|/\eta_0$) as a function of frequency and CFO volume fraction for 5 mm thick samples.

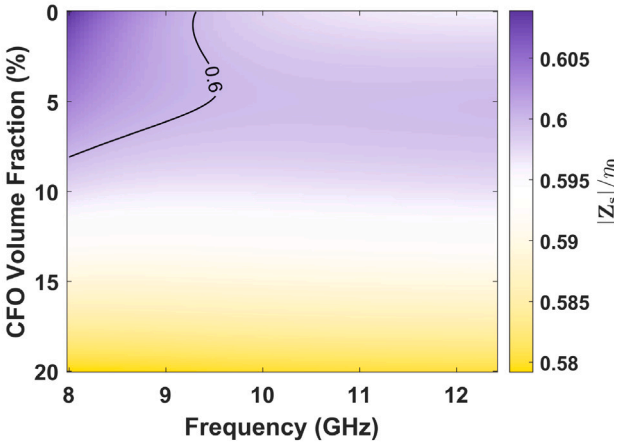

(d) Impedance ($|Z_s|/\eta_0$) as a function of frequency and CFO volume fraction for 8 mm thick samples.

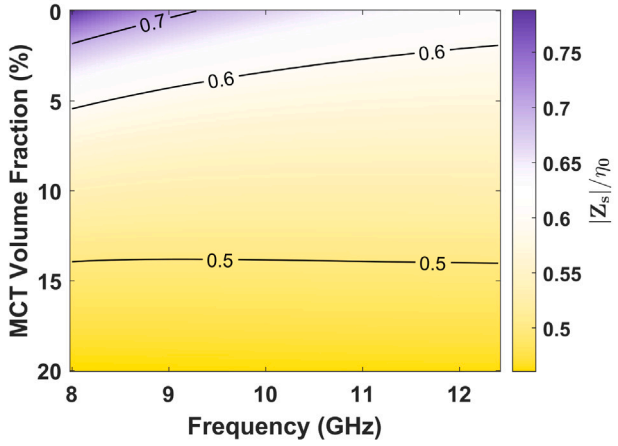

(e) Impedance ($|Z_s|/\eta_0$) as a function of frequency and MCT volume fraction for 5 mm thick samples.

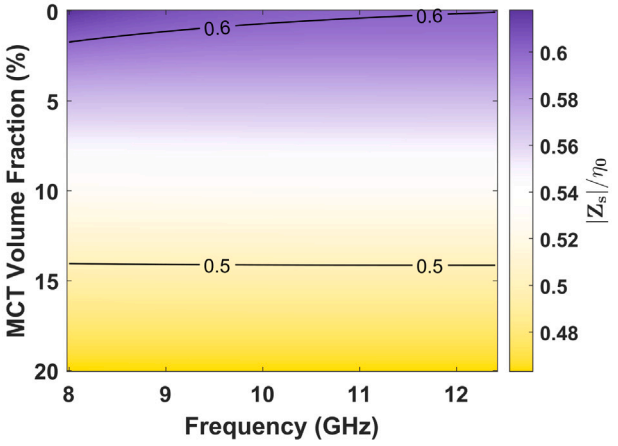

(f) Impedance ($|Z_s|/\eta_0$) as a function of frequency and MCT volume fraction for 8 mm thick samples.

Fig. 16. Impedance ($|Z_s|/\eta_0$) plots as a function of frequency (8–12 GHz) and volume fraction for BTO, CFO, and MCT nanoparticles in 5 mm and 8 mm thick samples, highlighting the contributions to impedance matching. While volume fraction of one of the nanoparticles is being varied till 20%, other nanoparticles are fixed at 1% volume fraction.

Table 2
Remaining mass percentages after thermal degradation for individual phases, composites, and mixed samples at various required volume fractions of $BaTiO_3$ (BTO), $CoFe_2O_4$ (CFO), and MWCNTs (MCT) based nanocomposites.

Phase	Remaining mass (in %)
Epoxy	06.650
BTO	90.515
CFO	84.824
MCT	98.549

(a) Remaining mass percentages for individual phases after thermal degradation, showing the thermal stability of epoxy, $BaTiO_3$ (BTO), $CoFe_2O_4$ (CFO), and MWCNTs (MCT).

Required V_f	Remaining mass (in %)		
	BTO	CFO	MCT
05%	23.130	22.453	06.986
10%	38.148	33.675	07.414
15%	47.225	41.161	07.783
20%	55.220	49.216	08.353
25%	60.088	54.067	08.889
30%	65.500	58.912	–
40%	–	–	11.024

(b) Remaining mass percentages for $BaTiO_3$ (BTO), $CoFe_2O_4$ (CFO), and MWCNTs (MCT) based nanocomposites at various required volume fractions.

Required V_f	Remaining mass (in %)
	Mixed sample
10%	16.929
15%	22.601
20%	27.56
30%	41.917
45%	57.231

(c) Remaining mass percentages of the mixed composite samples at various required volume fractions.

Table 3
Comparison of required and actual volume fractions for $BaTiO_3$ (BTO), $CoFe_2O_4$ (CFO), MWCNTs (MCT), and mixed composite samples, highlighting the discrepancies between theoretical and measured values.

Required V_f	Actual V_f (in %)			
	BTO	CFO	MCT	Mixed sample
05%	04.403	04.954	04.535	–
10%	09.740	09.803	09.787	09.935
15%	14.395	13.985	13.909	14.441
20%	19.799	19.737	19.640	19.353
25%	23.959	24.078	24.437	–
30%	29.679	29.324	–	28.968
40%	–	–	39.286	–
45%	–	–	–	41.112

angle (refer to Figs. 17(c) and 17(d)). The RL<−10 dB, covering the entire frequency range till the angle of incidence of 77° and 75° for 1 mm and 7 mm thick samples, respectively. When the inclusion volume fraction is doubled inside the epoxy matrix, the broadband RL is attained only upon the incidence of TM polarised waves till 77° incidence angle (refer to Figs. 18(c) and 18(d)). Nevertheless, under the influence of TE polarised waves, the desirable RL<−10 dB is attained only till 38° (refer to Figs. 18(a) and 18(b)) for both the 1 mm and 7 mm thick samples, covering only a part of the frequency range considered. These studies show that the combination of the proposed inclusion provides exceptional RL under the incidence of TM polarised waves than the TE polarised waves. Meanwhile, broadband RL can be attained at lower volume fractions in both TE and TM polarisations. The angle of incidence sensitivity of the composite samples is significant with variations in the volume fraction combinations rather than the thickness of the samples.

The electromagnetic absorption behaviour of the multiphase composite exhibits complex, polarisation-dependent characteristics influenced by permittivity, permeability, boundary conditions, and internal reflections. Under TE polarisation, the composite achieves broadband reflection loss (RL) up to 40°, but the RL bandwidth diminishes and drops to zero above 50°. In TE polarisation, the electric field lies parallel to the interfaces, while the magnetic field develops an increasing normal component as the incidence angle increases. However, the similar and relatively low magnetic permeabilities across BTO, CFO, and MCT limit magnetic field amplification at the interfaces, reducing the potential for strong magnetic loss interactions. Moreover, the parallel electric field orientation minimises charge accumulation, thereby reducing the chances of dipole reorientation and defect-induced polarisation, restricting dielectric loss contributions. Studies on FeSiB@C@$NiBr_2$ composites demonstrate that interface polarisation, driven by charge accumulation at C-$NiBr_2$ heterojunctions, significantly enhances dielectric loss, but requires a perpendicular electric field to maximise charge separation [34]. Similarly, FeCo/Zn@C nanofibres show that interface polarisation at FeCo/C interfaces boosts dielectric losses, yet is less effective in TE polarisation due to the parallel field [35]. Metal borides/carbon nanocomposites further confirm that interface polarisation at NiCoB-carbon boundaries enhances dielectric loss, but its efficacy diminishes without a normal electric field [36]. Additionally, single metal site carbon composites highlight that dipole polarisation, driven by dipole reorientation under an electromagnetic field, is critical for absorption, but is limited in TE polarisation due to reduced dipole alignment [37]. Defect-rich carbon nanosheets show that defect dipole polarisation, induced by oxygen vacancies, enhances dielectric loss through multiple Debye relaxation processes, but requires field alignment perpendicular to interfaces [38]. In TE polarisation, the lack of significant interface, dipole, and defect dipole polarisation at multiphase interfaces limits polarisation-relaxation processes at higher angles, thereby reducing EM energy dissipation. At lower angles, the composite's moderate permittivity and permeability values, along with relatively balanced impedance matching, allow the electric field to dissipate energy through dielectric losses, resulting in reasonable absorption. However, as the incidence angle increases, the shifting electric field path length and lack of magnetic field enhancement disrupt impedance matching, reducing RL bandwidth.

At lower angles in TM polarisation, the multiphase composite's electromagnetic properties and relatively balanced impedance matching allow the magnetic field to interact initially and dissipate energy through magnetic losses, resulting in reasonable absorption. Unlike TE polarisation, in TM polarisation, the electric field develops normal components as the incidence angle increases, enhancing permittivity differences between BTO, CFO, MCT, and epoxy, leading to strong field interactions. This contrast in permittivity, especially with MCT's high imaginary permittivity, creates favourable conditions for electric field interactions at these interfaces. This field interaction enhances energy dissipation as more electromagnetic energy is converted into heat. This is further enhanced by robust interface, dipole, and defect dipole polarisation mechanisms, supported by magnetic-electric balance and magnetoelectric coupling. For instance, FeSiB@C@$NiBr_2$ composites exhibit enhanced dielectric losses due to interface polarisation at C-$NiBr_2$ heterojunctions, with nanosheet arrays promoting charge accumulation and multiple Debye relaxation processes [34]. FeCo/Zn@C nanofibres similarly show that charge accumulation at FeCo/C interfaces boosts dielectric losses, amplified by the normal electric field in TM polarisation [35]. Metal borides/carbon nanocomposites highlight that interface polarisation at NiCoB-carbon boundaries, combined with magnetic losses from cobalt-based borides, optimises EM absorption

Table 4
Comparison of effective electromagnetic properties of $BaTiO_3$ (BTO), $CoFe_2O_4$ (CFO), MWCNTs (MCT), and mixed composite samples, highlighting the difference between the in-house optimisation tool and experimental values.

Sample	Permittivity (ϵ)		Error %	Permeability (μ)		Error %
	Experiments	Optimisation tool		Experiments	Optimisation tool	
BTO10	5.597+j1.318	5.420+j1.276	3.164	1.329+j0.095	1.277+j0.091	3.914
BTO15	6.897+j1.597	6.582+j1.528	4.555	1.409+j0.106	1.350+j0.101	4.190
BTO20	7.903+j1.818	7.688+j1.768	2.722	1.449+j0.112	1.411+j0.109	2.623
BTO25	9.210+j2.134	8.751+j2.000	5.049	1.564+j0.123	1.464+j0.116	5.890
CFO10	4.386+j1.288	4.188+j1.230	4.513	1.357+j0.251	1.302+j0.242	4.038
CFO15	4.939+j1.486	4.726+j1.420	4.323	1.452+j0.303	1.391+j0.286	4.260
CFO20	5.353+j1.633	5.210+j1.589	2.673	1.505+j0.328	1.465+j0.320	2.648
CFO25	5.970+j1.857	5.654+j1.742	5.372	1.634+j0.370	1.530+j0.346	5.871
MCT10	5.212+j2.326	5.004+j2.232	3.999	1.520+j0.175	1.459+j0.169	4.005
MCT15	6.484+j3.186	6.140+j3.041	5.158	1.637+j0.201	1.568+j0.190	4.234
MCT20	7.506+j3.986	7.304+j3.879	2.690	1.703+j0.212	1.656+j0.206	2.761
MCT25	8.972+j5.032	8.493+j4.740	5.450	1.828+j0.232	1.730+j0.218	5.372
Mixed10	4.270+j1.326	4.102+j1.278	3.907	1.395+j0.194	1.349+j0.187	3.303
Mixed15	5.125+j1.692	4.887+j1.640	4.488	1.516+j0.215	1.452+j0.205	4.230
Mixed20	5.865+j1.889	5.708+j1.838	2.679	1.556+j0.210	1.513+j0.204	2.765
Mixed30	7.627+j2.852	7.172+j2.694	5.913	1.766+j0.269	1.652+j0.252	5.752

through a magnetic-electric balance strategy [36]. Single metal site carbon composites demonstrate that dipole polarisation, driven by dipole reorientation, significantly boosts absorption, particularly when the electric field is normal to interfaces [37]. Defect-rich carbon nanosheets show that oxygen vacancies induce defect dipole polarisation, enhancing dielectric loss through multiple relaxation processes, further amplified in TM polarisation [38]. In the proposed multiphase composite, defects such as oxygen vacancies in BTO or CFO, combined with interfaces between BTO, CFO, MCT, and epoxy, facilitate charge accumulation, dipole reorientation, and defect dipole polarisation. The normal electric field in TM polarisation enhances these effects, promoting polarisation-relaxation processes. The ferroelectric BTO and ferrimagnetic CFO phases likely induce magnetoelectric coupling, where electric field-induced polarisation in BTO interacts with magnetic domains in CFO, enhancing synergistic dielectric and magnetic losses. This coupling, supported by the dielectric-magnetic synergy in $FeSiB@C@NiBr_2$ composites and the magnetic-electric balance in NiCoB/C composites, sustains effective energy dissipation at high angles. The heterogeneous interfaces promote multiple reflections, as seen in nanosheet array structures, further attenuating waves [34] . As a result, TM polarised EM wave absorption remains strong, even as the angle increases, sustaining broadband RL up to 78°. The peak in RL around 60° in TM polarisation results from an optimal balance between electric field amplification, dielectric losses, and magnetic field interactions, maximised by interface, dipole, and defect dipole polarisation, magnetic-electric balance, and magnetoelectric coupling. This multiscale synergy enables sustained broadband RL across a wide angular range and highlights the importance of tailored nanostructuring and phase selection in EM absorber design.

In the multiphase composite with 4%, 8%, and 4% volume fractions, broadband RL is not attained at lower incident angles in TE and TM polarisations due to impedance mismatch in certain X-band frequency regions. Increased loading enhances electric and magnetic losses, but impedance mismatch reduces the energy interacting with the particles, increasing reflection. This is consistent with findings in $FeSiB@C@NiBr_2$ composites, where excessive nanosheet loading increases interface polarisation but disrupts impedance matching [34]. FeCo/Zn@C nanofibres show that higher nanoparticle loading boosts interface polarisation, yet risks impedance mismatch [35]. Metal borides/carbon nanocomposites demonstrate that while interface polarisation and magnetic-electric balance enhance EM absorption, excessive loading can disrupt impedance matching [36]. Single metal site carbon composites indicate that excessive dipole polarisation may lead to impedance challenges [37]. Defect-rich carbon nanosheets show that excessive defect dipole polarisation increases conductivity, reducing impedance matching and RL performance [38].

5.4. Critical assessment of the proposed multiphase nanocomposite RL performance

A comprehensive comparison is provided in Table 5 to evaluate the electromagnetic absorption performance of the proposed multiphase nanocomposites against other recently reported systems in the X-band frequency range. The first two entries in the table correspond to the present study, which investigates $BaTiO_3/CoFe_2O_4$/MWCNTs dispersed in an epoxy matrix. These entries represent two sample compositions: (i) V_{BTO} = 2%, V_{CFO} = 4%, and V_{MCT} = 2%, and (ii) V_{BTO} = 4%, V_{CFO} = 8%, and V_{MCT} = 4%. These ceramic-based multiphase nanocomposites demonstrate considerable synergy between dielectric ($BaTiO_3$), magnetic ($CoFe_2O_4$), and conductive (MWCNTs) inclusions, resulting in efficient microwave attenuation. With a thickness of just 1 mm, the proposed configurations achieve reflection losses of −14.10 dB and −12.16 dB with effective bandwidths of 4.0 GHz and 3.36 GHz, respectively. These results correspond to high-efficiency values (i.e., RL per unit thickness) of approximately −14.1 dB/mm and −12.16 dB/mm, making them highly promising for thin, lightweight microwave absorption applications.

In contrast, many of the other literature-reported absorbers utilise either metallic alloys, oxide-decorated CNTs, or complex carbides embedded in matrices such as paraffin, carbon fibre, or MXene-derived composites. For instance, Guo et al. [39] synthesised $LaFeO_3$ nanoparticles, and magnetic $LaFeO_3$/Fe@CNTs nanocomposites were successfully prepared in situ by CVD method using the $LaFeO_3$ nanoparticles. Later, Fe nanoparticles are reduced from $LaFeO_3$ and encapsulated into CNTs. Although the optimal sample reported by Guo et al. achieved a minimum reflection loss of –38.76 dB, it required a thickness of 2.5 mm, resulting in a reduced efficiency of −15.50 dB/mm. In another research work, Guo et al. [40] fabricated multiphase structured Co/Ni bimetallic nitride fibre material ($Co_{5.47}N/Ni_4N$/CF) using a combination of electrospinning, hydrothermal synthesis, and high-temperature nitridation. The optimal multiphase nanocomposite has shown a minimum RL of –43.82 dB and a bandwidth of 4.0 GHz, but with a sample of 2.9 mm thickness, resulting in an RL/mm of –15.1 dB/mm. Although these values seem competitive, they rely heavily on magnetic metal nitrides or core–shell structures, which are often more difficult to synthesise with uniform dispersion and may compromise w.r.t mechanical or thermal stability.

Zhang et al. [41] fabricated a novel multiphase Fe/Co magnetic oxide that is facilely introduced onto the α-Fe particles. The incorporation of the magnetic oxides helped attain magnetic loss capabilities. This proposed nanocomposite also shows a good absorption with a minimum RL of –32.00 dB for a 3.0 mm thick sample, but the bandwidth remains relatively narrow (2.35 GHz), and the overall efficiency

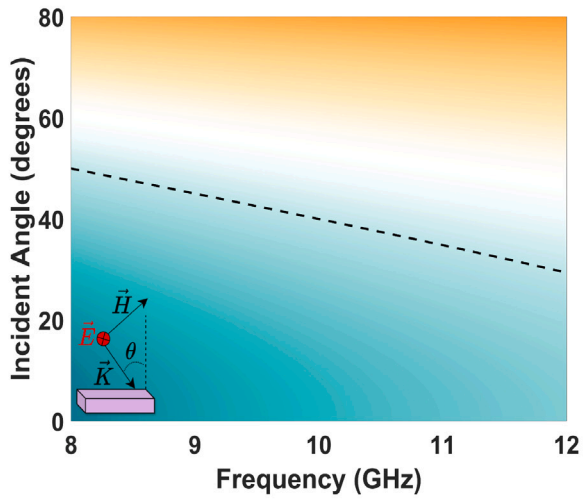

(a) RL contour of composite of 1.00 mm thick (under incidence of TE polarised waves)

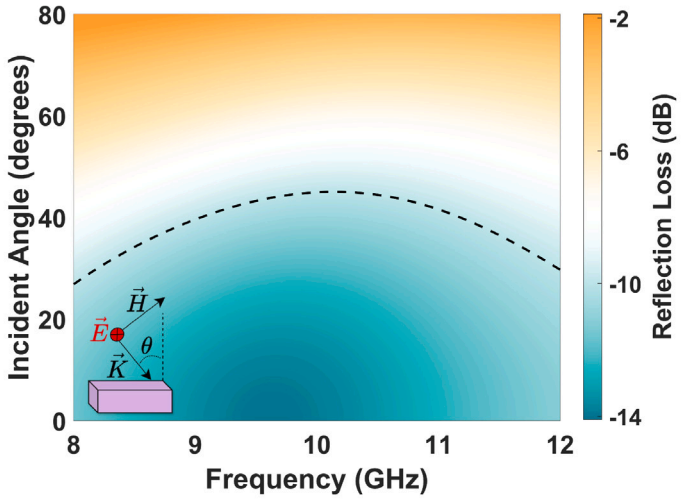

(b) RL contour of composite of 7.00 mm thick (under incidence of TE polarised waves)

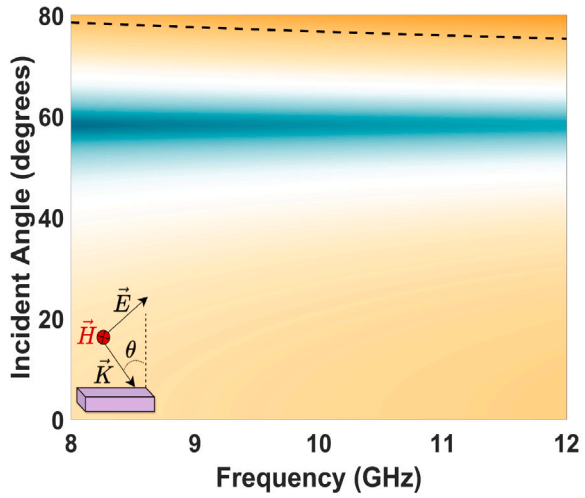

(c) RL contour of composite of 1.00 mm thick (under incidence of TM polarised waves)

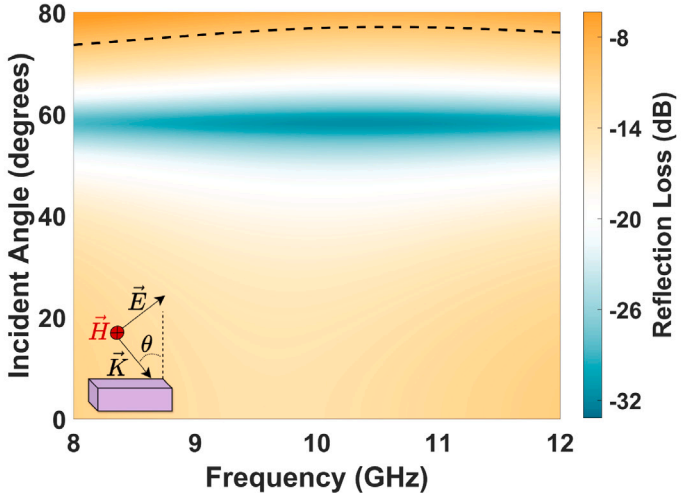

(d) RL contour of composite of 7.00 mm thick (under incidence of TM polarised waves)

Fig. 17. Reflection loss behaviour of multiphase composite with V_f = 2% BTO, 4% CFO, 2% MCT under the incidence of TE and TM polarised EM waves at varying incident angles.

(≈10.67 dB/mm) is notably lower than that of the present work. Kumar et al. [42] fabricated nanocomposite samples using calcium carbonate nanoplatelets (CCNPs) obtained from the mussel shell, which were reinforced into a Silane functionalised cardanol(SCF)-toughened epoxy matrix to mimic the composite structure of the abalone shell. The optimal sample reported a minimum RL of −43.0 dB but required a 10 mm thick sample, resulting in low efficiency of only −4.3 dB/mm and extremely narrow bandwidth (0.20 GHz), severely limiting their practical usability for broadband RL applications in the X-band frequency range.

$Ti_3C_2T_x$ MXene-based nanocomposites have already been widely studied for their electromagnetic absorption applications. To further enhance their minimum reflection loss (RL), Liu et al. [43] fabricated novel composites by introducing magnetic Co nanoparticles into $Ti_3C_2T_x$ MXene by using a simple solvothermal method. By introducing different contents of Co nanoparticles, the Co(CoO)/$Ti_3C_2T_x$ /TiO_2 nanocomposites RL capabilities is optimised. The optimal sample of 2.50 mm thickness has shown a minimum RL of −38.0 dB, resulting in an efficiency of ≈ −15.2 dB/mm, which is higher than the proposed composites in this current work. However, the bandwidth in the X-band is only 2.40 GHz. Guo et al. [44] fabricated a multiphase nanocomposite with magnetic and electric nanoparticles such as Co, MnO and $Ti_3C_2T_x$. Whereas the matrix is made up of a mixture of reduced graphene oxide (rGO) and MXene. This hybrid nanocomposite exhibited a minimum reflection loss of −32.1 dB with a 3.1 mm thickness, but both of these nanocomposites' reliance on expensive and environmentally unstable MXenes can be a challenge for scalability.

Pang et al. [45] developed a highly engineered nanocomposite comprising semiconducting β-SiC, conductive hafnium carbide (HfC)-carbon core–shell nanoparticles, and interconnected carbon nanoribbons, all dispersed in a SiO_2 matrix. By varying the filler volume fractions, they optimised the sample to achieve a minimum RL of –60.70 dB

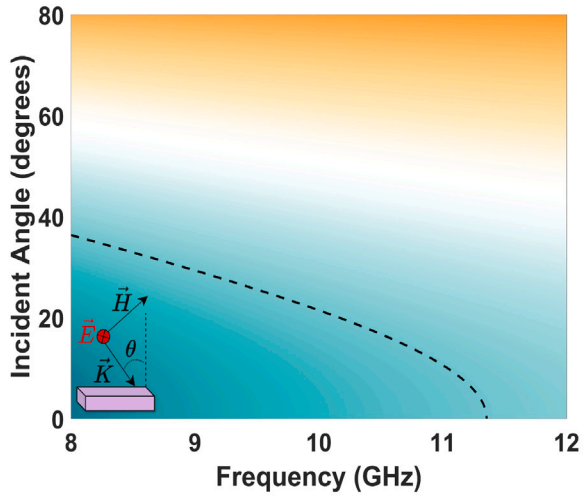

(a) RL contour of composite of 1.00 mm thick (under incidence of TE polarised waves)

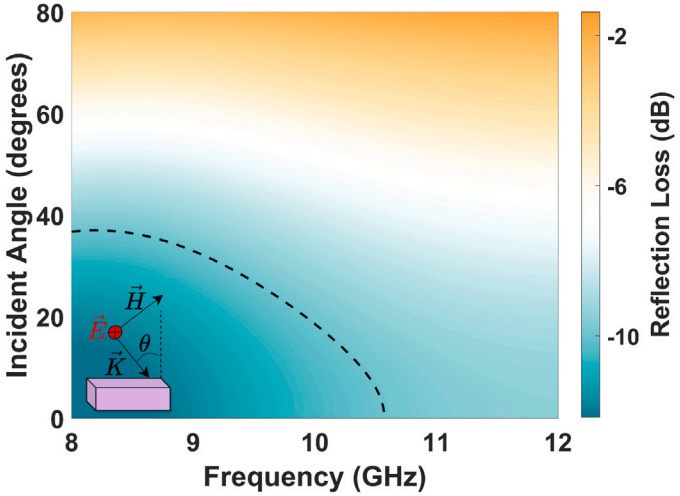

(b) RL contour of composite of 7.00 mm thick (under incidence of TE polarised waves)

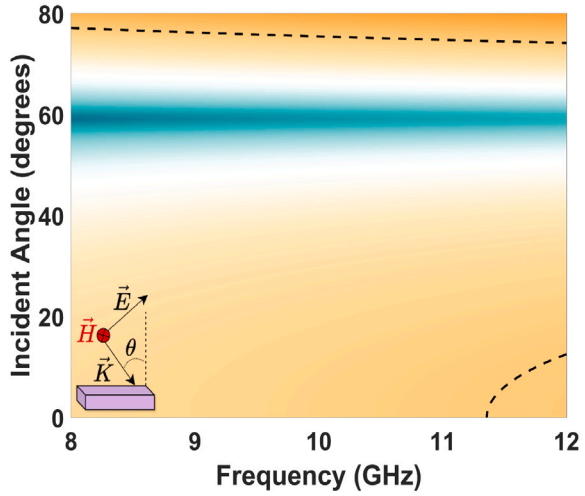

(c) RL contour of composite of 1.00 mm thick (under incidence of TM polarised waves)

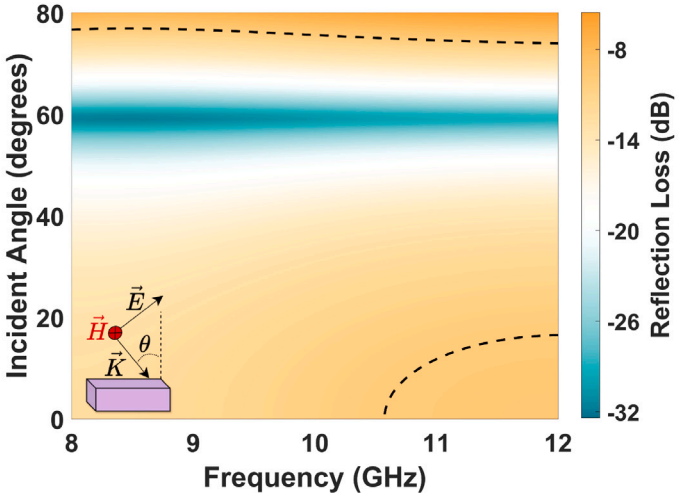

(d) RL contour of composite of 7.00 mm thick (under incidence of TM polarised waves)

Fig. 18. Reflection loss behaviour of multiphase composite with V_f = 4% BTO, 8% CFO, 4% MCT under the incidence of TE and TM polarised EM waves at varying incident angles.

at a thickness of 3.33 mm, with a 3.00 GHz bandwidth. This corresponds to a high efficiency of approximately −18.2 dB/mm. In another study, Wang et al. [46] fabricated (TiC/TiO_2/carbon ribbon)/SiOC nanocomposites using polymer-derived ceramics (PDCs) from a TiC-modified polysiloxane (PSO) precursor processed at 900 °C under Ar. The optimal sample, with a thickness of 2.80 mm, achieved a minimum RL of −30 dB and an efficiency of approximately −10.7 dB/mm, effectively covering the entire X-band.

In comparison with the literature works, the proposed multiphase nanocomposites, the present work offers a simple yet effective design by combining dielectric ($BaTiO_3$) and magnetic ($CoFe_2O_4$) ceramic nanoparticles with conductive MWCNTs in a polymer matrix, resulting in balanced absorption with minimal thickness. The excellent impedance matching and interfacial polarisation effects arising from the multiphase configuration contribute to the absorption of incident EM waves at reduced thickness. Therefore, the proposed ceramic-based nanocomposites outperform many complex or less scalable systems in terms of efficiency, manufacturability, and thickness sensitivity, making them highly promising candidates for next-generation broadband EM absorption applications. Also, all the literature works are experimental-driven methods to attain optimal composite sample configurations. For the first time, a minimal experiments-assisted computational approach is proposed in this work to attain optimal multiphase nanocomposite samples for broadband RL applications.

6. Conclusions

An integrated experimental computational research methodology is proposed in the current study to analyse the multiphase composites with ceramic inclusions ($BaTiO_3$ (BTO), $CoFe_2O_4$ (CFO), MWCNTs (MCT)) for broadband reflection loss capabilities. XRD and Raman analysis are carried out to characterise the nanoparticles used in the fabrication. TGA, SEM and X-ray micro-CT analysis are carried out to characterise the fabricated nanocomposite samples. All the fabricated composites are tested using a two-port VNA setup to extract the scattering parameters of the composite in the X-band frequency range. The effective properties of the composites are obtained from the

Table 5
Comparison of thickness (in mm), minimum reflection loss (-RL in dB) and bandwidth (in GHz) of the multiphase nanocomposites proposed in the present work with the reported multiphase composites in the X-band frequency range.

Nanoparticles, Matrix	Thickness	-RL, Bandwidth
(i) $BaTiO_3/CoFe_2O_4$/MWCNTs, Epoxy	01.00	14.10, 4.00
(ii) $BaTiO_3/CoFe_2O_4$/MWCNTs, Epoxy	01.00	12.16, 3.36
$LaFeO_3$/Fe@CNTs, Paraffin [39]	02.50	38.76, 2.20
$Co_{5.47}N/Ni_4N$, Carbon fibre [40]	02.90	43.82, 4.00
Fe/Co oxide@α-Fe, Paraffin [41]	03.00	32.00, 2.35
CCNPs, Epoxy modified with SFC [42]	10.00	43.00, 0.20
$Co/CoO/TiO_2$, $Ti_3C_2T_x$ MXene [43]	02.50	38.00, 2.40
$Co/MnO/Ti_3C_2T_x$, MXene/rGO [44]	03.10	32.10, 4.00
SiC/HfC/C, SiO_2 [45]	03.33	60.70, 3.00
TiC/TiO_2/C, SiOC [46]	02.80	30.00, 4.00

Nicolson-Ross-Weir (NRW) algorithm (using the scattering parameters). The electromagnetic properties of the individual nanoparticles, along with the interaction parameters in the Lichterecker mixing rule, are extracted using the in-house optimisation tool (based on Nelder–Mead simplex and L-BFGS methods). Using the effective electromagnetic properties and the actual volume fraction (obtained from TGA), the reflection loss (RL) spectrum in the X-band frequency range is obtained using the in-house transfer matrix method (TMM). Both the in-house tools are validated with the experimental results. The reliability of the methodology is underscored by the close agreement between computational predictions and experimental results (3%–4% deviation in properties, 5% in RL), ensuring consistent performance across diverse composite configurations. In the current study, the influencing parameters on the RL, such as volume fraction of BTO, CFO, MCT, the thickness of the multiphase composite, incident angle, and the polarisation of the incident EM waves, are varied. It should be noted that the proposed methodology is a generalised approach to designing multiphase composites for broadband RL applications.

Two different parametric studies are out. The first one is to identify the influence of individual nanoparticles along with the thickness of the composite under the normal incidence of TE polarised EM waves. The second parametric study assesses the impact of incidence angle and polarisation (TE and TM) on broadband reflection loss performance. The main objective is to ensure broadband reflection loss across the frequency range, i.e. bandwidth of 4.4 GHz (RL < −10 dB). The thickness of the sample is increased to 10 mm, starting from 1 mm, and the other parameters like V_f of BTO, CFO and MCT nanoparticles are varied from 1% to 20%. The following observations are obtained from the study:

- When the BTO and MCT loading is greater than 10% (while other nanoparticle's volume fraction is fixed as 1%), not even at a single thickness configuration, a complete bandwidth of 4.4 GHz covering the entire X-band frequency is obtained.
- Based on the RL plots of CFO-dominated nanocomposites, it is inferred that CFO loading provided broadband bandwidth even at a high-volume fraction of CFO nanoparticles, and there is a large range of thickness configurations where this broad bandwidth is attained.
- At lower incident angles in transverse electric (TE) polarisation, the composite's moderate permittivity and permeability, coupled with the relatively optimal impedance matching among the materials, enable the electric field to engage initially and dissipate energy via dielectric losses, leading to broadband RL.
- As the incidence angle increases, the altered electric field path length and the absence of magnetic field enhancement at the interfaces become the primary factors, disrupting effective impedance matching conditions at elevated incident angles and consequently limiting the composite's broadband RL capabilities.
- Under the incidence of TM polarised EM waves, the variation in the permittivity between the nanoparticles and the epoxy results in significant electric field interaction. The combined effect of dielectric losses and multiple scattering resulted in broadband RL across a broad range of incident angles (≈ up to 78°).

The inferences attained from the proposed study identified that the multiphase composite with $BaTiO_3$, $CoFe_2O_4$ and MWCNTs can attain broadband reflection loss in the X-band frequency range for different combinations of nanoparticles. The proposed integrated methodology is a generalised approach that helps attain the optimal configurations for any arbitrary mixture of multiphase composites for band-specific or broadband reflection loss applications.

CRediT authorship contribution statement

A. Phanendra Kumar: Conceptualization, Methodology, Writing – original draft, Visualization, Validation, Software, Investigation, Formal analysis, Data curation. **Rishi Raj:** Writing – review & editing, Investigation, Data curation. **Dineshkumar Harursampath:** Conceptualization, Writing – review & editing, Supervision, Resources. **Sathiskumar Anusuya Ponnusami:** Conceptualization, Methodology, Writing – review & editing, Supervision.

Declaration of competing interest

The authors declare that they have no known competing financial interests or personal relationships that could have appeared to influence the work reported in this paper.

Acknowledgement

The first author would like to acknowledge the Prime Minister's Research Fellowship Scheme, India, for the support during the research.

Appendix

The crystal structure and phase composition of the $BaTiO_3$ sample were investigated using X-ray diffraction (XRD) analysis, as shown in Fig. A1(a). The XRD pattern exhibits sharp, well-defined peaks, indicating the formation of a highly crystalline material. The observed peaks can be primarily indexed to the characteristic reflections of the tetragonal phase of $BaTiO_3$ (JCPDS card no. 05-0626) [47,48]. The prominent peaks at 2θ values of 22.0°, 31.5°, 38.9°, 45.4°, 50.8°, 56.1°, 65.8°, 70.4°, 75.0° and 79.2° correspond to the (001), (110), (111), (200), (210), (211), (202), (212), (310), and (311) planes of the $BaTiO_3$ crystal structure, respectively. The Raman spectra of the $BaTiO_3$ nanoparticles are shown in Fig. A1(b) and peaks are available at 156 cm^{-1}, 272 cm^{-1}, 383 cm^{-1}, 452 cm^{-1}, 461 cm^{-1}, 617 cm^{-1}, 647 cm^{-1}, which is typical for ferroelectric Barium Titanate nanoparticles. The peak at 272 cm^{-1} can be related to the E(TO) mode, which is attributed to the Ti-O stretching within the TiO_6. It is often found in tetragonal $BaTiO_3$, indicating a non-cubic phase. The peak in the region at 383 cm^{-1} can be associated with the A_1(TO) mode. This mode is attributed to TiO_6 octahedral vibrations and is an important feature of the tetragonal phase. This implies that the barium titanate has a well-enhanced ferroelectric material property. The peaks at 452 cm^{-1} and 461 cm^{-1} are usually attributed to the E(LO) mode. These close-lying peaks mean a small degree of symmetry breaking or slight distortion in the $BaTiO_3$ lattice unit cell. This still indicates that the Barium titanate particles are in the tetragonal phase. The peaks at 617 cm^{-1} and 647 cm^{-1} are generally attributed to the A_1(LO) and E(LO) modes. They are related to the higher-order phonon modes and can exist in tetragonal $BaTiO_3$. These peaks indicate that the $BaTiO_3$ nanoparticles sample may contain a mixture of a tetragonal phase and a small rhombohedral phase. The 2θ vs intensity plot obtained

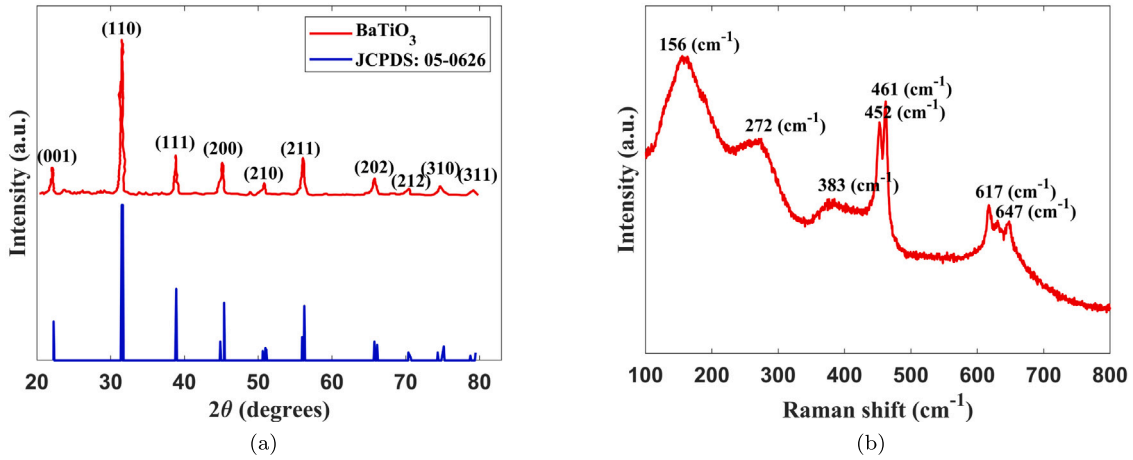

Fig. A1. (a) X-ray diffraction (XRD) pattern of $BaTiO_3$ compared with JCPDS card no. 05-0626, showing characteristic peaks corresponding to the tetragonal phase. (b) Raman spectra of $BaTiO_3$, indicating distinct vibrational modes at 156, 272, 383, 461, 617, and 647 cm^{-1}, which are consistent with the expected phonon modes of $BaTiO_3$.

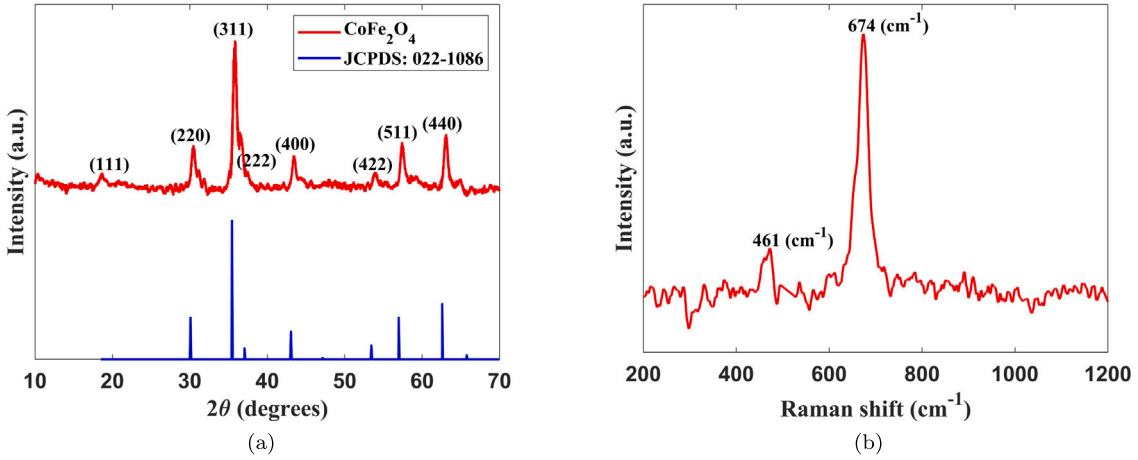

Fig. A2. (a) X-ray diffraction (XRD) pattern of $CoFe_2O_4$ compared with JCPDS card no. 022-1086, showing prominent peaks that confirm the centered-cubic crystal structure. (b) Raman spectra of $CoFe_2O_4$, highlighting vibrational modes at 461 and 674 cm^{-1}, which correspond to the typical phonon modes of spinel ferrite.

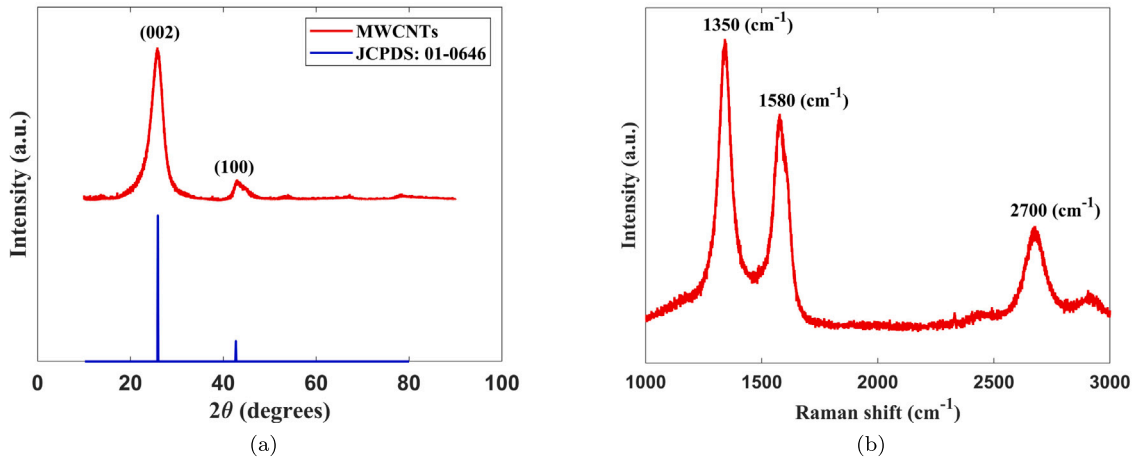

Fig. A3. (a) X-ray diffraction (XRD) pattern of multi-walled carbon nanotubes (MWCNTs) compared with JCPDS card no. 01-0646, showing distinct peaks at (002) and (100) planes, indicating the graphitic structure of MWCNTs. (b) Raman spectra of MWCNTs, highlighting the D-band at 1350 cm^{-1}, G-band at 1580 cm^{-1}, and 2D-band at 2700 cm^{-1}, which are characteristic features of graphitic materials and provide insight into the degree of disorder and graphitisation.

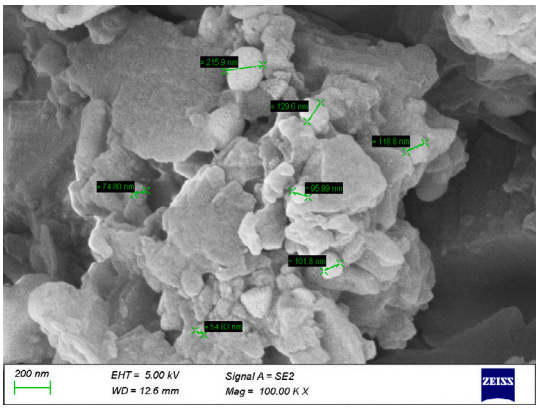

(a) BTO-based composite with particles size representation at 100k.

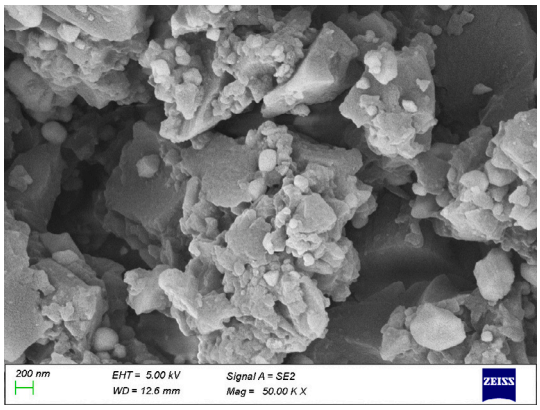

(b) BTO-based composite at 50k.

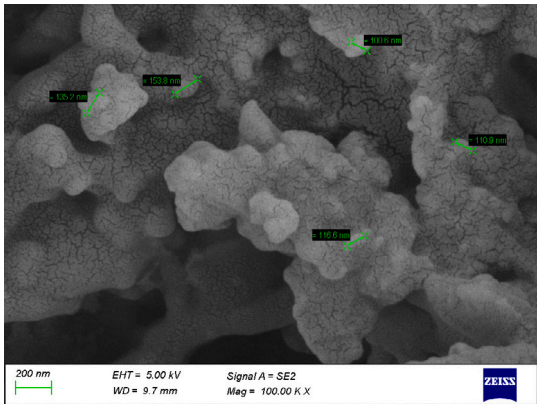

(c) CFO-based composite with particles size representation at 100k.

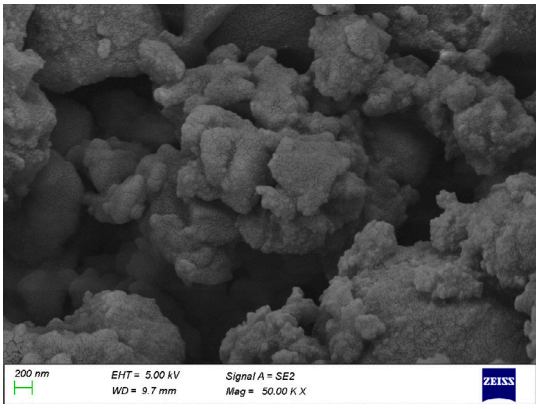

(d) CFO-based composite at 50k.

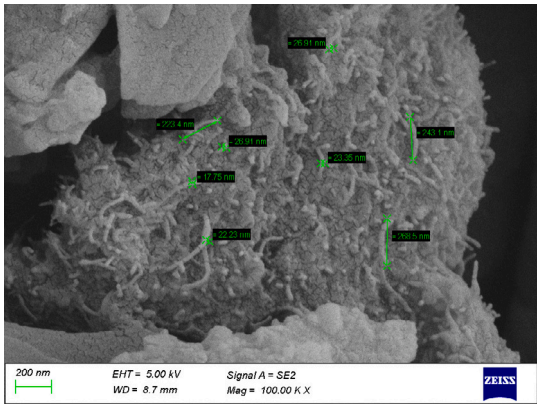

(e) MCT-based composite with particles size representation at 100k.

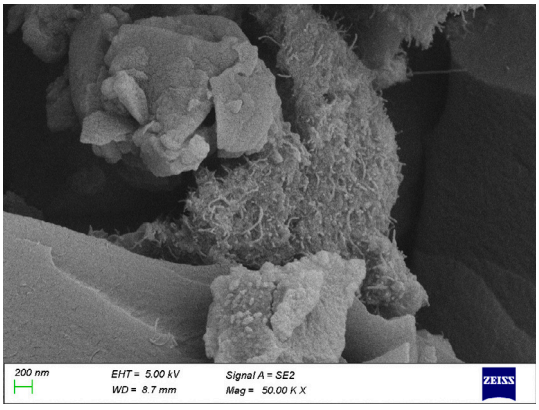

(f) MCT-based composite at 50k.

Fig. A4. Scanning Electron Microscopy (SEM) images of two-phase nanocomposites illustrating the morphology and dispersion of the particles inclusions. The scale bar represents 200 nm.

from the XRD analysis performed on the $CoFe_2O_4$ nanoparticles is shown in Fig. A2(a). The observed peaks can be indexed to the characteristic reflections of the centred-cubic crystal structure of $CoFe_2O_4$ particles (JCPDS card no. 022-1086) [49,50]. The prominent peaks at 2θ values of 18.2°, 30.1°, 35.5°, 37.0°, 43.0°, 53.4°, 56.9°, and 62.5° correspond to the (111), (220), (311), (222), (400), (422), (511), and (440) planes of the $CoFe_2O_4$ crystal structure, respectively. The intensity and sharpness of these peaks suggest the high crystallinity and phase purity of the $CoFe_2O_4$ sample. From the group theory analysis, $CoFe_2O_4$ nanoparticles exhibit five Raman active modes of vibrations such as E_g (278–293 cm^{-1}), $3T_{2g}$ (539–565 cm^{-1}, 449–471 cm^{-1}, 163–177 cm^{-1}) and A_{1g} (648–680 cm^{-1}) [51,52]. From Fig. A2(b), it can be observed that two peaks were observed at 461 cm^{-1} and 674 cm^{-1}. The two Raman peaks observed above and below 650 cm^{-1}

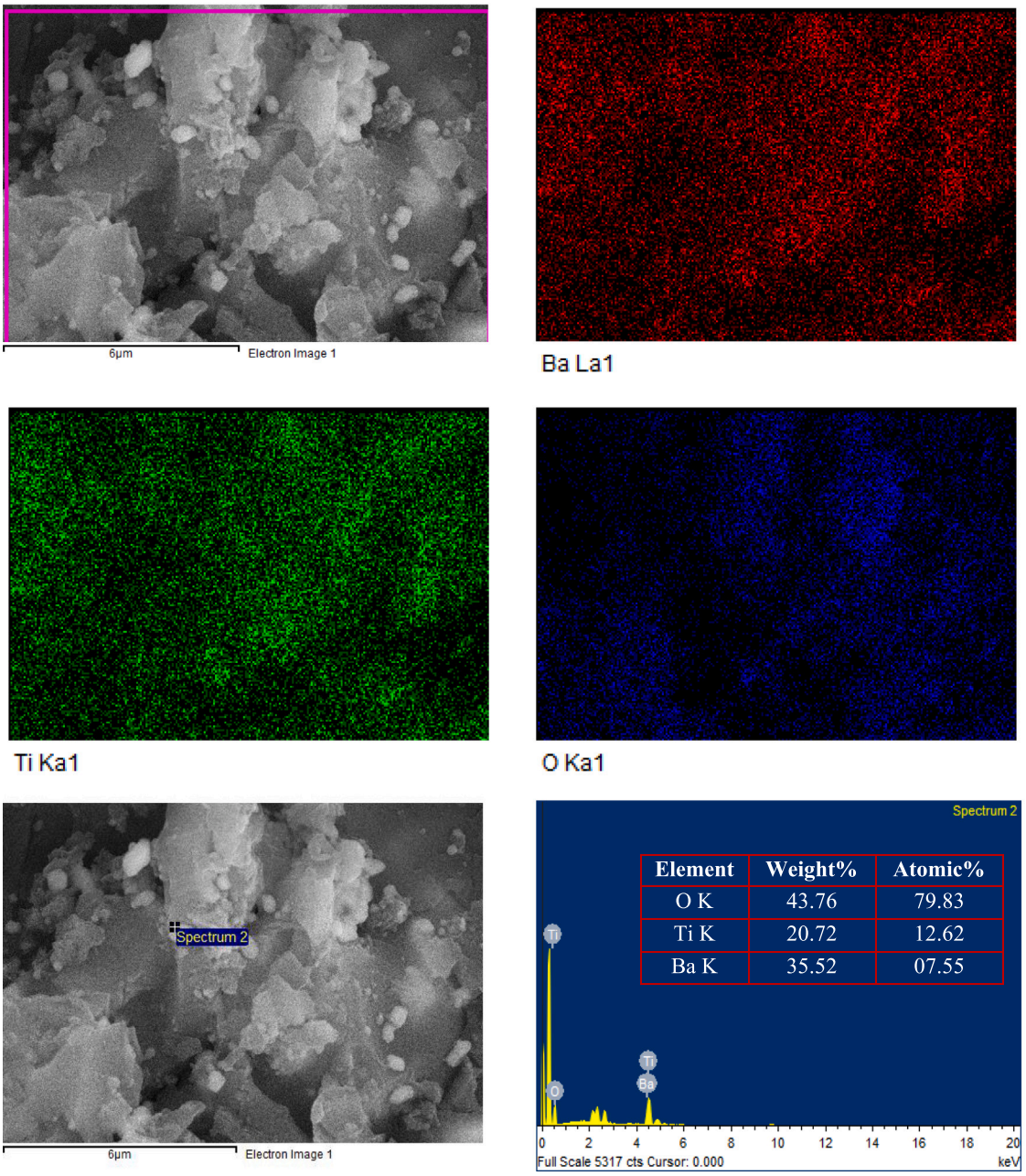

Fig. A5. Elemental mapping of Ba-L, Ti-K and O-K of BTO composite in the region selected in the SEM image is shown. The point EDS spectrum of the BTO composite with different elements is shown in the graph, with the *X*-axis representing energy in keV and the *Y*-axis showing the counts of detected X-rays. Major peaks correspond to the elements present in the sample, including Barium (Ba), Titanate (Ti) and oxygen (O). A table is provided with the weight percentage and atomic percentage of each element in the image area selected.

indicate vibrations of oxygen in the tetrahedral lattice site (AO_4) and octahedral lattice site (Fe-O and Co-O) respectively [53,54]. Therefore, these two vibration modes represent the oxygen vibration and have resulted in two detectable peaks A_{1g} and $T_{2g}(2)$ [55]. In the case of normal spinel ferrites, the Raman modes for A_{1g} symmetry will be in the range of 600–650 cm^{-1} [52]. But the peak at 674 cm^{-1} represents the inverse spinel structure of the $CoFe_2O_4$ nano particles used in the current study. The existence of Raman bands at ~ 240 cm^{-1} $CoFe_2O_4$ corresponds to impurities like α-Fe2O3 [56], but the observed bands in Fig. A2(b) confirms the non-existence of these impurities.

The XRD pattern attained for MWCNTs is shown in Fig. A3(a), and the observed peaks can be attributed to the characteristic reflections of the hexagonal graphite structure [57]. The XRD pattern exhibits characteristic peaks that can be indexed to the graphitic structure of carbon nanotubes. The prominent peaks at 2θ values of approximately 26.2° and 42.9° correspond to the (002) and (100) planes of MWCNTs, respectively, which is consistent with the standard JCPDS card no. 01-0646 [58,59]. The (002) peak indicates the graphitic interlayer spacing, while the (100) peak corresponds to the in-plane reflection [59]. The sharpness and intensity of these peaks suggest that the MWCNTs have a high degree of crystallinity and well-ordered graphitic layers. Raman

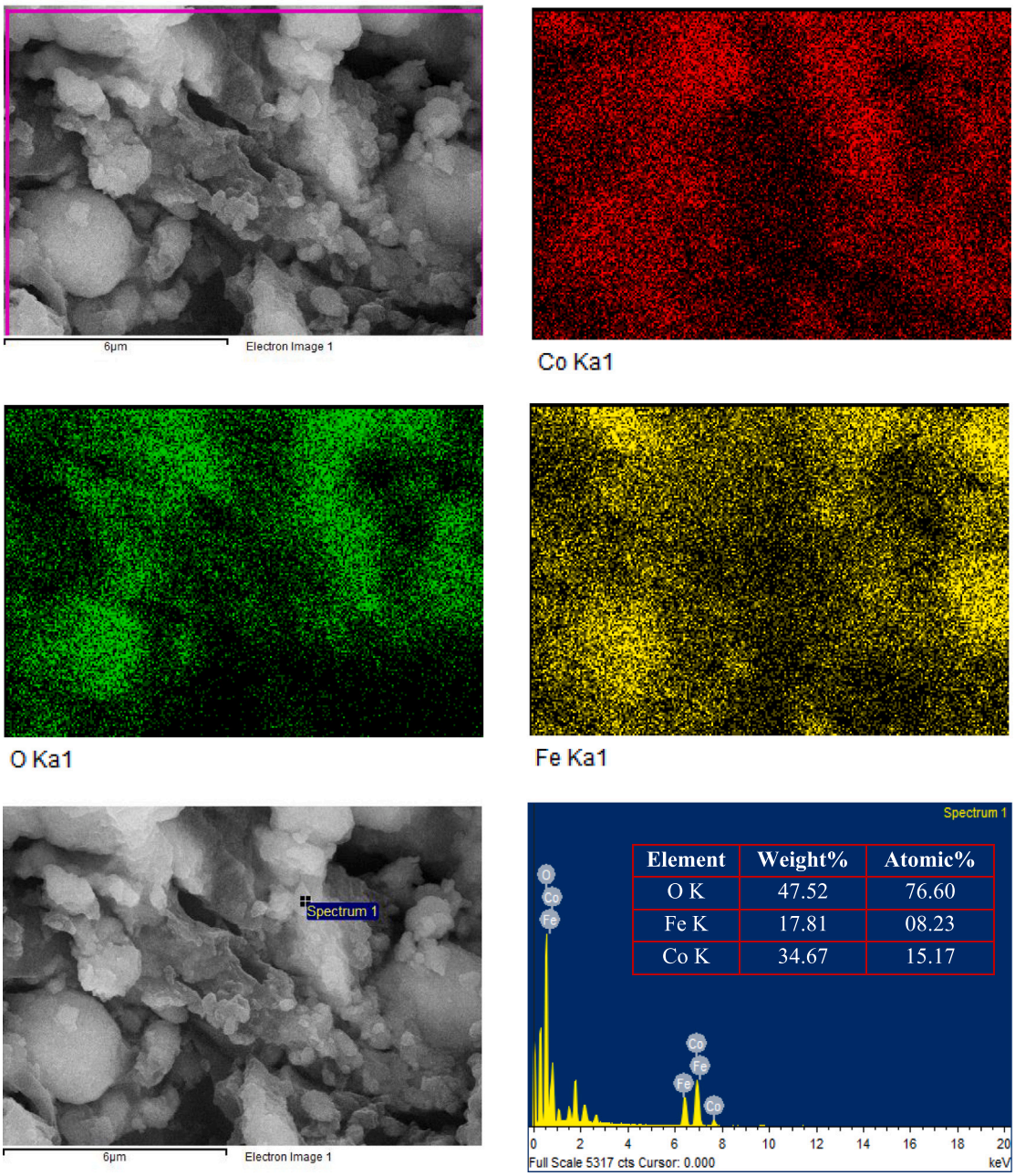

Fig. A6. Elemental mapping of Co-K, Fe-K and O-K of CFO composite in the region selected in the SEM image is shown. The point EDS spectrum of the CFO composite with different elements is shown in the graph, with the *X*-axis representing energy in keV and the *Y*-axis showing the counts of detected X-rays. Major peaks correspond to the elements present in the sample, including Ferrite (Fe), Cobalt (Co) and oxygen (O). A table is provided with the weight percentage and atomic percentage of each element in the image area selected.

spectroscopy was employed to investigate the structural characteristics of the MWCNTs further, as shown in Fig. A3(b). The Raman spectrum displays two prominent peaks, the D-band at around 1350 cm^{-1} and the G-band at around 1580 cm^{-1}. The D-band is associated with the disorder-induced mode, which arises due to the presence of defects and amorphous carbon in the MWCNTs [60,61]. The G-band corresponds to the tangential stretching mode of sp^2-bonded carbon atoms in the graphitic layers [62]. The intensity ratio of the D-band to the G-band I_D/I_G is approximately 1.29, indicating a moderate level of disorder in the MWCNTs [60,61]. A higher I_D/I_G ratio suggests greater defects or amorphous carbon content [63]. The Raman spectrum also shows a weak 2D band at around 2700 cm^{-1}, which is a second-order overtone of the D-band and indicates the presence of a few-layered graphene structures within the MWCNTs [60,61].

Data availability

Data will be made available on request.

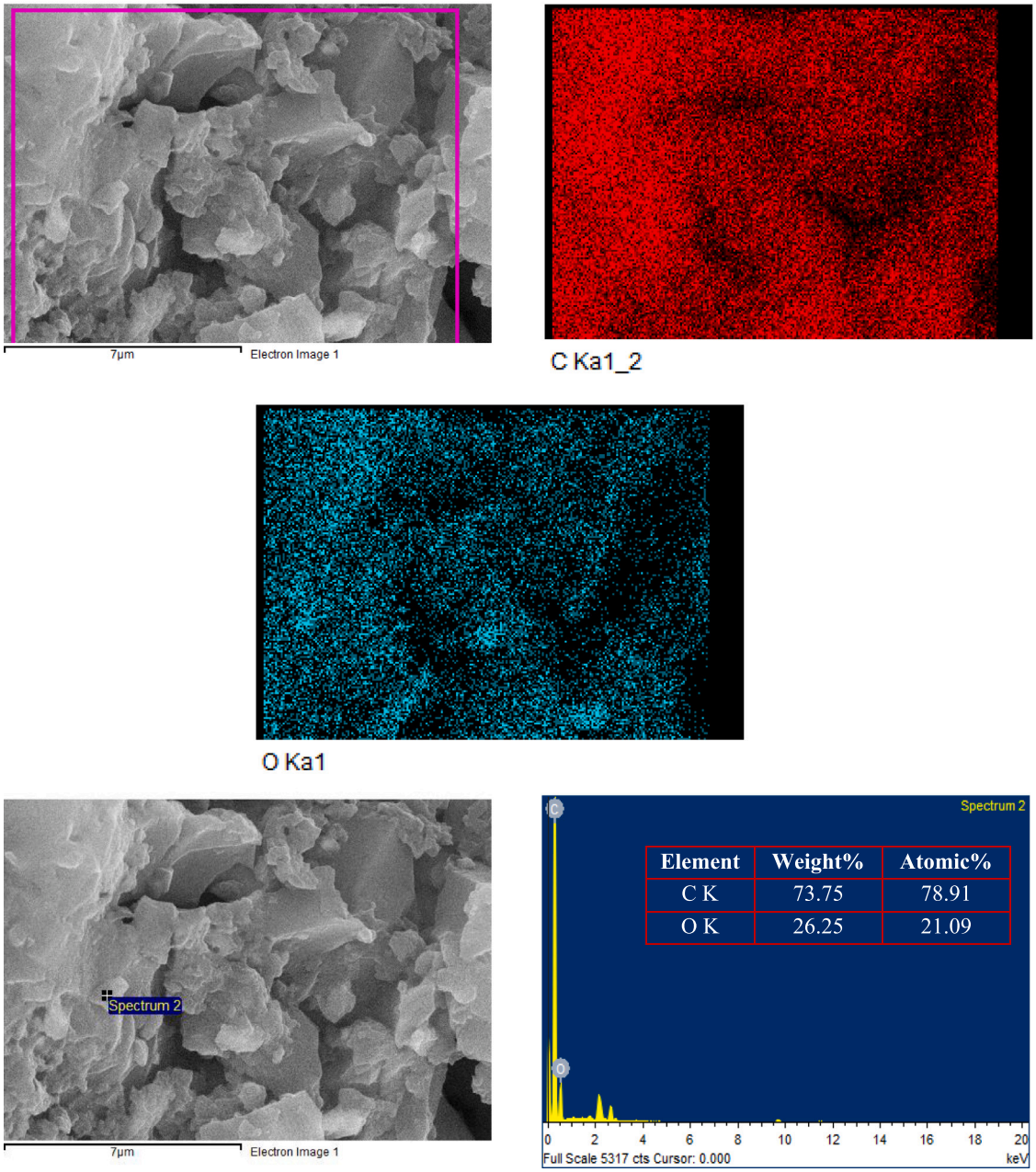

Fig. A7. Elemental mapping of C-K, O-K of MCT composite in the region selected in the SEM image is shown. The point EDS spectrum of the MCT composite with different elements is shown in the graph, with the *X*-axis representing energy in keV and the *Y*-axis showing the counts of detected X-rays. Major peaks correspond to the elements present in the sample, including carbon (C) and oxygen (O). A table is provided with the weight percentage and atomic percentage of each element in the image area selected.

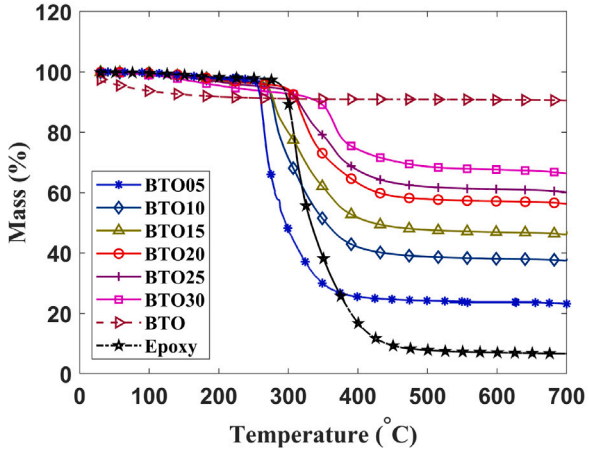

(a) TGA analysis of $BaTiO_3$ composites, showing the mass loss behavior at different temperatures for $BaTiO_3$ with varying volume fractions (5%, 20%, 30%) and pure epoxy.

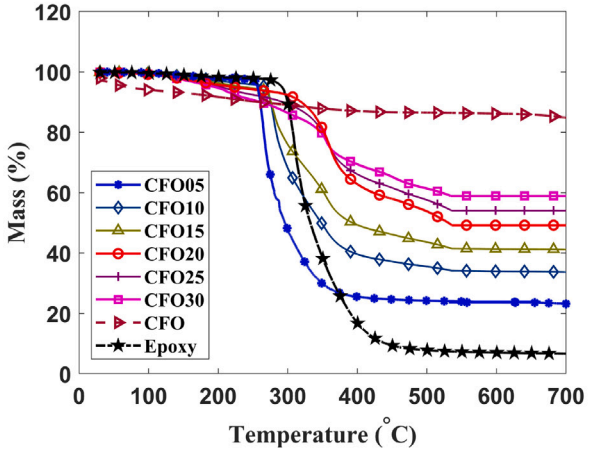

(b) TGA analysis of $CoFe_2O_4$ composites, demonstrating thermal degradation trends at different temperatures for $CoFe_2O_4$ with volume fractions of 5%, 20%, and 30%, compared to pure epoxy.

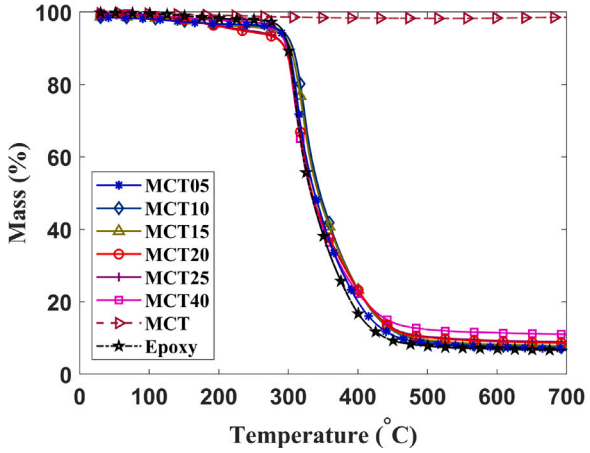

(c) TGA analysis of MWCNT composites, illustrating the mass degradation profiles of MWCNT composites with 5%, 20%, and 40% volume fractions alongside pure epoxy.

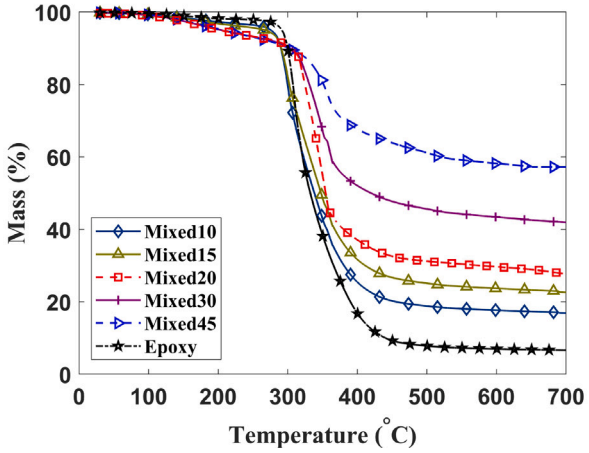

(d) TGA analysis of mixed samples (with $BaTiO_3$, $CoFe_2O_4$, MWCNT nanoparticles), showing the thermal stability and mass loss for mixed composites at 20% and 45% volume fractions compared to epoxy.

Fig. A8. TGA analysis of $BaTiO_3$, $CoFe_2O_4$, MWCNT, and mixed composites, providing a comprehensive comparison of thermal degradation behaviour across different material compositions and volume fractions.

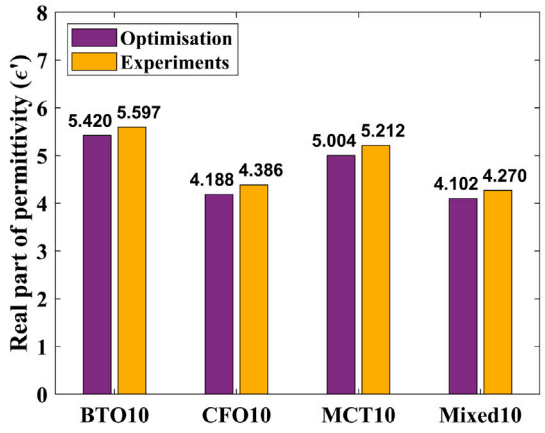

(a) Real part of the permittivity of the nanocomposites with 10% volume fraction

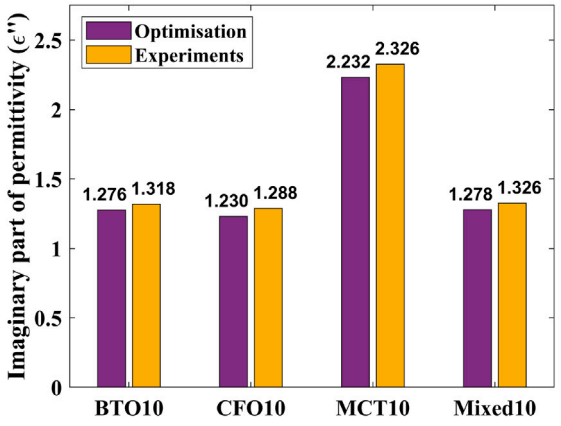

(b) Imaginary part of the permittivity of the nanocomposites with 10% volume fraction

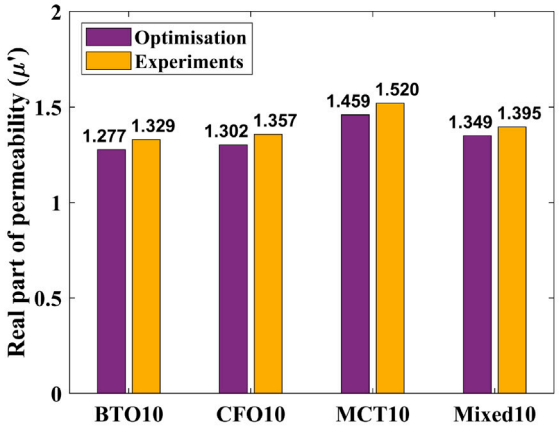

(c) Real part of the permeability of the nanocomposites with 10% volume fraction

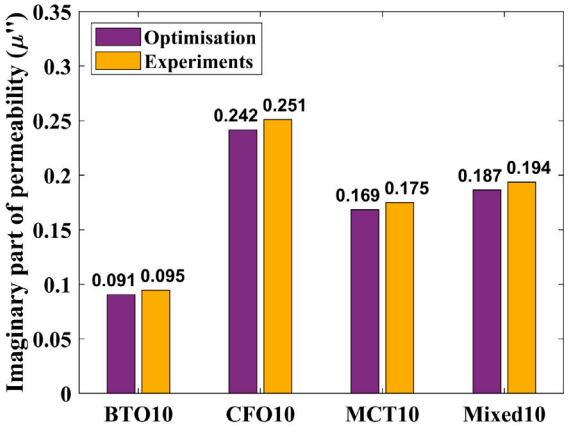

(d) Imaginary part of the permeability of the nanocomposites with 10% volume fraction

Fig. A9. Comparison of the electromagnetic properties of the nanocomposites with 10% volume fraction obtained from experiments (in yellow) and optimisation (in violet). Where Mixed10 contains 03% $BaTiO_3$, 04% $CoFe_2O_4$ and 03% MWCNTs nanoparticles inside epoxy.

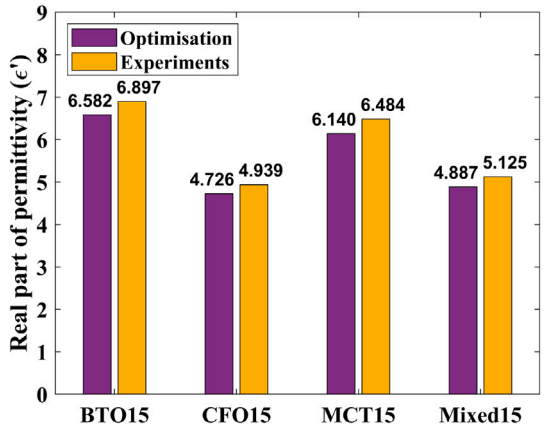

(a) Real part of the permittivity of the nanocomposites with 15% volume fraction

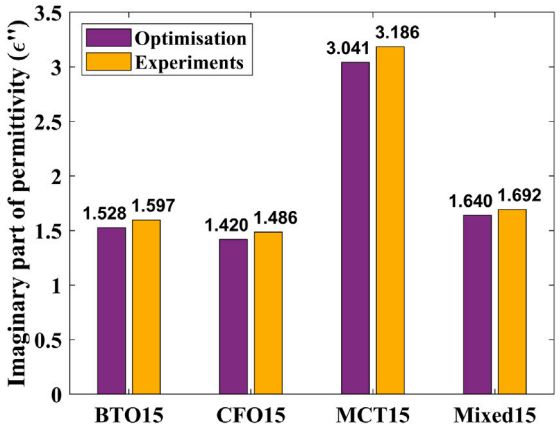

(b) Imaginary part of the permittivity of the nanocomposites with 15% volume fraction

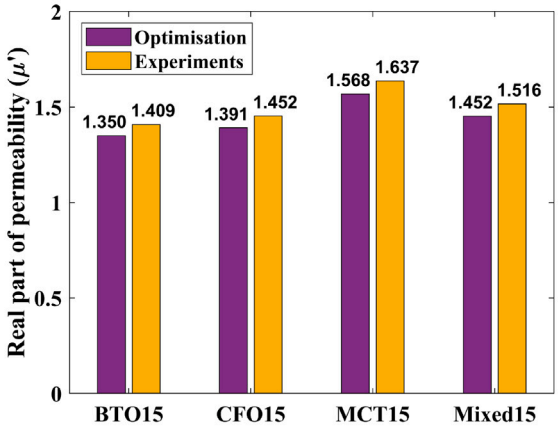

(c) Real part of the permeability of the nanocomposites with 15% volume fraction

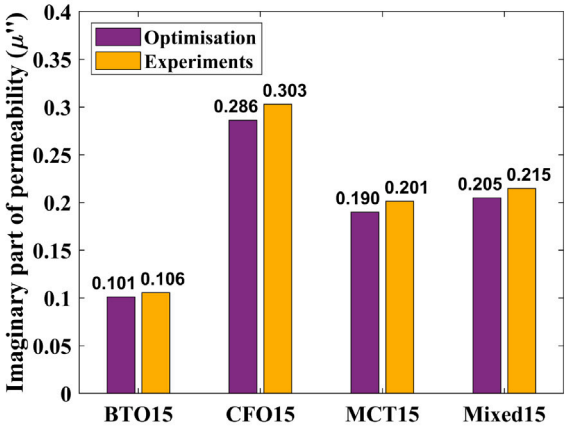

(d) Imaginary part of the permeability of the nanocomposites with 15% volume fraction

Fig. A10. Comparison of the electromagnetic properties of the nanocomposites with 15% volume fraction obtained from experiments (in yellow) and optimisation (in violet). Where Mixed15 contains 05% $BaTiO_3$, 05% $CoFe_2O_4$ and 05% MWCNTs nanoparticles inside epoxy.

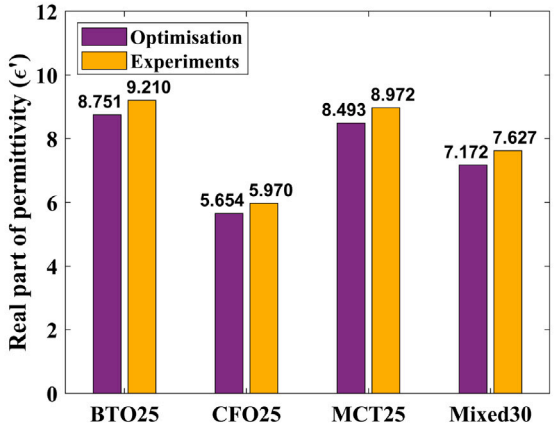

(a) Real part of the permittivity of the nanocomposites with 25% volume fraction of two phase and 30% volume fraction of multiphase composites

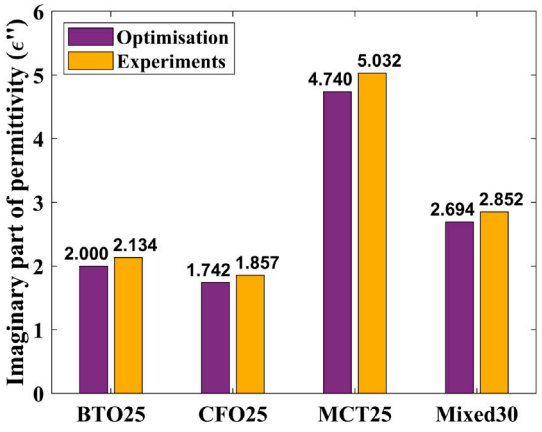

(b) Imaginary part of the permittivity of the nanocomposites with 25% volume fraction of two phase and 30% volume fraction of multiphase composites

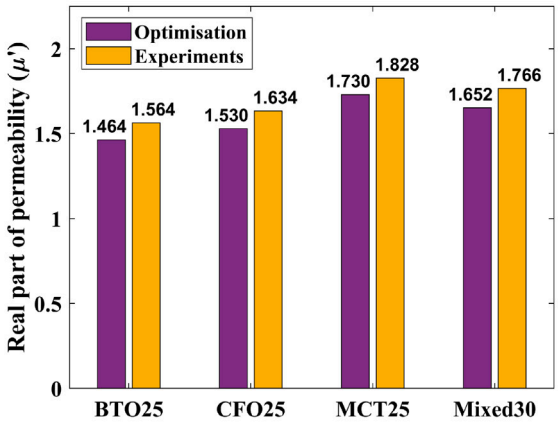

(c) Real part of the permeability of the nanocomposites with 25% volume fraction of two phase and 30% volume fraction of multiphase composites

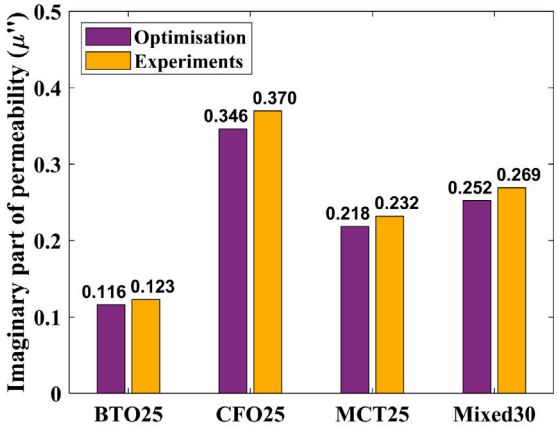

(d) Imaginary part of the permeability of the nanocomposites with 25% volume fraction of two phase and 30% volume fraction of multiphase composites

Fig. A11. Comparison of the electromagnetic properties of the two phase nanocomposites with 25% and mixed composite with 30% volume fraction obtained from experiments (in yellow) and optimisation (in violet). Where Mixed30 contains 10% $BaTiO_3$, 10% $CoFe_2O_4$ and 10% MWCNTs nanoparticles inside epoxy.

References

[1] L. Du, Y. Li, Q. Zhou, T. Shi, L. Zhang, J. Wang, X. Wang, X. Fan, A flexible metamaterial based on CNTs/Cellulose aerogels for broadband and ultra-lightweight microwave absorbers, Compos. Sci. Technol. 261 (2025) 111024.

[2] A.P. Kumar, D. Harursampath, S.A. Ponnusami, A novel engineered sandwich composite with ceramic-coated graphite fibre-reinforced face sheets and an auxetic core for enhanced broadband electromagnetic absorption: design using multiscale computational analysis, Smart Materials and Structures 33 (11) (2024) 115004.

[3] Q. Zhou, T. Shi, B. Xue, S. Gu, W. Ren, F. Ye, X. Fan, L. Du, Multi-scale integrated design and fabrication of ultra-broadband electromagnetic absorption utilizing multi-walled carbon nanotubes-based hierarchical metamaterial, Compos. Sci. Technol. 232 (2023) 109877.

[4] R. Tan, F. Zhou, P. Chen, B. Zhang, J. Zhou, PANI/FeCo@ C composite microspheres with broadband microwave absorption performance, Compos. Sci. Technol. 218 (2022) 109143.

[5] Q. Wu, J. Wang, H. Jin, Y. Dong, S. Huo, S. Yang, X. Su, B. Zhang, Facile synthesis of Co-embedded porous spherical carbon composites derived from Co3O4/ZIF-8 compounds for broadband microwave absorption, Compos. Sci. Technol. 195 (2020) 108206.

[6] N. Zhang, P. Chen, Y. Wang, M. Zong, W. Chen, Supramolecular self-assembly derived Mo2C/FeCo/NC hierarchical nanostructures with excellent wideband microwave absorption properties, Compos. Sci. Technol. 221 (2022) 109325.

[7] Y.-Y. Wang, W.-J. Sun, K. Dai, D.-X. Yan, Z.-M. Li, Flexible and heat-resistant carbon nanotube/graphene/polyimide foam for broadband microwave absorption, Compos. Sci. Technol. 212 (2021) 108848.

[8] L. Vovchenko, O. Lozitsky, L. Matzui, V. Oliynyk, V. Zagorodnii, Microwave shielding and absorbing properties of single-and multilayered structures based on two-phase filler/epoxy composites, Appl. Nanosci. 12 (4) (2022) 1037–1049.

[9] X.-M. Meng, X.-J. Zhang, C. Lu, Y.-F. Pan, G.-S. Wang, Enhanced absorbing properties of three-phase composites based on a thermoplastic-ceramic matrix (BaTiO 3+ PVDF) and carbon black nanoparticles, J. Mater. Chem. A 2 (44) (2014) 18725–18730.

[10] N. Wang, K. Nan, H. Zheng, Q. Xue, W. Wang, Y. Wang, Two-phase magnetic nanospheres with magnetic coupling effect encapsulated in porous carbon to achieve lightweight and efficient microwave absorbers, J. Colloid Interface Sci. 671 (2024) 56–66.

[11] M. Valentini, F. Piana, J. Pionteck, F. Lamastra, F. Nanni, Electromagnetic properties and performance of exfoliated graphite (EG)–thermoplastic polyurethane (TPU) nanocomposites at microwaves, Compos. Sci. Technol. 114 (2015) 26–33.

[12] Z. He, C. Wang, R. Sun, S. Liu, L. Ding, T. Gao, P. Liu, Hollow engineering of HCNs@ CoFe 2 se 4-QDs with quantum dots toward ultra-broadband electromagnetic wave absorption, J. Adv. Ceram. 14 (4) (2025).

[13] P. Liu, Y. Li, H. Xu, L. Shi, J. Kong, X. Lv, J. Zhang, R. Che, Hierarchical Fe-Co@ TiO2 with incoherent heterointerfaces and gradient magnetic domains for electromagnetic wave absorption, ACS Nano 18 (1) (2023) 560–570.

[14] J. Zhao, Z. Wang, H. Wang, P. Liu, R. Che, Controllable design of "nested doll" MoS2/V2O3 heterostructures promotes polarization effects for high-efficiency microwave absorption, Adv. Funct. Mater. 35 (14) (2025) 2418282.

[15] J. Ma, U. Azhar, C. Zong, Y. Zhang, A. Xu, C. Zhai, L. Zhang, S. Zhang, Core-shell structured PVDF@ BT nanoparticles for dielectric materials: A novel composite to prove the dependence of dielectric properties on ferroelectric shell, Mater. Des. 164 (2019) 107556.
[16] X. Chen, G. Wang, Y. Duan, S. Liu, Electromagnetic characteristics of barium titanate/epoxide resin composites in X and Ku bands, J. Alloys Compd. 453 (1–2) (2008) 433–436.
[17] G.C. Manika, G.C. Psarras, Energy storage and harvesting in BaTiO3/epoxy nanodielectrics, High Volt. 1 (4) (2016) 151–157.
[18] L. Jing, G. Wang, Y. Duan, Y. Jiang, Synthesis and electromagnetic characteristics of the flake-shaped barium titanate powder, J. Alloys Compd. 475 (1–2) (2009) 862–868.
[19] J. Cai, B. Xie, Y. Jiang, J. Lu, Z. Li, P. Mao, M.A. Marwat, H. Zhang, Design and preparation of ternary polymer nanocomposites for high energy density film capacitors, Compos. Sci. Technol. 245 (2024) 110361.
[20] F. Sharifianjazi, M. Moradi, N. Parvin, A. Nemati, A.J. Rad, N. Sheysi, A. Abouchenari, A. Mohammadi, S. Karbasi, Z. Ahmadi, et al., Magnetic CoFe2O4 nanoparticles doped with metal ions: a review, Ceram. Int. 46 (11) (2020) 18391–18412.
[21] S. Amiri, H. Shokrollahi, The role of cobalt ferrite magnetic nanoparticles in medical science, Mater. Sci. Eng.: C 33 (1) (2013) 1–8.
[22] S. Deng, M. Dai, B. Fang, Y. Huang, S. Zeng, Z. Huang, J. Xue, X. Li, S. Shi, F. Cheng, Assembly of PAN/Gr@ MWCNTs/CoFe2O4 multilayer composite films for high-efficiency electromagnetic shielding and joule heating, Compos. Sci. Technol. (2025) 111081.
[23] J. Cheng, H. Zhang, M. Ning, H. Raza, D. Zhang, G. Zheng, Q. Zheng, R. Che, Emerging materials and designs for low-and multi-band electromagnetic wave absorbers: the search for dielectric and magnetic synergy? Adv. Funct. Mater. 32 (23) (2022) 2200123.
[24] S. Begum, H. Ullah, A. Kausar, M. Siddiq, M.A. Aleem, Fabrication of epoxy functionalized MWCNTs reinforced PVDF nanocomposites with high dielectric permittivity, low dielectric loss and high electrical conductivity, Compos. Sci. Technol. 167 (2018) 497–506.
[25] V.N. Popov, Carbon nanotubes: properties and application, Mater. Sci. Eng.: R: Rep. 43 (3) (2004) 61–102.
[26] P. Pokharel, D. Xiao, F. Erogbogbo, O. Keles, et al., A hierarchical approach for creating electrically conductive network structure in polyurethane nanocomposites using a hybrid of graphene nanoplatelets, carbon black and multi-walled carbon nanotubes, Compos. Part B: Eng. 161 (2019) 169–182.
[27] J. Prabhudass, K. Palanikumar, E. Natarajan, K. Markandan, Enhanced thermal stability, mechanical properties and structural integrity of MWCNT filled bamboo/kenaf hybrid polymer nanocomposites, Materials 15 (2) (2022) 506.
[28] Z.-I. Lin, C.-W. Lou, Y.-J. Pan, C.-T. Hsieh, C.-H. Huang, C.-L. Huang, Y.-S. Chen, J.-H. Lin, Conductive fabrics made of polypropylene/multi-walled carbon nanotube coated polyester yarns: Mechanical properties and electromagnetic interference shielding effectiveness, Compos. Sci. Technol. 141 (2017) 74–82.
[29] K. Lichtenecker, Die herlritung des logarithmischen mischungsgesetzes aus allgemeinen prinzipien der stationaren stromung, Phys. Z 32 (1931) 255–260.
[30] R.C. Rumpf, Improved formulation of scattering matrices for semi-analytical methods that is consistent with convention, Prog. Electromagn. Res. B 35 (2011) 241–261.
[31] A.P. Kumar, R. Nakka, D. Harursampath, S.A. Ponnusami, Computational evaluation of absorption characteristics of ceramic-based auxetic materials in X-band frequency range, Smart Mater. Struct. 32 (10) (2023) 105024.
[32] E. Michielssen, J.-M. Sajer, S. Ranjithan, R. Mittra, Design of lightweight, broadband microwave absorbers using genetic algorithms, IEEE Trans. Microw. Theory Tech. 41 (6) (2002) 1024–1031.
[33] D.M. Pozar, Microwave Engineering, 4th ed., University of Massachusetts at Amherst, John Wiley & Sons, Inc, 2012, pp. 26–30.
[34] Q.-H. Sun, H.-C. Zhai, Y.-F. Liu, C.-S. Li, J.-W. Wang, X. Jian, N. Mahmood, Kirkendall effect-assisted electrospinning porous FeCo/Zn@ C nanofibers featuring well-dispersed FeCo nanoparticles for ultra-wide electromagnetic wave absorption, Rare Met. 44 (3) (2025) 1856–1868.
[35] J.-F. Wang, M. Xia, J.-N. Sun, H.-Y. Zhang, Q.-H. Sun, J.-W. Wang, N. Mahmood, X. Jian, Hybrid bilayers of carbon/NiBr2 anchoring on FeSiB surface for enhanced microwave absorption coupling with smart discoloration, Rare Met. 44 (1) (2025) 489–502.
[36] D. Sheng, Z. Song, S. Cheng, W. Wang, Z. Chen, R. Gao, W. Li, A. Xie, Defect-rich carbon nanosheets derived from p (C3O2) x for electromagnetic wave absorption applications, Carbon 230 (2024) 119637.
[37] S. Cheng, D. Sheng, S. Mukherjee, W. Dong, Y. Huang, R. Cao, A. Xie, R.A. Fischer, W. Li, Carbon nanolayer-mounted single metal sites enable dipole polarization loss under electromagnetic field, Nat. Commun. 15 (1) (2024) 9077.
[38] Z. Chen, J. Zhang, L. Ni, D. Sheng, R. Gao, W. Li, A. Xie, Improving electromagnetic wave absorption property of metal borides/carbon nanocomposites by magnetic-electric balance and ion substitution tuning strategy, Carbon 221 (2024) 118901.
[39] W. Guo, B. Hong, J. Xu, Y. Han, X. Peng, J. Li, H. Chen, X. Wang, Highly-improved microwave absorption performance of LaFeO3/Fe@ CNTs nanocomposites through in-situ synthesis of Fe@ CNTs, Ceram. Int. 51 (1) (2025) 764–776.
[40] Z. Guo, J. Ren, X. Xu, D. Lan, S. Zhang, M. He, Z. Gao, Z. Jia, G. Wu, Multiphase Co/Ni metal nitrides with heterointerfaces for enhanced interfacial polarization loss in electromagnetic wave absorption, J. Mater. Sci. Technol. (2025).
[41] Y. Zhang, Y. Zhang, L. Yan, R. Liu, J. Jiang, C. Liu, F. Wu, F. Xu, Multiphasic Fe/Co oxide@ α-Fe magnetic composites for enhanced microwave absorption and corrosion resistance, J. Magn. Magn. Mater. 606 (2024) 172378.
[42] M. Sathish Kumar, M. Mandhakini, S. Jeferson, R. Jayavel, Silane functionalized cardanol/calcium carbonate epoxy-reinforced polymer nanocomposites for sustainable microwave absorption applications, Polym. Compos. 45 (15) (2024) 13924–13939.
[43] Z. Liu, K. Wang, H. Zhang, S. Huang, N. Xie, Q. Wang, H. Zhu, Y. Liu, X. Zhao, Solvothermally synthesized Co (CoO)/Ti3C2T x/TiO2 nanocomposites for enhanced microwave absorption, ACS Appl. Nano Mater. 7 (5) (2024) 5488–5497.
[44] C. Guo, S. Shao, X. Zhang, Y. Tang, L. Wang, J. Liu, L. Wu, K. Bi, F. Wang, Multifunctional MXene/rGO aerogels loaded with Co/MnO nanocomposites for enhanced electromagnetic wave absorption, thermal insulation and pressure sensing, Nano Res. 17 (9) (2024) 7803–7813.
[45] L. Pang, H. Luo, X. Fan, W. Zhou, P. Chen, P. Xiao, Q. Wen, Y. Li, Z. Yu, R. Riedel, Electromagnetic wave absorbing performance of multiphase (SiC/HfC/C)/SiO2 nanocomposites with an unique microstructure, J. Eur. Ceram. Soc. 41 (4) (2021) 2425–2434.
[46] C. Wang, H. Wang, J. Wu, H. Wei, J. Xue, Enhanced electromagnetic wave absorption performance of multiphase (TiC/TiO2/C)/SiOC composites with unique microstructures, Mater. Charact. 203 (2023) 113131.
[47] R. Rotaru, C. Peptu, P. Samoila, V. Harabagiu, Preparation of ferroelectric barium titanate through an energy effective solid state ultrasound assisted method, J. Am. Ceram. Soc. 100 (10) (2017) 4511–4518.
[48] M. Biglar, M. Gromada, F. Stachowicz, T. Trzepieciński, Synthesis of barium titanate piezoelectric ceramics for multilayer actuators (mlas), Acta Mech. et Autom. 11 (4) (2017) 275–279.
[49] S. Mitra, P.S. Veluri, A. Chakraborthy, R.K. Petla, Electrochemical properties of spinel cobalt ferrite nanoparticles with sodium alginate as interactive binder, ChemElectroChem 1 (6) (2014) 1068–1074.
[50] E. Swatsitang, S. Phokha, S. Hunpratub, B. Usher, A. Bootchanont, S. Maensiri, P. Chindaprasirt, Characterization and magnetic properties of cobalt ferrite nanoparticles, J. Alloys Compd. 664 (2016) 792–797.
[51] G. Faraci, S. Gibilisco, P. Russo, A.R. Pennisi, S. La Rosa, Modified Raman confinement model for Si nanocrystals, Phys. Rev. B— Condens. Matter Mater. Phys. 73 (3) (2006) 033307.
[52] V.H. Ojha, K.M. Kant, Investigation of structural and magnetic properties of strained CoFe2O4 nanoparticles, J. Phys. Chem. Solids 148 (2021) 109655.
[53] F. Nakagomi, S. Da Silva, V. Garg, A. Oliveira, P. Morais, A. Franco Jr., Influence of the Mg-content on the cation distribution in cubic MgxFe3- xO4 nanoparticles, J. Solid State Chem. 182 (9) (2009) 2423–2429.
[54] Z. Wang, D. Schiferl, Y. Zhao, H.S.C. O'Neill, High pressure Raman spectroscopy of spinel-type ferrite ZnFe2O4, J. Phys. Chem. Solids 64 (12) (2003) 2517–2523.
[55] Sarita, Anchal, Priya, S.R. Choudhary, M.S. Rulaniya, A. Kumar, S.N. Dolia, P.A. Alvi, B.L. Choudhary, Studies of structural, optical, and Raman analysis of Ni-substituted CoFe2O4, Phys. Status Solidi (A) (2024) 2400083.
[56] P.B. Kharat, S.B. Somvanshi, J.S. Kounsalye, S.S. Deshmukh, P.P. Khirade, K. Jadhav, Temperature dependent viscosity of cobalt ferrite/ethylene glycol ferrofluids, in: AIP Conference Proceedings, 1942, AIP Publishing, 2018, pp. 0094–243X.
[57] A. Awadallah-f, S. Al-Muhtaseb, Carbon nanoparticles-decorated carbon nanotubes, Sci. Rep. 10 (1) (2020) 4878.
[58] N.T. Abdel-Ghani, G.A. El-Chaghaby, F.S. Helal, Individual and competitive adsorption of phenol and nickel onto multiwalled carbon nanotubes, J. Adv. Res. 6 (3) (2015) 405–415.
[59] H. Soleimani, M.K. Baig, N. Yahya, L. Khodapanah, M. Sabet, B.M. Demiral, M. Burda, Impact of carbon nanotubes based nanofluid on oil recovery efficiency using core flooding, Results Phys. 9 (2018) 39–48.
[60] A.C. Ferrari, J. Robertson, Raman spectroscopy of amorphous, nanostructured, diamond–like carbon, and nanodiamond, Philos. Trans. R. Soc. Lond. Ser. A Math. Phys. Eng. Sci. 362 (1824) (2004) 2477–2512.
[61] M.S. Dresselhaus, G. Dresselhaus, R. Saito, A. Jorio, Raman spectroscopy of carbon nanotubes, Phys. Rep. 409 (2) (2005) 47–99.
[62] A.C. Ferrari, J. Robertson, Interpretation of Raman spectra of disordered and amorphous carbon, Phys. Rev. B 61 (20) (2000) 14095.
[63] L. Cançado, K. Takai, T. Enoki, M. Endo, Y. Kim, H. Mizusaki, A. Jorio, L. Coelho, R. Magalhães-Paniago, M. Pimenta, General equation for the determination of the crystallite size la of nanographite by Raman spectroscopy, Appl. Phys. Lett. 88 (16) (2006).